THE UNIVERSITY OF NOTTINGHAM

SINGLE-WALLED CARBON NANOTUBE MODELLING BASED ON ONE- AND TWO-DIMENSIONAL COSSERAT CONTINUA

A DISSERTATION

SUBMITTED TO THE GRADUATE SCHOOL

IN PARTIAL FULFILLMENT OF THE REQUIREMENTS

for the degree

DOCTOR OF PHILOSOPHY

Civil Engineering

By

Yu Zhang

May 2011

Abstract

This research aims to study the mechanical properties of single-walled carbon nanotubes. In order to overcome the difficulties of spanning multi-scales from atomistic field to macroscopic space, the Cauchy-Born rule is applied to link the deformation of atom lattice vectors at the atomic level with the material deformation in a macro continuum level. Single-walled carbon nanotubes are modelled as Cosserat surfaces, and modified shell theory is adopted where a displacement field-independent rotation tensor is introduced, which describes the rotation of the inner structure of the surface, i.e. micro-rotation. Empirical interatomic potentials are applied so that stress fields and modulus fields can be computed by the derivations of potential forms from displacement fields and rotation fields. A finite element approach is implemented. Results of simulations for single-walled carbon nanotubes under stretching, bending, compression and torsion are presented. In addition, Young's modulus and Poisson ratio for graphite sheet and critical buckling strains for single-walled carbon nanotubes are predicted in this research.

Acknowledgements

Firstly, I express my great gratitude to my supervisor, Professor Carlo Sansour, for his guidance and patient supervision and partly financial support through my study.

Secondly, I would like to thank Dr. Sebastian Skatulla for his help with the development of the program and valuable comments on the thesis.

Thirdly, I am heartily grateful to Professor Hai Sui Yu who supported and encouraged me during the completion of the research, who is also the internal examiner.

Also, it has to be mentioned of a massive thanks to Professor Harm Askes, who is the external examiner, who has given great advices on the corrections on original thesis.

Finally, my most appreciation is to my family, who have always been the greatest motivation for me to work, study and to live my life.

Declaration

The work described in this thesis was conducted at the Centre for Structural Engineering and Construction, School of Civil Engineering, The University of Nottingham, between September 2005 and May 2011. I declare that the work is my own and has not been submitted for a degree of another university.

Contents

Figures

Tables

Nomenclature

$\boldsymbol{A}, \boldsymbol{a}$	undeformed lattice vector and deformed lattice vector
$\boldsymbol{C}_h$	chiral vector
D	direct derivative
D	carbon nanotube diameter
e_{ijk}	permutation tensor (Levi-Civita tensor) (i, j, k = 1, 2, 3)
$\boldsymbol{e}_i$	Cartesian co-ordinates (i = 1, 2, 3)
E	Young's modulus
$\boldsymbol{f}, \boldsymbol{f}_s$	external forces on the surface and on the boundary
F	applied force
$\boldsymbol{F}$	deformation gradient
$\boldsymbol{G}_\alpha, \boldsymbol{g}_\alpha$	covariant base vectors of $\boldsymbol{X}$ and $\boldsymbol{x}$
$G_{\alpha\beta}, g_{\alpha\beta}$	Riemannian metric
h	carbon nanotube effective wall thickness
$\boldsymbol{k}_\alpha$	axial vector of $\boldsymbol{R}^T\boldsymbol{R}_{,\alpha}$
$\boldsymbol{l}$	axial vector of $\boldsymbol{L}$

$\boldsymbol{L}$	right multiplication of rotation tensor
$\boldsymbol{m}$	tensor-like bending modulus
$\boldsymbol{n}$	tensor-like stretch modulus
$\boldsymbol{N}$	normal vector
$\boldsymbol{q}, \boldsymbol{q}_s$	external torques on the surface and on the boundary
$\boldsymbol{R}$	rotation tensor
S_0	area of representative atomic cell
$\boldsymbol{S}$	force tensor
$\boldsymbol{T}$	couple tensor
$\boldsymbol{u}$	displacement vector
$\boldsymbol{U}$	first Cosserat deformation tensor
V	interatomic potential
W_0	strain energy density
$\boldsymbol{X}, \boldsymbol{x}$	a point on reference configuration and its position after deformation
$\mathcal{B}, \mathcal{B}_t$	reference and deformed surface
ε	strain
$\boldsymbol{\varepsilon}$	Ricci tensor
ϑ^{α}	co-ordinates in $\mathcal{B}$, $(\alpha = 1,2)$
$\boldsymbol{\mathcal{K}}$	second Cosserat deformation tensor
$\boldsymbol{\omega}$	eigenvector of $\boldsymbol{R}$
$\boldsymbol{\eta}$	inner displacement vector

Chapter 1

Introduction

1.1 Background

It was a revolution in nano-science when carbon nanotubes (CNTs) were discovered by Iijima in 1991 with their outstanding properties. Because of their unique electrical properties and extremely high thermal conductivity, CNTs have been used for electronics, field-emission displays, energy storage, functional fillers in composites, and some biomedical devices (*Ajayan and Zhou 2001; Baughman et al. 2002; Endo et al. 2006*). Moreover, CNTs have high elastic modulus (>1TPa), large elastic strain - up to 5%, and large breaking strain - up to 20% (*Iijima 1991*). Their excellent mechanical properties could lead to many more applications. For example, with their amazing strength and stiffness, plus the advantage of lightness, perspective future applications of CNTs are in aerospace engineering and virtual bio-devices.

CNTs have been studied worldwide by scientists and engineers since their discovery, but a robust, theoretically precise and efficient prediction of the mechanical properties of CNTs has not yet been found. The problem is, when the size of an object is small to nano-scale, their many physical properties cannot be modelled and analyzed by using constitutive laws from traditional continuum theories, since the complex atomistic processes affect the results of their macroscopic behaviour. In this case, atomistic simulations can give more precise modelled results of the underlying physical properties. However, fully atomistic simulations of a whole carbon nanotube are computationally infeasible at present.

Thus, a new atomistic and continuum mixing modelling method is needed to solve the problem, which requires crossing the length and time scales. The research here is to develop a proper technique of spanning multi-scales from atomic to macroscopic space, in which the constitutive laws are derived from empirical atomistic potentials which deal with individual interactions between single atoms at the micro-level, whereas Cosserat continuum theories are adopted for a shell model through the application of the Cauchy-Born rule to give the properties which represent the averaged behaviour of large volumes of atoms at the macro-level.

Since experiments of CNTs are relatively expensive at present, and often unexpected manual errors could be involved, it will be very helpful to have a mature theoretical method for the study of mechanical properties of CNTs. Thus, if this research is successful, it could also be a reference for the research of all sorts of research at the nano-scale, and the results can be of interest to aerospace, biomedical engineering and other displines.

1.2 **Structure of carbon nanotubes**

Carbon nanotubes (CNTs) are tubular carbon molecules with particular properties. Generally, they can be divided in two main categories: single-walled carbon nanotubes (SWCNTs) and multi-walled carbon nanotubes (MWCNTs). SWCNTs can be considered as rectangular strips of hexagonal graphite monolayers rolling up to cylinder tubes. Two types of SWCNTs with high symmetry are normally selected by researchers, which are zigzag SWCNTs and armchair SWCNTs. When some of the atomic bonds are parallel to the tube axis, the CNT is called a zigzag CNT, while if the bonds are perpendicular to the axis, it is called an armchair CNT, and for any other structures, they are called chiral CNTs, as shown in Figure 1.1 (*Dresselhaus et al. 1996*).

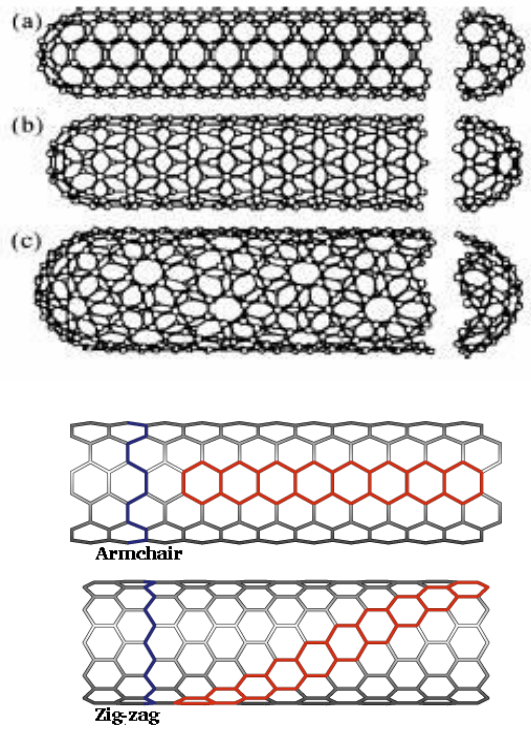

Figure 1-1: Some SWCNTs with different chiralities. (a) armchair structure (b) zigzag structure (c) chiral structure (*Dresselhaus et al. 1996*)

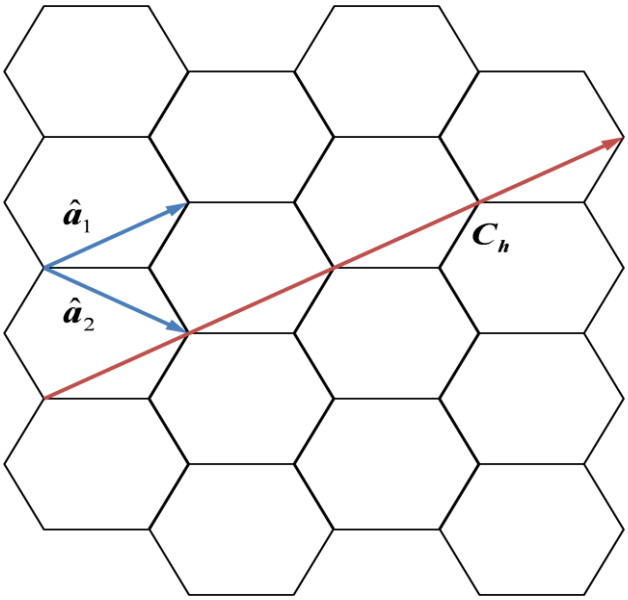

Figure 1-2: Basis vectors and chiral vector

Chiral vector $\boldsymbol{C}_h$ is a vector that maps an atom of one end of the tube to the other. $\boldsymbol{C}_h$ can be an integer multiple of $\hat{\boldsymbol{a}}_1$ and $\hat{\boldsymbol{a}}_2$, which are two basis vectors of the graphite cell. Then we have $\boldsymbol{C}_h = n\hat{\boldsymbol{a}}_1 + m\hat{\boldsymbol{a}}_2$, with integer n and m, and the constructed CNT is called a (n, m) CNT, as shown in Figure 1.2. It can be proved that for armchair CNTs $n = m$, and for zigzag CNTs $m = 0$. For example, in Figure 1.2, the structure is designed to be a (4,0) zigzag SWCNT.

MWCNT can be considered as the structure of a bundle of concentric SWCNTs with different diameters. The length and diameter of MWCNTs are different from those of SWCNTs, which means, of course, their properties differ significantly. This research concentrates on solving the mechanical properties of SWCNTs. In further research, MWCNTs can be modelled as a collection of SWCNTs, provided the interlayer interactions are modelled by Van der Waals forces in the simulation.

A SWCNT can be modelled as a hollow cylinder by rolling a graphite sheet as shown in Figure 1.3. If a planar graphite sheet is considered to be an undeformed configuration, and the SWCNT is defined as the current configuration, then the relationship between the SWCNT and the graphite sheet can be shown to be:

$$e_1 = G_1, \qquad e_2 = R\sin\frac{G_2}{R}, \qquad e_3 = R\cos\frac{G_2}{R} - R$$

where G_1, G_2 are the material co-ordinates of a point in the initial configuration and e_1, e_2 and e_3 are the co-ordinates in the current configuration. R is the radius of the modelled SWCNT. The relationship between the integers n, m and the radius of SWCNT R is given by $R = a\sqrt{m^2 + mn + n^2}/2\pi$, where $a = \sqrt{3}a_0$, and a_0 is the length of a non-stretched C-C bond which is $0.142nm$ given by *Wu et al.* (*2006*).

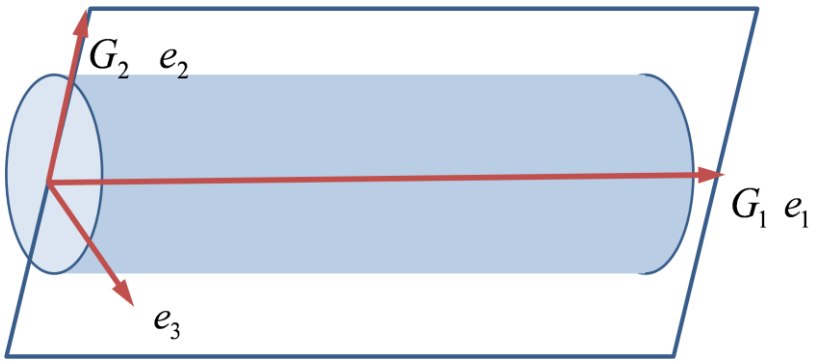

Figure 1-3: Illustration of a graphite sheet rolling to SWCNT

As a graphite sheet can be 'rolled' into a SWCNT, we can 'unroll' the SWCNT to a plane graphite sheet. Since a SWCNT can be considered as a rectangular strip of hexagonal graphite monolayer rolling up to a cylindrical tube, the general idea is that it can be modelled as a cylindrical shell, a cylinder surface, or it can pull-back

to be modelled as a plane sheet deforming into curved surface in three-dimensional space. A MWCNT can be modelled as a combination of a series of concentric SWCNTs with inter-layer interatomic reactions.

Provided the continuum shell theory captures the deformation at the macro-level, the inner micro-structure can be described by finding the appropriate form of the potential function which is related to the position of the atoms at the atomistic level. Therefore, the SWCNT can be considered as a generalized continuum with microstructure.

1.3 **Literature Review**

1.3.1 Aim: study on mechanical properties of carbon nanotubes

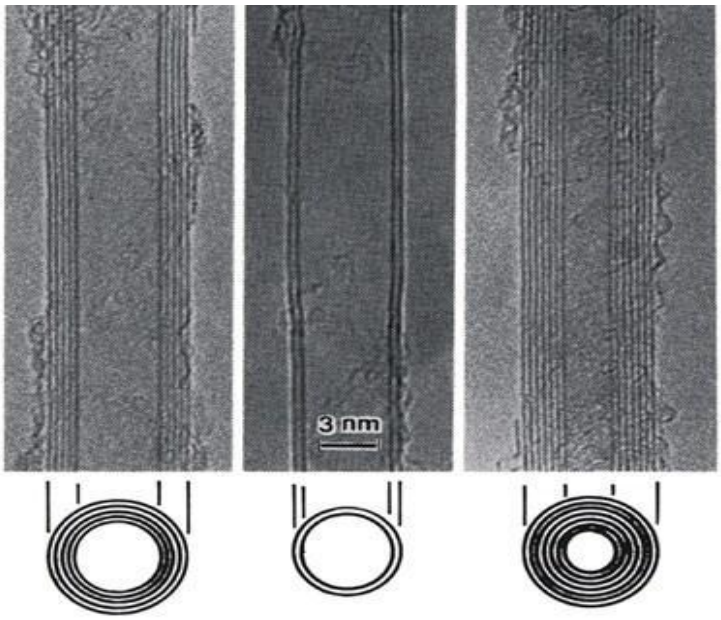

Figure 1-4: Electron micrographs of the cross section of different types of carbon nanotube (*Iijima, 1991*)

Since the discovery of CNTs, their mechanical properties have been the subject of many studies. Generally, CNTs can be divided into two types: single-walled (SWCNTs) and multi-walled carbon nanotubes (MWCNTs). A transmission electron micrograph of different types of carbon nanotube is shown in Figure 1.4.

1.3.1.1 Young's modulus

Young's modulus and Poisson ratio are two independent elastic constants which are important measures of stiffness in classical elasticity theory. However, the established definitions of elastic measures in solid mechanics may fail in CNTs, since the spacing and the inner structure are very complex at the nano-scale. *Iijima* (*1991*) obtained Young's modulus of CNTs around 1TPa. *Treacy et al.* (*1996*) observed a much higher Young's modulus of CNTs to an axial load. A large scatter in the value of Young's modulus for CNTs exists, whether in experimental results or in theoretical calculations, which varies from 0.5TPa to 6TPa. In addition, researchers also presented different points of view on how the scale of tube diameter affects Young's modulus of CNTs.

Different authors presented different points of view about the dependence of CNT's Young's modulus on the tube diameter. *Chang and Gao* (*2003*) derived the expressions for the elastic modulus and Poisson ratio of a SWCNT as a function of the CNT diameter. They compared their results with those from other researchers in Figure 1.5. *Li and Chou* (*2003*) predicted that Young's modulus and the shear modulus increase with the increasing of tube diameter, with an average Young's modulus around 1TPa (Figure 1.6). *Wang et al.* (*2006*) presented similar results for Young's modulus in length and circumferential directions and pointed out two different sets of parameters for potential models which result in

significantly different outcomes, as shown in Figure 1.7. *Avila and Lacerda* (*2008*) demonstrated the same trend for Young's modulus and Poisson ratio against the tube diameter (Figure 1.8).

On the other hand, *Gao and Li* (*2003*) concluded that Young's modulus is not directly proportional to the tube diameter, and they also demonstrated that Young's modulus depends on the wall thickness of CNTs, which is shown in Figure 1.9. *Lei et al.* (*2011*) obtained the inversely proportional results for Young's modulus against tube diameter, as shown in Figure 1.10. *Parvaneh and Shariati* (*2011*) as well gained the inverse results, and they proved that the calculation of Young's modulus was also affected by aspect ratio and loading types (Figure 1.11).

Meo and Rossi (*2006*) modelled and calculated Young's modulus of CNTs of an average of 0.915TPa, which is independent of the tube diameter. They pointed out, that this diameter-independence was also obtained by *Wen et al.* (*2004*) and only a very slight dependence was obtained by *Jin and Yuan* (*2003*). This shows that some of the statements to be found in the literature are contradictory.

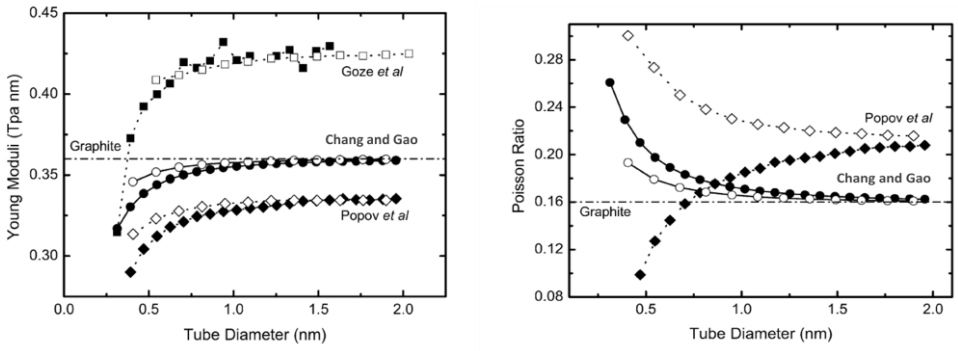

Figure 1-5: Young's modulus and Poisson ratio with dependence on tube diameter. Open symbols for armchair tubes and solid symbols for zigzag tubes. (*Chang and Gao, 2003*)

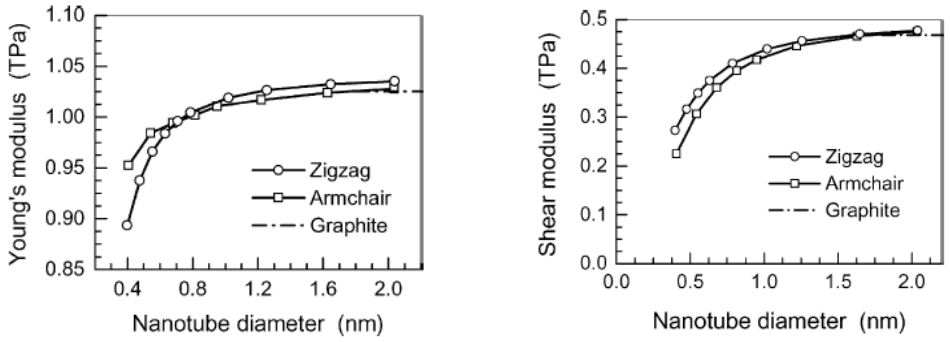

Figure 1-6: Young's modulus and shear modulus with dependence on tube diameter. (*Li and Chou, 2003*)

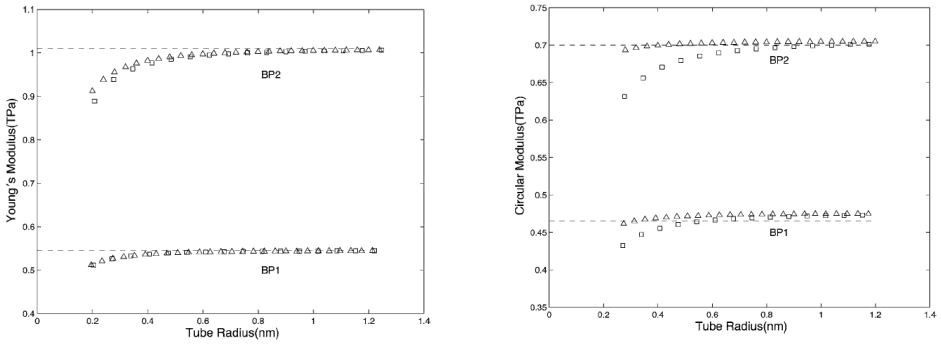

Figure 1-7: Young's modulus and circular modulus with dependence on tube diameter. BP1 and BP2 are two potential models. (*Wang et al. 2006*)

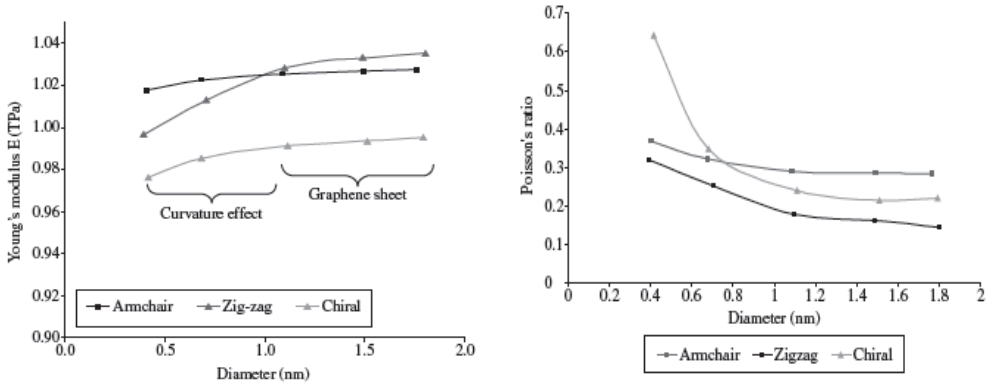

Figure 1-8: Young's modulus and Poisson ratio with dependence on tube diameter. (*Avila and Lacerda, 2008*)

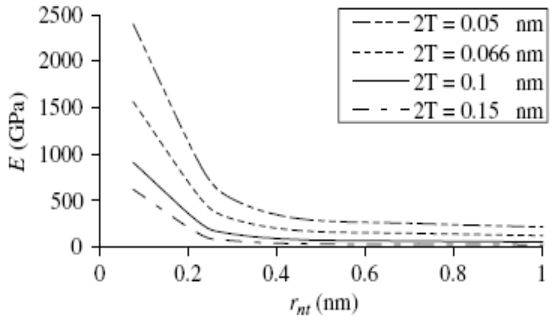

Figure 1-9: Young's modulus and Poisson ratio with dependence on tube diameter and wall thickness. T is the wall thickness. (*Gao and Li, 2003*)

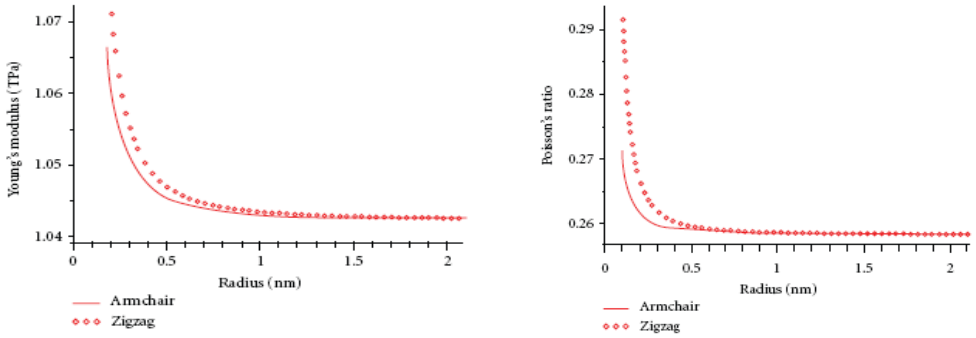

Figure 1-10: Young's modulus and Poisson ratio with dependence on tube diameter. (*Lei et al. 2011*)

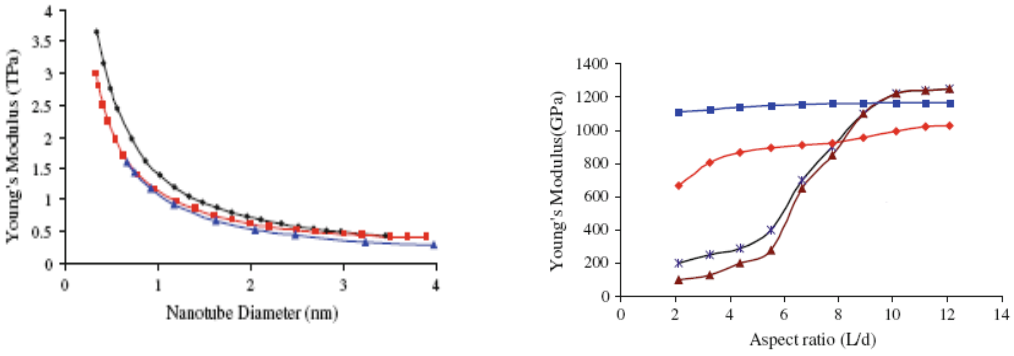

Figure 1-11: Young's modulus with dependence on tube diameter and aspect ratio. (*Parvaneh and Shariati, 2011*)

1.3.1.2 Bending, buckling and torsion

All the above cited authors in Section 1.3.1.1 have shown that CNTs exhibit very high stiffness in their axial direction, however, CNTs as a whole, especially SWCNTs, are very flexible in bending mode since their length is much larger than their diameter. *Huhtala et al.* (*2002*) simulated two sets of SWCNTs under bending strain, and gave out the result deformations as shown in Figure 1.12.

At larger strains, CNTs tend to have non-linear behaviour, but the changes are reversible with no atomic rearranging or bond breaking, this behaviour is called resilience (*Hertel et al. 1998*).

Figure 1.13 shows the simulation of buckling of a SWCNT under axial compression (*Yakobson et al. 1996*). With the strain increasing, the tube buckled into pattern b and then into pattern c. It buckled sideways at point d and squashed asymmetrically at point e. They also presented simulations of torsion deformations of SWCNTs as shown in Figure 1.14. *Arroyo and Belystchko* (*2004*) simulated deformations of SWCNTs under compression and under torsion as well (Figure 1.15).

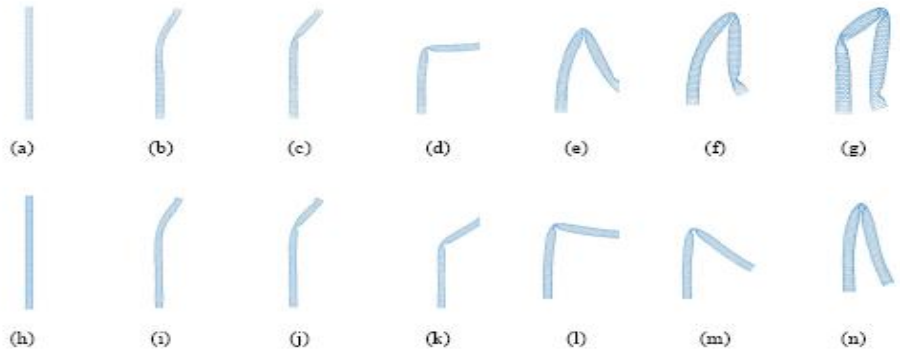

Figure 1-12: Two sets of simulations of nanotube behaviour under increasing bending strain (*Huhtala et al. 2002*)

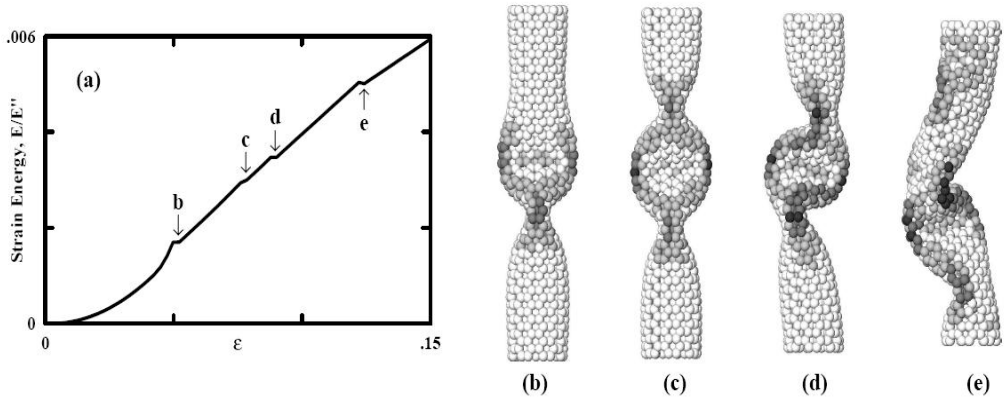

Figure 1-13: Simulation of SWCNT under axial compression (*Yakobson et al. 1996*)

Figure 1-14: Simulation of SWCNT under torsion (*Yakobson et al. 1996*)

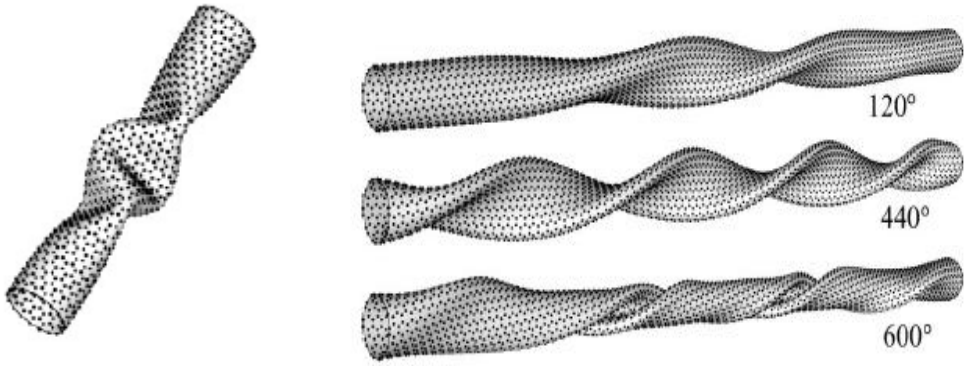

Figure 1-15: Simulation of compressed and twisted SWCNTs (*Arroyo and Belytschko, 2004*)

1.3.2 Inspirations on methodologies

1.3.2.1 Nanomechanics

Traditional continuum mechanics have been used to model CNTs in early years. *Govindjee and Sackman* (*1999*) used a simple Bernoulli–Euler beam model and continuum elastic theory to calculate the Young's Modulus of CNTs. *Pantano et al.* (*2004*) built CNT models with shell theory using continuum methods as well. *Natsuki and Endo* (*2004*) also simulated mechanical properties of CNTs based on a continuum shell model. Afterwards continuum cylindrical shell models were widely applied in the buckling analysis of CNTs (*He et al. 2005, Zhang et al. 2006, Yang and Wang 2007*). But, as shown by *Govindjee and Sackman* (*1999*), the mechanical properties of CNTs are distinctly dependent on the size of the system, thus in nano-scale situations, the constitutive laws of traditional continuum mechanics are no longer applicable. *Wang et al.* (*2006*) also proved the dependence on scale effect in studying CNTs. They observed that solutions obtained from classical elastic beam and shell model were significantly overestimated, so the scale effect had to be taken into account to provide reasonable results.

The more accurate modelling of CNTs is via atomistic methods, which considers each atom as its fundamental unit and describes their behaviour by a series of equations. One of the most popular atomistic models of CNTs is the empirical potential molecular mechanics model, which considers a series of atoms as repeating units and predicts the potential energies as a function of the positions of atoms. *Bao et al.* (*2004*) studied Young's moduli of CNTs based on molecular

dynamics (MD) simulation. *Chang and Gao* (*2003*) also presented the elastic properties of SWCNTs through a molecular mechanics approach, and recommended further applications of molecular mechanics in CNTs modelling. *Liew et al.* (*2004*) also used MD simulations to describe the mechanical properties of CNTs. In addition to the elastic properties, such as Young's modulus and Poisson's ratio, they studied the plastic behaviour and the fracture of CNTs. *Sun and Zhao* (*2005*) used a finite element model based on molecular mechanics to calculate the strength of SWCNTs. *Meo and Rossi* (*2006*) applied molecular mechanics based finite element approach to simulate the fracture progress in CNTs.

Atomistic simulation is necessary for the fracture study of CNTs, because continuum mechanics cannot capture all the details of an atomic bond breakage or dislocation at a micro-level (*Belytschko et al. 2002, Lu and Bhattacharya 2005, Meo and Rossi 2006*). Since this research is concentrating on the study of the elastic properties of CNTs, there is no need for a full atomistic simulation of a whole CNT which would be extremely computationally expensive and time consuming rendering it impractical. Therefore, a new atomistic and continuum mixing method needs to be established, which is computationally practical and can provide more accurate physical results than a classical continuum theory.

To apply continuum mechanics to the study of CNTs, the first step is to think about how to link the continuum behaviour of CNTs with the atomic deformations at the nano-level. In this aspect, the inspiration came from *Arroyo and Belytschko* (*2003, 2004*) with the idea of applying modified Cauchy-Born rule on the study of mechanical properties of CNTs.

1.3.2.2 The Cauchy-Born rule

The Cauchy-Born rule is a rule to link the atomistic field to the continuum world that describes the relations between the deformation of atom lattice vectors and the deformation of bulk vectors. As pointed out by *Arroyo and Belytschko* (*2003, 2004*), the Cauchy–Born rule is not directly suitable to applications of CNT, because CNT can be viewed as a curved surface, and the deformation gradient maps the deformed vector on the tangent space of the deformed curve instead of the real chord vector which lies on the curve. In order to achieve more accurate results through Cauchy-Born rule, different kinds of modifications have been created. *Arroyo and Belytschko* (*2003, 2004*) developed a so-called exponential Cauchy-Born rule which was demonstrated naturally mapping the tangent vector into the chord on the curved surface. *Guo et al.* (*2006*) presented a higher order Cauchy-Born rule by preserving more higher-order terms in Taylor's expansion to improve the accuracy of approximation. Since modification of the Cauchy-Born rule is an important inspiration of this research, the exponential and higher order Cauchy-Born rules are briefly explained.

1.3.2.2.1 Exponential Cauchy-Born rule

Arroyo and Belytschko (*2003, 2004*) described two-dimensional manifold deforming in three-dimensional Euclidean space. The undeformed surface $\Omega_0 \subset \mathbb{R}^2$ represents the planar grapheme as the reference configuration. It is changed by the deformation map into the deformed surface $\Omega \subset \mathbb{R}^3$. The deformation gradient $\boldsymbol{F}$ is the tangent of the configuration map $T\Phi$, which maps infinitesimal vectors of the undeformed plane Ω_0 into vectors on the tangent plane of the deformed surface Ω (Figure 1.16). The standard Cauchy-Born rule $\boldsymbol{a} = \boldsymbol{FA}$

produces vectors after deformation map on the tangent plane of the deformed surface instead of the real chord on the curve of the surface. In order to capture the effect of curvature in the deformed surface, *Arroyo and Belytschko* (*2003, 2004*) composed the standard Cauchy-Born rule with an exponential map, and represented the so-called exponential Cauchy-Born rule, which naturally maps the tangent space onto the curved surface. This is accomplished by

$$\boldsymbol{a} = \exp \circ \boldsymbol{FA} \tag{1.1}$$

where 'exp' defines the exponential map. The exponential map brings the original deformed vector after the standard Cauchy-Born rule, which lies on the tangent plane of the curved surface, $\boldsymbol{w} = \boldsymbol{FA}$, i.e. the tangent deformed lattice vector to the chord of the curved surface (Figure 1.16).

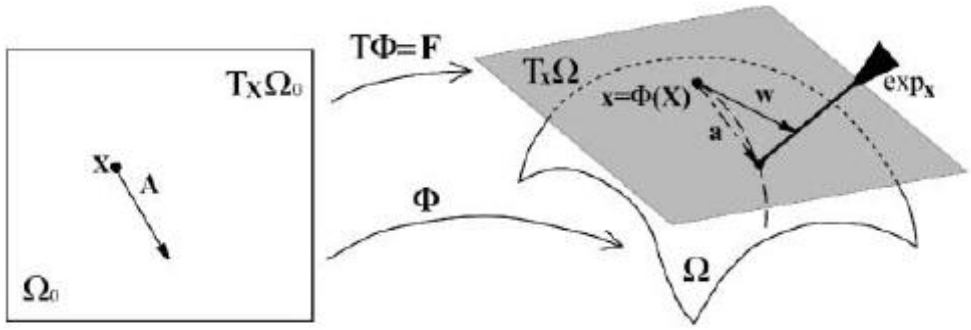

Figure 1-16: Illustration of the exponential Cauchy-Born rule (*Arroyo and Belytschko, 2003*)

Consider the principal directions of the curved surface are $\boldsymbol{v}_1$ and $\boldsymbol{v}_2$, and the normal vector at point $\boldsymbol{x}$ is $\boldsymbol{v}_1 \times \boldsymbol{v}_2$. Then the components of $\boldsymbol{w}$ can be calculated as

$$\begin{Bmatrix} w_1 \\ w_2 \end{Bmatrix} = \begin{Bmatrix} \boldsymbol{w} \cdot \boldsymbol{v}_1 \\ \boldsymbol{w} \cdot \boldsymbol{v}_2 \end{Bmatrix} = \begin{Bmatrix} \boldsymbol{V}_1 \cdot \boldsymbol{C} \cdot \boldsymbol{A} \\ \boldsymbol{V}_2 \cdot \boldsymbol{C} \cdot \boldsymbol{A} \end{Bmatrix} = \begin{Bmatrix} C_{AB} A^A (V_1)^B \\ C_{AB} A^A (V_2)^B \end{Bmatrix} \tag{1.2}$$

where $\boldsymbol{C}$ is the Green deformation tensor defined by $\boldsymbol{C} = \boldsymbol{F}^T\boldsymbol{F}$, and $\boldsymbol{V}$ is the pull back of $\boldsymbol{v}$ on the undeformed body, $\boldsymbol{v} = \boldsymbol{F}\boldsymbol{V}$. By defining $\vartheta(x) = \sin(x)/x$, the local approximation to the exponential Cauchy-Born rule is

$$\boldsymbol{a} = \begin{Bmatrix} a^1 \\ a^2 \\ a^3 \end{Bmatrix} = \begin{Bmatrix} w_1\vartheta(k_1 w_1) \\ w_2\vartheta(k_2 w_2) \\ \frac{k_1 w_1^2}{2}\vartheta^2\left(\frac{k_1 w_1}{2}\right) + \frac{k_2 w_2}{2}\vartheta^2\left(\frac{k_2 w_2}{2}\right) \end{Bmatrix} \tag{1.3}$$

where $k_{1,2}$ are the principal curvatures corresponding to $\boldsymbol{v}_{1,2}$, which can be obtained from the eigenvalue problem

$$\boldsymbol{\mathcal{K}}\boldsymbol{V} = \boldsymbol{k}\boldsymbol{C}\boldsymbol{V} \tag{1.4}$$

where $\boldsymbol{\mathcal{K}}$ is the curvature tensor. Then the deformed chord vector $\boldsymbol{a}$ can be a function of the undeformed lattice vector $\boldsymbol{A}$, the Green deformation tensor $\boldsymbol{C}$ and the curvature tensor $\boldsymbol{\mathcal{K}}$. The bond length a, and the angle θ between two deformed bonds $\boldsymbol{a}$ and $\boldsymbol{b}$ can be calculated from

$$a = \|\boldsymbol{a}\| = \sqrt{a^c a^c} \tag{1.5}$$

$$\theta = \arccos\frac{\boldsymbol{a}\cdot\boldsymbol{b}}{a\ b} = \arccos\frac{a^c b^c}{a\ b} \tag{1.6}$$

Therefore, the lengths of bonds and angles between bonds have been written in terms of two strain measures $\boldsymbol{C}$ and $\boldsymbol{\mathcal{K}}$, i.e. $a = f(\boldsymbol{C}, \boldsymbol{\mathcal{K}}; \boldsymbol{A})$ and $\theta = g(\boldsymbol{C}, \boldsymbol{\mathcal{K}}; \boldsymbol{A}, \boldsymbol{B})$, which are further used to formulate continuum constitutive functions on the base of inter-atomic potentials which consist of functions of bond lengths and angles. The strain energy density (energy per unit undeformed area) can be written as

$$W_0(\boldsymbol{C}, \boldsymbol{\mathcal{K}}) = \frac{1}{S_0}\sum V\left(a_1, a_2, a_3, \theta_1, \theta_2, \theta_3\right) \tag{1.7}$$

S_0 defines the area of a unit cell, $a_{1,2,3}$ are the bond lengths of the three bonds connected on one atom, $\theta_{1,2,3}$ are the bond angles between the three bonds.

Two stress measures, a force stress tensor, where $\boldsymbol{S}_{II}$ is the second Piola-Kirchhoff stress tensor, and a moment like stress tensor $\boldsymbol{T}$, can be derived from

$$\boldsymbol{S}_{II} = 2\frac{\partial \widehat{W}_0}{\partial \boldsymbol{C}}, \qquad \boldsymbol{T} = \frac{\partial \widehat{W}_0}{\partial \boldsymbol{\mathcal{K}}} \tag{1.8}$$

Lagrangian elasticity tensors can be obtained by second derivatives

$$\boldsymbol{n} = 4\frac{\partial^2 \widehat{W}_0}{\partial \boldsymbol{C}^2}, \qquad \boldsymbol{m} = \frac{\partial^2 \widehat{W}_0}{\partial \boldsymbol{\mathcal{K}}^2}, \qquad \boldsymbol{n}_c = 2\frac{\partial^2 \widehat{W}_0}{\partial \boldsymbol{C}\,\partial \boldsymbol{\mathcal{K}}} \tag{1.9}$$

These three tensors represent in-plane stiffness, bending stiffness and coupling stiffness respectively (*Arroyo and Belytschko, 2002,2003,2004*). It is written $\widehat{W}_0$ instead of W_0 due to the consideration of inner displacement functioning in the potential form, which will be further explained in Section 2.3.2.

1.3.2.2.2 Higher order Cauchy-Born rule

Guo et al. (*2006*) presented an extension of the standard Cauchy-Born rule by introducing a higher order deformation gradient. In classical continuum mechanics deformation gradient is defined by

$$d\boldsymbol{x} = \boldsymbol{F}d\boldsymbol{X} \tag{1.10}$$

Instead of the standard Cauchy-Born rule $\boldsymbol{a} = \boldsymbol{FA}$, *Leamy et al.* (*2003*) defined the deformed lattice vector $\boldsymbol{b}$ as

$$\boldsymbol{b} = \int_{\boldsymbol{0}}^{\boldsymbol{a}} \boldsymbol{F}(\boldsymbol{s})\boldsymbol{ds} \tag{1.11}$$

$\boldsymbol{F}(\boldsymbol{s})$ is assumed to be a Taylor's expansion of the deformation field

$$\boldsymbol{F}(\boldsymbol{s}) = \boldsymbol{F}(\boldsymbol{0}) + \nabla\boldsymbol{F}(\boldsymbol{0}) \cdot \boldsymbol{s} + \frac{\nabla\nabla\boldsymbol{F}(\boldsymbol{0}) : (\boldsymbol{s} \otimes \boldsymbol{s})}{2} + \mathrm{O}(\|\boldsymbol{s}\|^3) \tag{1.12}$$

By retaining two terms of the expansion, approximated deformed lattice vector can be expressed as

$$\boldsymbol{b} \approx \boldsymbol{F}(\boldsymbol{0})\boldsymbol{a} + \frac{1}{2}\nabla \boldsymbol{F}(\boldsymbol{0}) : (\boldsymbol{a} \otimes \boldsymbol{a}) \tag{1.13}$$

As shown in Figure 1.17, the higher order term brings the tangent vector from the standard Cauchy–Born rule closer to the real deformed configuration. The accuracy of approximation can be improved by introducing more higher-order terms, although the computation work will be more time consuming.

The strain energy density W_0 can be expressed as

$$W_0 = W_0(|\boldsymbol{a}_{I1}|, |\boldsymbol{a}_{I2}|, |\boldsymbol{a}_{I3}|) = \frac{1}{S_0}\sum_{J=1}^{3} V_{IJ}\,(\boldsymbol{a}_{I1}, \boldsymbol{a}_{I2}, \boldsymbol{a}_{I3}) \tag{1.14}$$

which represents the potential for an atom I, and S_0 is the area of a representative cell at the undeformed configuration.

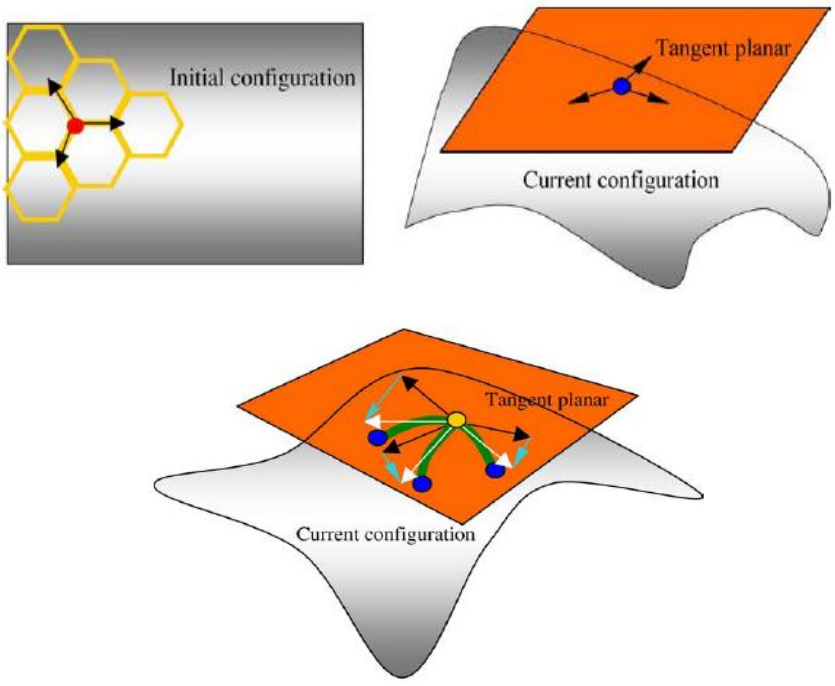

Figure 1-17: Illustration of the higher order Cauchy-Born rule (*Guo et al. 2006*)

$$\boldsymbol{a}_{IJ} = \boldsymbol{F}\boldsymbol{A}_{IJ} + \boldsymbol{P} : \frac{\boldsymbol{A}_{IJ} \otimes \boldsymbol{A}_{IJ}}{2} \tag{1.15}$$

where $\boldsymbol{a}_{IJ}$ and $\boldsymbol{A}_{IJ}$ denote the deformed and undeformed lattice vectors. The following relations hold

$$\boldsymbol{F} = F_{ij}\boldsymbol{e}_i \otimes \boldsymbol{e}_j\,, \qquad \boldsymbol{P} = \nabla \boldsymbol{F} = G_{ijk}\boldsymbol{e}_i \otimes \boldsymbol{e}_j \otimes \boldsymbol{e}_k \tag{1.16}$$

with which the strain energy density can be written as

$$W_0 = W_0(\boldsymbol{F}, \boldsymbol{P}) \tag{1.17}$$

The first Piola-Kirchhoff stress tensor $\boldsymbol{S}_I$ and the higher-order stress tensor $\boldsymbol{T}_I$ are

$$\boldsymbol{S}_I = \frac{\partial W_0}{\partial \boldsymbol{F}} = \frac{1}{S_0}\sum_{J=1}^{3} \boldsymbol{f}_{IJ} \otimes \boldsymbol{A}_{IJ} \tag{1.18}$$

$$\boldsymbol{T}_I = \frac{\partial W_0}{\partial \boldsymbol{P}} = \frac{1}{2S_0}\sum_{J=1}^{3} \boldsymbol{f}_{IJ} \otimes \boldsymbol{A}_{IJ} \otimes \boldsymbol{A}_{IJ} \tag{1.19}$$

where $\boldsymbol{f}_{IJ}$ is the generalized force defined as

$$\boldsymbol{f}_{IJ} = \frac{\partial W_0}{\partial \boldsymbol{a}_{IJ}} \tag{1.20}$$

Let $W_0 = \widetilde{W}_I / S_0$, where

$$\widetilde{W}_I = \sum_{J=1}^{3} V_{IJ}\left(\boldsymbol{a}_{IJ}, \boldsymbol{a}_{IK}, \theta_{IJK}, K \neq I, J\right) \tag{1.21}$$

V_{IJ} is taken as the form of interatomic potential for carbon.

The generalized stiffness $\boldsymbol{K}_{IJLK}$is defined as

$$\boldsymbol{K}_{IJLK} = \frac{\partial \boldsymbol{f}_{IJ}}{\partial \boldsymbol{a}_{LK}} = \frac{\partial^2 W_0}{\partial \boldsymbol{a}_{IJ} \partial \boldsymbol{a}_{LK}} \tag{1.22}$$

The modulus tensors $\boldsymbol{n}$ can be derived as

$$\boldsymbol{n}_{FF} = \frac{\partial^2 \widehat{W}_0}{\partial \boldsymbol{F} \otimes \partial \boldsymbol{F}}\,, \qquad \boldsymbol{n}_{FP} = \frac{\partial^2 \widehat{W}_0}{\partial \boldsymbol{F} \otimes \partial \boldsymbol{P}}$$

$$\boldsymbol{n}_{PF} = \frac{\partial^2 \widehat{W}_0}{\partial \boldsymbol{P} \otimes \partial \boldsymbol{F}}, \qquad \boldsymbol{n}_{GG} = \frac{\partial^2 \widehat{W}_0}{\partial \boldsymbol{P} \otimes \partial \boldsymbol{P}} \tag{1.23}$$

Again it is written $\widehat{W}_0$ instead of W_0 because of the inclusion of inner displacement in potential functions.

Both the above methods are based on the same idea by adding extra higher order terms into the deformation gradient in order to approximate the real curve after standard Cauchy-Born rule, which is different in this research where the standard Cauchy-Born rule stays to describe the strain at the tangent plane, and modification is made by adding a displacement field-independent rotation tensor at each point of the surface, which describes the curvature by rotating the deformed vector on the tangent plane into the real deformed curve itself. Thus, the Cosserat continuum theory is introduced via the independent rotation tensor in order to describe the curvature of the deformed surface after applying the standard Cauchy-Born rule to the tangent vectors. Cosserat surface as a shell model is established in this research since SWCNT can be modelled as a hollow cylindrical shell, therefore built as a two-dimensional surface instead of a three-dimensional solid continuum.

1.3.2.3 Cosserat surface as a shell model

SWCNTs, as well MWCNTs have been modelled as linear elastic shells (*Tu and Ou-yang, 2002, Pantano et al. 2004*) or non-linear elastic shells (*Arroyo and Belytschko, 2002,2003,2004*) via continuum mechanics methods. In the linear elastic range, Young's modulus and the wall thickness were found by fitting the interatomic model, covering a large range from 0.5TPa to 6TPa, and from 0.06nm to 0.6 nm.

Wu et al. (*2008*) developed a finite-deformation shell theory for CNTs based on the interatomic potentials for carbon. Shell theory based on interatomic potentials is the approach by all the authors above and as well as in this research. *Wu et al.* (*2008*) set a relationship for the rates of the second Piola-Kirchhoff stress tensor $\boldsymbol{S}$ and the bending moment tensor $\boldsymbol{T}$ to the increments of Green strain tensor $\boldsymbol{E}$ and curvature tensor $\boldsymbol{\mathcal{K}}$ as

$$\dot{\boldsymbol{S}} = \boldsymbol{n} : \dot{\boldsymbol{E}} + \boldsymbol{n}_c : \dot{\boldsymbol{\mathcal{K}}} \tag{1.24}$$

$$\dot{\boldsymbol{T}} = \boldsymbol{n}_c^T : \dot{\boldsymbol{E}} + \boldsymbol{m} : \dot{\boldsymbol{\mathcal{K}}} \tag{1.25}$$

where $\boldsymbol{n}$, $\boldsymbol{m}$ and $\boldsymbol{n}_c$, $\boldsymbol{n}_c^T$ are the tension, bending and coupling rigidity derived from interatomic potentials

$$\boldsymbol{n} = \frac{\mathrm{D}}{\mathrm{D}\boldsymbol{E}}\left(\frac{\partial W}{\partial \boldsymbol{E}}\right), \boldsymbol{m} = \frac{\mathrm{D}}{\mathrm{D}\boldsymbol{\mathcal{K}}}\left(\frac{\partial W}{\partial \boldsymbol{\mathcal{K}}}\right), \boldsymbol{n}_c = \frac{\mathrm{D}}{\mathrm{D}\boldsymbol{\mathcal{K}}}\left(\frac{\partial W}{\partial \boldsymbol{E}}\right), \boldsymbol{n}_c^T = \frac{\mathrm{D}}{\mathrm{D}\boldsymbol{E}}\left(\frac{\partial W}{\partial \boldsymbol{\mathcal{K}}}\right) \tag{1.26}$$

and it modified the constitutive model in classical continuum shell theory by adding extra coupling terms to describe the stress-curvature and moment-strain relations.

Sansour and Bednarczyk (*1995*) presented a shell theory for the Cosserat surface which is considered as a two-dimensional manifold in Cosserat continuum, and the surface is attached with a determined displacement field and an independent rotation field. In classical continuum mechanics elasticity theory there are two elastic constants involved which can be directly derived from the displacement field, but Cosserat continuum theory introduces one more material constant that is related to a three parametric rotation tensor attached to every particle of the continuum, which takes into consideration size effects in the calculations. The theory has been developed in further years to model viscoplastic shells (*Kollman*

and Sansour, 1999), and hyperelastic behaviours (*Haefner et al. 2002*), and also to study finite strain elastoplasticity (*Sansour et al. 2006),* and finite strain plasticity (*Sansour 2006*).

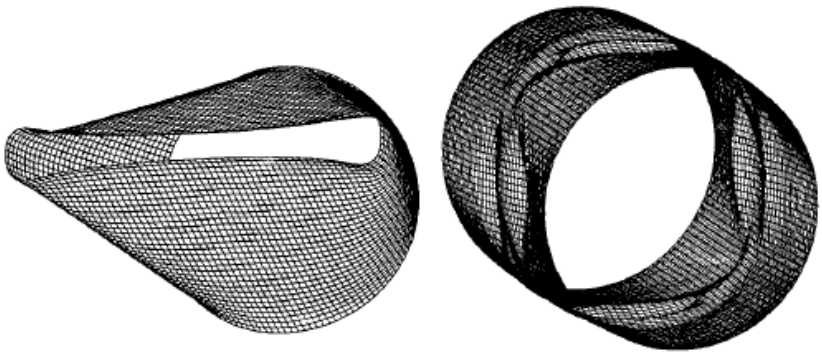

Figure 1-18: Deformation of pinched cylinder (*Sansour and Kollmann, 1998*)

These studies identified significant advantages over classical shell theory and original Cosserat continuum methods. The introduced rotation tensor is an independent variable which provides an insight into the interior structure of the surface. Drilling degrees are included in a completely natural way. This approach can produce good results for shells under large deformation, as shown in Figure 1.18.

SWCNT can be considered as a two-dimensional manifold and can be solved with the Cosserat surface shell theory demonstrated by *Sansour and Bednarczyk* (*1995*), where the rotation field is already at a micro-level. However, the Cosserat surface shell theory (*Sansour and Bednarczyk, 1995*) is based on constitutive laws from conventional continuum theory, for the study of CNTs, which will be

deviated in this research by constitutive laws derived from empirical interatomic potentials which describe the real interactions among atoms at an atomic level.

1.4 **Outline**

This research is to propose a new multi-scale modelling method to simulate the mechanical properties of SWCNTs. The central idea of the method is to consider SWCNT as a Cosserat surface based on continuum shell theory. Constitutive laws are derived from empirical interatomic potential functions which describe the local potential of CNTs at the atomic level. The Cauchy-Born rule is applied to connect the atomic description to a macroscopic space, which provides the strain changing on the deformed surface. A shift vector is needed for the hexagonal arrangement of atoms in SWCNT. An independent rotation tensor is employed to compute the change of curvature of the deformed surface which is introduced in Cosserat surface shell theory to overcome the application of the standard Cauchy-Born rule on the study of CNTs. The Cosserat surface shell model is then analyzed to produce results and simulations through a finite element approach.

Chapter 1 has given the background of CNTs and the previous studies of CNTs. The literature review mainly includes research results of the linear and non-linear elastic properties of CNTs from previous researchers, and discusses the methodologies for studying SWCNTs. From inadequate continuum mechanics to computationally difficult atomistic simulations, we are looking for a decent approach to link them and give more accurate results of CNTs in a practical way.

Chapter 2 presents the whole methodologies. Section 2.1 shows the main structure of the modelling methods. Section 2.2 explains the Cauchy-Born rule and why it

should be modified when studying CNTs. This section also introduces a shift vector which should be taken into account when the Cauchy-Born rule is applied to a non-centrosymmetric structure. Section 2.3 presents a shell theory for Cosserat surface, in which the deformation gradient, the rotation tensor and the strain measures are defined, and where the equilibrium equations are derived from the principle of virtual work. Section 2.4 provides the potential forms designed for the one-dimensional rod and two-dimensional surface to be applied in the next two chapters. Section 2.5 provides the implementation of finite element approach based on shell theory of the Cosserat surface. The finite element formulation is developed, and an updating method of the rotation tensor is designed so as to be path independent.

Chapter 3 designs an atomic chain model, and simulates the deformations from one-dimensional to two-dimensional and to three-dimensional space. Numerical modelling equations are given. Results are presented and compared. Simulations of a one-dimensional embedded rod, a thread in torsion and a cross section of CNTs in bending are demonstrated. It shows that atomic chains and CNTs have many behaviours in common. Although the quantitative physical meaning of atomic chain is still under development, it gives a fundamental preparation of full graphite sheet and CNT simulations.

Chapter 4 further demonstrates the Cosserat surface as a shell model which is applied to a two-dimensional graphite sheet deforming in-plane and out-of-plane. Young's modulus and Poisson ratio are predicted for the graphite sheet and the results are compared with the literature. SWCNTs are modelled as cylindrical shells, and deformations of SWCNTs under bending, compression and torsion are

simulated. Young's modulus is predicted from cylindrical shell bending models. Buckling strains are predicted from force-strain relationship figures for cylindrical shell model under compression. A twisting angle against external torque force relationship is shown for the cylindrical shell model under torsion.

Chapter 5 summarises and concludes the work carried out in this research. Discussions about the modelling methods and the results are presented. Possible improvements are suggested towards the end of the chapter.

Chapter 2

Modelling Methods

2.1 **Main Idea**

The aim of this research is to study the mechanical properties of SWCNTs. Two kinds of methodologies have been established by other researchers, one being continuum mechanics-based, and the other by atomistic simulations.

Traditional continuum mechanics have been used to model CNTs in earlier years. Two main approaches are based on the Bernoulli–Euler beam model and the continuum cylindrical shell model. However, as for the study of the mechanical properties of CNTs many of the assumptions in classical continuum mechanics are no longer applicable because of the size effect of nano-structures. *Wang et al.* (*2006*) pointed out that the classical elastic beam and shell models provided highly overestimated results when modelling CNTs, thus, the scale effect cannot

be ignored, although atomistic simulations give accurate results when modelling CNTs, the very fact that one has to calculate every atom in the system makes them incredibly time consuming and computationally inefficient. Therefore, a bridge linking continuum mechanics and atomistic simulations is developed.

The Cauchy-Born rule is a rule to relate the deformation of an atom bond vector at a micro-level to the deformation of the bulk vector at a macro-level. It is applicable for solid crystals, but it is not suitable to apply to CNTs, because the map Cauchy-Born builds leads to a deformed vector lying on the tangent plane of the curved surface instead of lying on the curve. However motivated by the exponential Cauchy-Born rule (*Arroyo and Belytschko 2002*) and the higher order Cauchy-Born rule (*Guo et al. 2006*), a modification of the standard Cauchy-Born to applications for modelling CNTs as shells is established.

In this research an alternative way is investigated. A shell theory based on Cosserat continua is presented to model CNTs following the work of *Sansour and Bednarczyk* (*1995*). A displacement field-independent rotation tensor is introduced to describe the micro-level rotation, which also makes up for the shortcomings of the standard Cauchy-Born rule, and can take size-effects into account. The main idea of this research is to consider SWCNT as a two-dimensional manifold and solving it with the Cosserat surface shell theory as demonstrated. The deformation can be described by a stretch tensor and a rotation tensor. Responding to external force, the surface deforms providing a force stress field and a couple stress field. A force stress tensor can be obtained from the first derivative of the potential with respect to a stretch tensor, and a couple stress tensor can be obtained from the first derivative of the potential with respect to a

curvature tensor. Stretch modulus tensors can be found from the second derivative of the potential with respect to the stretch tensor, and bending modulus tensor can be calculated from the second derivative of potential with respect to the curvature tensor. In order to solve for these four fields mentioned above, a way to describe the material mechanical properties, one needs to identify the right potential forms that are adequate at an atomistic level and applicable for continuum formulations.

Two sets of models are considered in this research. As a hypothetical example, also being the preparation of the whole CNT modelling, an atomic chain model, referred to as a Cosserat curve, is developed as a one-dimensional rod deforming in a three-dimensional space. Further modelling is carried out by considering SWCNT as a Cosserat surface deforming in a three-dimensional space. For the atomic chain model, the energy functions are chosen from molecular mechanics, which is also called the force field method. The total energy is determined by the interactions of the atoms, which takes into account contributions from atom bond stretching, bending between atom bonds and torsion energy. This model can be considered as an atomic chain that consists of a series of carbon atoms, and C-C bonds, which deforms in an atomic field.

For two-dimensional Cosserat surface of the SWCNT model, empirical functions of potentials are adopted which are practical and appropriate to describe the total potential of CNTs relatively accurately. The simplest potential functions, for example the Morse potential, have no dependence on the environment of the atoms, therefore not suitable to apply to a Cosserat surface. Thus we have to go for relatively complicated potentials which incorporate the effects of atom bond angles and bond orders, among which the Tersoff and Brenner potential (*Tersoff,*

1988, Brenner, 1989) involves the variations of bond energy due to changes in the position of an atom and also its neighbour atoms. A first generation of Tersoff and Brenner potentials was extensively applied in the study CNTs (*Belytschko et al. 2002, Zhang et al. 2002, Bao et al. 2004, Liew et al. 2004*). *Brenner et al.* (*2002*) made a few adjustments and developed a second generation of Brenner potentials, which they claimed to be more accurate to model the real interactomic reactions.

The finite element formulation is developed on the basis of variational principles. The stress fields and the modulus fields can thus be calculated via iteration procedures by updating displacement fields and rotation fields, where the rotation fields are designed to be path-independent in updating.

Section 2.2 demonstrates the Cauchy-Born rule, and also explains how the Cauchy-Born rule links continuum systems with the atomistic world, and why it should be modified to study surfaces when modelling CNTs. Also, an inner shift vector is introduced due to the restrictions of the Cauchy-Born rule when applied to the hexagonal structure of carbon cells. Section 2.3 presents the shell theory of the Cosserat surface, where a displacement field-independent rotation tensor is introduced, which is applied in this research instead of the modified Cauchy-Born rule, by rotating the tangent vector which is on the tangent plane of deformed surface into the real curve which lies on the deformed surface. Section 2.4 aims to find the appropriate forms of the potential functions to describe the potential of the atomic chain and the potential of a graphite sheet which is also used as a potential for CNTs. Section 2.5 furnishes the implementation of finite element approach of the Cosserat surface.

2.2 Cauchy-Born rule

2.2.1 Standard Cauchy-Born rule

The Cauchy–Born rule is an assumption made to link the deformation of the atomistic field to that of continuum field. It is normally used for bulk materials, e.g. space-filling crystals. In such homogeneous materials, without consideration of any defects, the Cauchy-Born rule is applied to show the relationship between the deformation of atomic lattice vectors and the deformation of the whole bulk material in the continuum field.

Similar to local crystal kinematics, where the deformation of the crystal vectors are described by the Cauchy-Born rule, the deformation of the bulk atom lattice, and respectively the bond vectors connecting two neighbouring atoms, can be described by the local deformation gradient. So, in essence, the deformation gradient is assumed to be constant within a small portion of the atom lattice and the latter can be dealt with as a bundle of lines where relative angles do not change, i.e. the tangent bundles. We find here the similarity to nonlocal theories.

Consider $\boldsymbol{\Phi}$ as the deformation map when a space-filling continuum body $\Omega_0 \subset \mathbb{R}^3$deforms to $\Omega \subset \mathbb{R}^3$, i.e. $\Omega = \boldsymbol{\Phi}(\Omega_0)$. Let $\boldsymbol{X}$ define a point in body Ω_0, while $\boldsymbol{x}$ is its position in body Ω after deformation, then we have the relationship $\boldsymbol{x} = \boldsymbol{\Phi}(\boldsymbol{X})$. The deformation gradient $\boldsymbol{F}$ is defined as the derivative of the deformation map, $\boldsymbol{F} = \mathrm{D}\boldsymbol{\Phi}$, which also means that it maps infinitesimal line elements from the deformed configuration to reference configuration

$$d\boldsymbol{x} = \boldsymbol{F}d\boldsymbol{X} \tag{2.1}$$

In elasticity theory, under finite strains, the deformation of space-filling continuum is homogeneous at the atomistic scale. Thus, the space-filling continuum undergoes the same deformation as the atomic lattice vectors as established by the Cauchy-Born rule:

$$\boldsymbol{a} = \boldsymbol{F}\boldsymbol{A} \tag{2.2}$$

where $\boldsymbol{a}$ is the deformed lattice vector, and $\boldsymbol{A}$ is the undeformed lattice vector in the continuum. Equation (2.2) is the essence of the Cauchy-Born rule which shows the link between atomistic and continuum deformations, as shown in Figure 2.1.

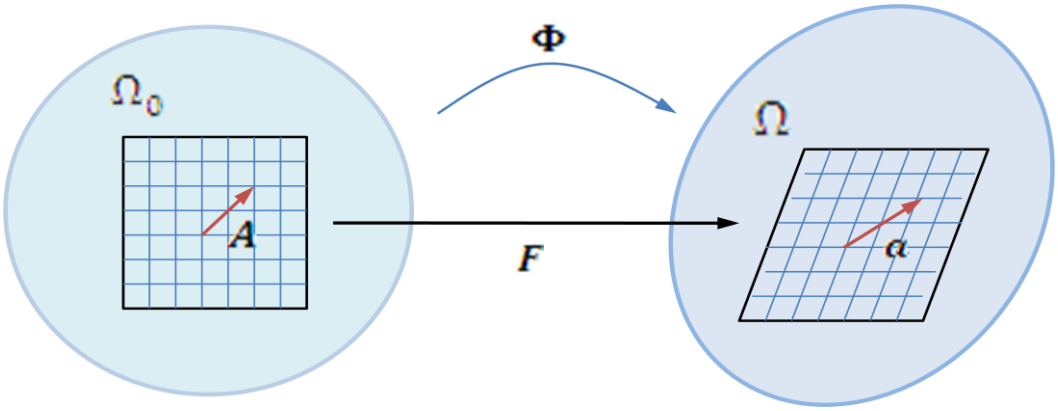

Figure 2-1: Illustration of Cauchy-Born rule

However, in case of CNTs, we have to deal with a curved surface consisting of chords, which are the bonds connecting the atoms laying in them. Although the Cauchy-Born rule is valid for the bulk atom lattice, it does not apply to the chords of CNTs. This is due to the fact that deformation vertical to the CNT's axis is accompanied by a change of curvature of the surface. This also means the angles between the atom bonds must have changed as well. In this case, the deformation at the surface of the CNT that is pure stretch of the chords, and can be described

by the deformation gradient, but the out-of-plane deformation which is related to the change of angles between connected chords, must be separately described, e.g. by the change of curvature of the surface.

Arroyo and Belytschko (*2003,2004*) first pointed out, though Cauchy–Born rule is suitable to apply for space-filling crystal material, it is not adequate to apply to CNTs, which can be viewed as a curved surface with nano-scale thickness, especially when it involves in large curvature effects. Because the deformation gradient tensor $\boldsymbol{F}$ maps the infinitesimal material vectors $d\boldsymbol{X}$ and $d\boldsymbol{x}$, if SWCNT is considered as a plane surface without thickness, the deformed lattice vector $\boldsymbol{a}$ will be falling on the tangent plane of the curved surface , which means the standard Cauchy-Born rule gives inaccurate result of deformed lattice vector $\boldsymbol{a}$, as a tangent vector which is tangent to the curve, instead of the accurate result of the real chord vector which is lying on the curve. Different kinds of modifications have been made to overcome the shortcomings mentioned above for the use of the standard Cauchy-Born rule in the study of properties of CNTs, such as the exponential Cauchy-Born rule, the higher order Cauchy-Born rule, the local Cauchy-Born rule, etc., some of which have been explained in Section 1.3.2.2.

2.2.2 Shift vector

Due to the non-centrosymmetric hexagonal atomic structure of CNTs, the standard Cauchy-Born rule cannot be applied directly for CNTs because it cannot satisfy the inner equilibrium of the representative cell. A system is said to be centrosymmetric when at any time for one point at position (x, y, z) there is always another point at position$(-x, -y, -z)$. For a centrosymmetric lattice there has to be another lattice pointing the opposite direction from the same atom,

which is not the case for CNTs. The Cauchy-Born rule ensures the equilibrium of centrosymmetric lattices because the forces of paired lattices are equal and opposite under homogeneous deformation.

The hexagonal lattice of a graphite sheet, which is called a Bravais multi-lattice, is not centrosymmetric, however, it consists of two centrosymmetric sub-lattices. Therefore, it is essential to introduce an in-plane shift vector as a bridge of two centrosymmetric sub-lattices. The position vectors of multi-lattice, two centrosymmetric sub-lattices, and an inner displacement of the atom sites are described in Figure 2.2.

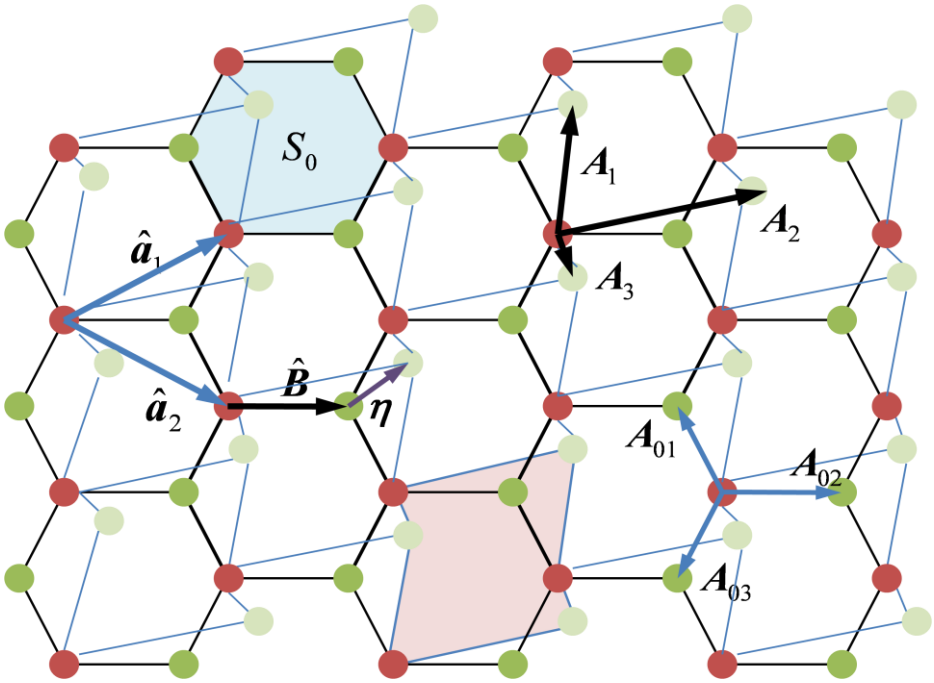

Figure 2-2: Multi-lattice, sub-lattices, and shift vector

Let $\hat{\boldsymbol{a}}_i$ $(i = 1,2)$ define the basis vectors of a centrosymmetric sub-lattice, and $\hat{\boldsymbol{B}}$ be the relative shift vector of two sub-lattices. To reach the required degrees of freedom, an additional kinematic variable is introduced, by describing the

perturbation of the shift vector, denoted by $\boldsymbol{\eta}$. The bond vectors $\boldsymbol{A}_i$ (i=1, 2, 3) after the perturbation are

$$\boldsymbol{A}_i = \boldsymbol{A}_{0i} + \boldsymbol{\eta} \tag{2.3}$$

where $\boldsymbol{A}_{0i}$ are the undeformed bond vectors.

Let $\widehat{\boldsymbol{P}} = \widehat{\boldsymbol{B}} + \boldsymbol{\eta}$, then the bond vectors are

$$\boldsymbol{A}_1 = -\widehat{\boldsymbol{a}}_2 + \widehat{\boldsymbol{P}}, \qquad \boldsymbol{A}_2 = \widehat{\boldsymbol{P}}, \qquad \boldsymbol{A}_3 = -\widehat{\boldsymbol{a}}_1 + \widehat{\boldsymbol{P}} \tag{2.4}$$

The introducing of shift vector results in differences of solutions in the stress and modulus fields for materials with centrosymmetric or non-centrosymmetric atomic structures, which are presented in the following.

2.2.2.1 Centrosymmetric atomic structure

Let $\boldsymbol{F}$ define the deformation gradient, from Cauchy-Born rule, we have

$$\boldsymbol{a} = \boldsymbol{F}\boldsymbol{A}$$

Define $\boldsymbol{A}_{IJ}$ to be the undeformed bond vector between atom I and J. The bond length after deformation is

$$a_{IJ} = \sqrt{\boldsymbol{A}_{IJ}\boldsymbol{F}^T\boldsymbol{F}\boldsymbol{A}_{IJ}} \tag{2.5}$$

The interatomic potential can be described as

$$V = V\left(a_{IJ}, a_{IK}, \theta_{IJK}, K \neq I, J\right) \tag{2.6}$$

where bond length a_{IK} and bond angle between $I - J$ and $I - K$, denoted by θ_{IJK}, are

$$a_{IK} = \sqrt{\boldsymbol{A}_{IK}\boldsymbol{F}^T\boldsymbol{F}\boldsymbol{A}_{IK}} \tag{2.7}$$

$$\cos(\theta_{IJK}) = \frac{a_{IJ}^2 + a_{IK}^2 - a_{JK}^2}{2a_{IJ}a_{IK}} \tag{2.8}$$

and bond length a_{JK} is

$$a_{JK} = \sqrt{\boldsymbol{A}_{JK}\boldsymbol{F}^T\boldsymbol{F}\boldsymbol{A}_{JK}} \tag{2.9}$$

Strain energy density is expressed as

$$W_0 = \frac{\sum_{I,J} V\left(a_{IJ}, a_{IK}, \theta_{IJK}, K \neq I,J\right)}{S_0} \tag{2.10}$$

where S_0 is the area of the representative atomic cell, and the force tensor can be expressed as

$$\overline{\boldsymbol{S}} = \frac{\partial W_0}{\partial \boldsymbol{F}} = \frac{1}{S_0}\sum_{I,J}\left(\frac{\partial V}{\partial a_{IJ}}\frac{\partial a_{IJ}}{\partial \boldsymbol{F}} + \sum_{K(\neq I,J)}\frac{\partial V}{\partial a_{IK}}\frac{\partial a_{IK}}{\partial \boldsymbol{F}}\right.$$

$$\left. + \sum_{K(\neq I,J)}\frac{\partial V}{\partial \theta_{IJK}}\frac{\partial \theta_{IJK}}{\partial \boldsymbol{F}}\right) \tag{2.11}$$

2.2.2.2 Non-centrosymmetric atomic structure

Let $\boldsymbol{\eta}$ define the inner displacement of a sub-lattice $\boldsymbol{A}$, with the undeformed lattice vector $\boldsymbol{A}_0$. Since $\boldsymbol{A} = \boldsymbol{A}_0 + \boldsymbol{\eta}$, the deformed lattice $\boldsymbol{a}$ under inner perturbation and deformation gradient can be written as

$$\boldsymbol{a} = \boldsymbol{F}(\boldsymbol{A}_0 + \boldsymbol{\eta}) \tag{2.12}$$

Then the bond length between atoms I and J becomes

$$a_{IJ} = \sqrt{(\boldsymbol{A}_{0IJ} + \boldsymbol{\eta})\boldsymbol{F}^T\boldsymbol{F}(\boldsymbol{A}_{0IJ} + \boldsymbol{\eta})} \tag{2.13}$$

Same as before the strain energy density is

$$W_0 = \frac{\sum_{I,J} V(a_{IJ}, a_{IK}, \theta_{IJK}, K \neq I,J)}{S_0} \tag{2.14}$$

The bond angle can be obtained from

$$\cos(\theta_{IJK}) = \frac{a_{IJ}^2 + a_{IK}^2 - a_{JK}^2}{2a_{IJ}a_{IK}} \tag{2.15}$$

As an inner variable, $\boldsymbol{\eta}$ can be computed by minimising the strain energy density with respect to $\boldsymbol{\eta}$

$$\frac{\partial W_0}{\partial \boldsymbol{\eta}} = \mathbf{0} \tag{2.16}$$

which leads to

$$\boldsymbol{\eta} = \boldsymbol{\eta}(\boldsymbol{F}) \tag{2.17}$$

Then we have

$$W_0 = W_0\big(\boldsymbol{F}; \boldsymbol{\eta}(\boldsymbol{F})\big) \tag{2.18}$$

The force tensor is now the direct derivative

$$\overline{\boldsymbol{S}} = \frac{\mathrm{D}W_0}{\mathrm{D}\boldsymbol{F}} = \frac{\partial W_0}{\partial \boldsymbol{F}} + \frac{\partial W_0}{\partial \boldsymbol{\eta}}\frac{\partial \boldsymbol{\eta}}{\partial \boldsymbol{F}} = \frac{\partial W_0}{\partial \boldsymbol{F}} \tag{2.19}$$

The modulus tensor $\overline{\boldsymbol{n}}$

$$\begin{aligned}\overline{\boldsymbol{n}} = \frac{\mathrm{D}\overline{\boldsymbol{S}}}{\mathrm{D}\boldsymbol{F}} &= \frac{\mathrm{D}}{\mathrm{D}\boldsymbol{F}}\left(\frac{\partial W_0}{\partial \boldsymbol{F}}\right) + \frac{\mathrm{D}}{\mathrm{D}\boldsymbol{F}}\left(\frac{\partial W_0}{\partial \boldsymbol{\eta}}\right)\frac{\partial \boldsymbol{\eta}}{\partial \boldsymbol{E}} + \frac{\partial W_0}{\partial \boldsymbol{\eta}}\frac{\mathrm{D}}{\mathrm{D}\boldsymbol{E}}\left(\frac{\partial \boldsymbol{\eta}}{\partial \boldsymbol{E}}\right) = \frac{\mathrm{D}}{\mathrm{D}\boldsymbol{F}}\left(\frac{\partial W_0}{\partial \boldsymbol{F}}\right) \\ &= \frac{\partial^2 W_0}{\partial \boldsymbol{F}\partial \boldsymbol{F}} + \frac{\partial^2 W_0}{\partial \boldsymbol{F}\partial \boldsymbol{\eta}}\frac{\partial \boldsymbol{\eta}}{\partial \boldsymbol{F}} \\ &= \frac{\partial^2 W_0}{\partial \boldsymbol{F}\partial \boldsymbol{F}} - \frac{\partial^2 W_0}{\partial \boldsymbol{F}\partial \boldsymbol{\eta}}\left(\frac{\partial^2 W_0}{\partial \boldsymbol{\eta}\partial \boldsymbol{\eta}}\right)^{-1}\frac{\partial^2 W_0}{\partial \boldsymbol{\eta}\partial \boldsymbol{F}}\end{aligned} \tag{2.20}$$

This is also a footprint of the derivations for dealing with inner displacement vector in Section 4.1. *Wang et al.* (*2006*) pointed out the results obtained without inner displacement were closer to atomistic simulation and experimental results than those with inner displacement. But *Arroyo and Belytschko* (*2004*) insisted that, even so, non-relaxation results were theoretically incorrect.

2.3 **The Cosserat surface as a shell model**

The central idea of Cosserat surface is to consider a thin three-dimensional classical continuum shell as a two-dimensional Cosserat continuum manifold, i.e. a Cosserat surface. A displacement field and a rotation field are introduced specifically, where they are independent of each other. Cosserat continuum theory is different from classical continuum theory by introducing a displacement field-independent rotation tensor, which can describe the behaviour of the inner structure within the surface, i.e. at a micro-level. Cosserat surface theory is to apply Cosserat continuum theory into a shell model, where the first and second strain measures are designed to be strain measures of the shell, which leads all different formulations from original Cosserat continuum theory (*Sansour and Bednarczyk, 1995*).

2.3.1 The deformation gradient

Let $\mathcal{B} \subset \mathbb{R}^3$ define a two-dimensional surface, and $\mathbb{R}$ be the real numbers. The map

$$\boldsymbol{\varphi}(t)\colon \mathcal{B} \to \mathbb{R}^3 \tag{2.21}$$

depends on the parameter $t \in \mathbb{R}$. (Here $\boldsymbol{\varphi}$ is a surface to surface map, as a counterpart of body to body map $\boldsymbol{\Phi}$, as mentioned in Section 2.2.1.) The reference configuration is defined by $\boldsymbol{\varphi}_0 = \boldsymbol{\varphi}(t = t_0)$. For simplicity, we write $\mathcal{B}$ instead of $\boldsymbol{\varphi}_0\mathcal{B}$ and $\mathcal{B}_t$ instead of $\boldsymbol{\varphi}(t)\mathcal{B}$, then we have

$$\boldsymbol{\varphi}(t)\colon \mathcal{B} \to \mathcal{B}_t \tag{2.22}$$

At time t, $\boldsymbol{X}$ is a point in the reference configuration and $\boldsymbol{x}$ is the point in the deformed configuration, then the relations hold

$$\boldsymbol{x}(t) = \boldsymbol{\varphi}(\boldsymbol{X}, t) \text{ and } \boldsymbol{X}(t) = \boldsymbol{\varphi}^{-1}(\boldsymbol{x}, t) \tag{2.23}$$

ϑ^{α} $(\alpha = 1,2)$ are the co-ordinates attached to the surface at $\mathcal{B}$, (Figure 2.3). Let $\mathcal{TB}, \mathcal{TB}_t$ be the tangent spaces of $\mathcal{B}$ and $\mathcal{B}_t$ respectively, we can calculate the covariant base vectors as

$$\boldsymbol{G}_{\alpha} = \frac{\partial \boldsymbol{X}}{\partial \vartheta^{\alpha}} \tag{2.24}$$

with $\boldsymbol{G}_{\alpha} \in \mathcal{TB}$, and

$$\boldsymbol{g}_{\alpha} = \frac{\partial \boldsymbol{x}}{\partial \vartheta^{\alpha}} \tag{2.25}$$

with $\boldsymbol{g}_{\alpha} \in \mathcal{TB}_t$.

The Riemannian metric can be obtained by

$$G_{\alpha\beta} = \boldsymbol{G}_{\alpha} \cdot \boldsymbol{G}_{\beta} \text{ and } g_{\alpha\beta} = \boldsymbol{g}_{\alpha} \cdot \boldsymbol{g}_{\beta} \tag{2.26}$$

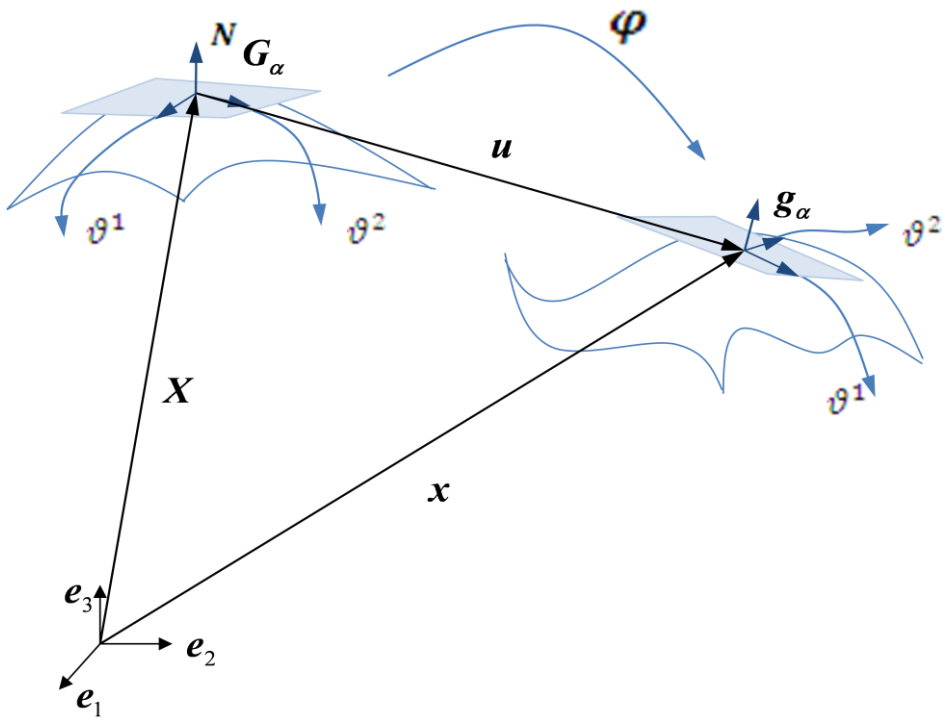

Figure 2-3: Deformation on Cosserat surface

The determinants of $G_{\alpha\beta}$ and $g_{\alpha\beta}$ are indicated by G and g. The basic skew-symmetric three-dimensional Levi-Civita tensor, also known as the permutation tensor, is denoted by

$$e_{ijk} = \begin{cases} +1 & \text{for odd permutations of } i,j,k \\ -1 & \text{for even permutations of } i,j,k \\ 0 & \text{otherwise} \end{cases} \tag{2.27}$$

and

$$\varepsilon_{ijk} \coloneqq \sqrt{G} e_{ijk}$$

$$\varepsilon^{ijk} \coloneqq \frac{1}{\sqrt{G}} e^{ijk} \tag{2.28}$$

where $e_{ijk} = e^{ijk}$ by its Euclidean structure. Here, i,j,k are set to be 1, 2 or 3. In absolute notation, it reads

$$\boldsymbol{\varepsilon} \equiv \varepsilon^{ijk} \boldsymbol{G}_i \otimes \boldsymbol{G}_j \otimes \boldsymbol{G}_k \tag{2.29}$$

Similarly, the two-dimensional Ricci tensors are

$$\varepsilon_{\alpha\beta} = \begin{cases} +\sqrt{G} & \text{for odd permutations of } \alpha,\beta \\ -\sqrt{G} & \text{for even permutations of } \alpha,\beta \end{cases}$$

$$\varepsilon^{\alpha\beta} = \begin{cases} +\dfrac{1}{\sqrt{G}} & \text{for odd permutations of } \alpha,\beta \\ -\dfrac{1}{\sqrt{G}} & \text{for even permutations of } \alpha,\beta \end{cases} \tag{2.30}$$

The normal vector is defined by $\boldsymbol{N} = \varepsilon^{\alpha\beta} \boldsymbol{G}_\alpha \times \boldsymbol{G}_\beta$ at the reference configuration, where it is easily seen that $\boldsymbol{N} \equiv \boldsymbol{G}_3$. For a curvature tensor $\boldsymbol{K} = K_{\alpha\beta} \boldsymbol{G}^\alpha \otimes \boldsymbol{G}^\beta$, its components are given by $K_{\alpha\beta} = -\boldsymbol{N}_{,\alpha} \cdot \boldsymbol{G}_\beta$. Also a Cartesian frame is considered by $\boldsymbol{e}_i$, $i = 1,2,3$ and the quantities can be obtained from

$$c_{\alpha i} = \boldsymbol{G}_\alpha \cdot \boldsymbol{e}_i \,, \qquad c_{3i} = \boldsymbol{N} \cdot \boldsymbol{e}_i \tag{2.31}$$

which describes the relations of the two base systems.

The deformation gradient $\boldsymbol{F}$ is defined as the tangent of the map $\boldsymbol{\varphi}$, $\boldsymbol{F} \equiv \mathcal{T}\boldsymbol{\varphi}$, where

$$\mathcal{T}\boldsymbol{\varphi}\colon \mathcal{TB} \rightarrow \mathcal{TB}_t \text{ , or } \boldsymbol{F}\colon \boldsymbol{G}_\alpha \rightarrow \boldsymbol{g}_\alpha \tag{2.32}$$

$\boldsymbol{F}$ can be given as the tensor product

$$\boldsymbol{F} = \boldsymbol{g}_\alpha \otimes \boldsymbol{G}^\alpha \tag{2.33}$$

The displacement field is introduced by the displacement vector

$$\boldsymbol{u} = \boldsymbol{x} - \boldsymbol{X} \tag{2.34}$$

and we have

$$\boldsymbol{g}_\alpha = \boldsymbol{G}_\alpha + \boldsymbol{u}_{,\alpha} \tag{2.35}$$

and

$$\boldsymbol{F} = (\boldsymbol{G}_\alpha + \boldsymbol{u}_{,\alpha}) \otimes \boldsymbol{G}^\alpha \tag{2.36}$$

where comma denotes partial derivatives.

2.3.2 The rotation tensor

One of the assumptions of the shell theory is that a displacement field as well as a rotation field are attached to the Cosserat surface, both of which are assumed to be independent of each other. The rotation field is introduced by an orthogonal tensor $\boldsymbol{R} \in \mathrm{SO}(3)$ which is described by an exponential map

$$\boldsymbol{R} = \exp(\boldsymbol{\Omega}) = \boldsymbol{1} + \boldsymbol{\Omega} + \frac{\boldsymbol{\Omega}^2}{2!} + \frac{\boldsymbol{\Omega}^3}{3!} + \cdots = \boldsymbol{1} + \frac{\sin|\boldsymbol{\omega}|}{|\boldsymbol{\omega}|}\boldsymbol{\Omega} + \frac{1-\cos|\boldsymbol{\omega}|}{|\boldsymbol{\omega}|^2}\boldsymbol{\Omega}^2 \tag{2.37}$$

with $\boldsymbol{\Omega} = -\boldsymbol{\Omega}^T$, and with $\boldsymbol{\omega} \in \mathbb{R}^3$ to be the corresponding axial vector of $\boldsymbol{\Omega}$.

For any $\boldsymbol{\gamma} \in \mathbb{R}^3$, it has a closed expression

$$\boldsymbol{R\gamma} = \boldsymbol{\gamma} + \frac{\sin|\boldsymbol{\omega}|}{|\boldsymbol{\omega}|}(\boldsymbol{\omega} \times \boldsymbol{\gamma}) + \frac{1-\cos|\boldsymbol{\omega}|}{|\boldsymbol{\omega}|^2}(\boldsymbol{\omega} \times (\boldsymbol{\omega} \times \boldsymbol{\gamma})) \tag{2.38}$$

If $\boldsymbol{\gamma}$ coincides with $\boldsymbol{\omega}$, the relation gives

$$\boldsymbol{R\omega} = \boldsymbol{\omega} \tag{2.39}$$

So $\boldsymbol{\omega}$ is an eigenvector of $\boldsymbol{R}$. If we use the rotation $\equiv \boldsymbol{\omega} \times \mathbf{1}$, where $\mathbf{1}$ is the identity tensor, the relation is obtained $\boldsymbol{\Omega\gamma} = (\boldsymbol{\omega} \times \mathbf{1})\boldsymbol{\gamma} = \boldsymbol{\omega} \times \boldsymbol{\gamma}$.

Furthermore, taking the derivative of the relation $\boldsymbol{RR}^T = \mathbf{1}$, one has

$$\boldsymbol{R}^T\boldsymbol{R}_{,\alpha} + \boldsymbol{R}_{,\alpha}^T\boldsymbol{R} = \mathbf{0} \tag{2.40}$$

Notice that $\boldsymbol{R}^T\boldsymbol{R}_{,\alpha} \in so(3)$, where $so(3)$ is the tangent space of SO(3), which defines the Lie algebra (*Hall, 2003*), that consists of all the skew-symmetric tensors. Let $\boldsymbol{k}_\alpha$ be the axial vector of $\boldsymbol{R}^T\boldsymbol{R}_{,\alpha}$, then one can get the relation

$$\boldsymbol{k}_\alpha = \frac{\sin|\boldsymbol{\omega}|}{|\boldsymbol{\omega}|}\boldsymbol{\omega}_{,\alpha} + \frac{1-\cos|\boldsymbol{\omega}|}{|\boldsymbol{\omega}|^2}\boldsymbol{\omega}_{,\alpha} \times \boldsymbol{\omega} + \left(\frac{1}{|\boldsymbol{\omega}|} - \frac{\sin|\boldsymbol{\omega}|}{|\boldsymbol{\omega}|^2}\right)\frac{(\boldsymbol{\omega} \cdot \boldsymbol{\omega}_{,\alpha})}{|\boldsymbol{\omega}|}\boldsymbol{\omega} \tag{2.41}$$

$\boldsymbol{k}_\alpha$ is related to $\boldsymbol{\omega}$ which is the eigenvector of $\boldsymbol{R}$.

Variation of $\boldsymbol{R}$ can be given by left or right multiplications

$$\delta\boldsymbol{R} = \boldsymbol{YR} = \boldsymbol{RL} \tag{2.42}$$

where $\boldsymbol{L}$ and $\boldsymbol{Y}$ are both skew-symmetric**.**

Let $\boldsymbol{l}$ and $\boldsymbol{y}$ be the axial vectors of $\boldsymbol{L}$ and $\boldsymbol{Y}$, the variation of $\boldsymbol{k}_\alpha$ can be derived by

$$\delta\boldsymbol{k}_\alpha = \text{axial}\left[\delta\left(\boldsymbol{R}^T\boldsymbol{R}_{,\alpha}\right)\right] = \text{axial}\left[\delta\boldsymbol{R}^T\boldsymbol{R}_{,\alpha} + \boldsymbol{R}^T\delta\boldsymbol{R}_{,\alpha}\right] \tag{2.43}$$

which means $\delta\boldsymbol{k}_\alpha \times \mathbf{1} = \delta\left(\boldsymbol{R}^T\boldsymbol{R}_{,\alpha}\right)$, and we have

$$\delta\boldsymbol{k}_\alpha = \text{axial}(-\boldsymbol{L}\boldsymbol{R}^T\boldsymbol{R}_{,\alpha} + \boldsymbol{R}^T\boldsymbol{R}_{,\alpha}\boldsymbol{L} + \boldsymbol{L}_{,\alpha}) \tag{2.44}$$

So

$$\delta\boldsymbol{k}_\alpha = \boldsymbol{k}_\alpha \times \boldsymbol{l} + \boldsymbol{l}_{,\alpha} \tag{2.45}$$

Similarly it can be derived that $\delta\boldsymbol{k}_\alpha = \boldsymbol{R}^T\boldsymbol{y}_{,\alpha}$.

2.3.3 Strain measures

The first Cosserat deformation tensor is

$$\boldsymbol{U} \coloneqq \boldsymbol{R}^T\boldsymbol{F} \tag{2.46}$$

And the second Cosserat deformation tensor is

$$\boldsymbol{\mathcal{K}} \coloneqq -\boldsymbol{k}_{\alpha} \otimes \boldsymbol{G}^{\alpha} \tag{2.47}$$

Alternatively, $\boldsymbol{\mathcal{K}}$ can be written as

$$\boldsymbol{\mathcal{K}} = -\frac{1}{2}\boldsymbol{\varepsilon} : \boldsymbol{R}^{T}\boldsymbol{R}_{,\boldsymbol{\alpha}} \otimes \boldsymbol{G}^{\alpha} \tag{2.48}$$

where (:) denotes a double contraction; the relation holds $\boldsymbol{A} : \boldsymbol{B} = \mathrm{tr}(\boldsymbol{A}\boldsymbol{B}^{T})$, where $\boldsymbol{A}$, $\boldsymbol{B}$ are two second order tensors and tr() is the trace operation.

A strain measure can be defined as $\overline{\boldsymbol{E}}$ that vanishes at the reference configuration

$$\overline{\boldsymbol{E}} \coloneqq \boldsymbol{U} - \boldsymbol{1} \tag{2.49}$$

where $\boldsymbol{U} = \boldsymbol{1}$ at the reference configuration.

The strain tensors can be decomposed with respect to the tangential base system at the reference configuration

$$\boldsymbol{U} = U_{\beta\alpha}\boldsymbol{G}^{\alpha} \otimes \boldsymbol{G}^{\beta} + U_{\alpha 3}\boldsymbol{N} \otimes \boldsymbol{G}^{\alpha} + U_{3\alpha}\boldsymbol{G}^{\alpha} \otimes \boldsymbol{N} + U_{33}\boldsymbol{N} \otimes \boldsymbol{N} \tag{2.50}$$

$$\boldsymbol{\mathcal{K}} = \mathcal{K}_{\beta\alpha}\boldsymbol{N} \times \boldsymbol{G}^{\alpha} \otimes \boldsymbol{G}^{\beta} + \mathcal{K}_{\alpha 3}\boldsymbol{N} \otimes \boldsymbol{G}^{\alpha} + \mathcal{K}_{3\alpha}\boldsymbol{G}^{\alpha} \otimes \boldsymbol{N} + \mathcal{K}_{33}\boldsymbol{N} \otimes \boldsymbol{N} \tag{2.51}$$

when writing the displacement and the rotation field in terms of Cartesian components

$$\boldsymbol{u} = u_k\boldsymbol{e}_k, \;\; \boldsymbol{\omega} = \omega_k\boldsymbol{e}_k \tag{2.52}$$

the strain measures can be finally expressed as

$$U_{\alpha\beta} = G_{\alpha\beta} + c_{\beta k}u_{k,\alpha} + (c_{\alpha k} + u_{k,\alpha})c_{\beta j}\left(\frac{\sin|\boldsymbol{\omega}|}{|\boldsymbol{\omega}|}e_{ijk}\omega_i + \frac{1-\cos|\boldsymbol{\omega}|}{|\boldsymbol{\omega}|^2}(\omega_k\omega_j - \omega_i\omega_i\delta_{jk})\right)$$

$$U_{\alpha 3} = c_{3k}u_{k,\alpha} + (c_{\alpha k} + u_{k,\alpha})\left(\frac{\sin|\boldsymbol{\omega}|}{|\boldsymbol{\omega}|}e_{ijk}\omega_i + \frac{1-\cos|\boldsymbol{\omega}|}{|\boldsymbol{\omega}|^2}(\omega_k\omega_j - \omega_i\omega_i\delta_{jk})\right)$$

$$U_{3\alpha} = 0$$

$$U_{33} = 1$$

$$\mathcal{K}_{\alpha\beta} = c_{\beta l}c_{3s}e_{kls}\left(\frac{\sin|\boldsymbol{\omega}|}{|\boldsymbol{\omega}|}\omega_{k,\alpha} + \frac{1-\cos|\boldsymbol{\omega}|}{|\boldsymbol{\omega}|^2}e_{ijk}\omega_{i,\alpha}\omega_j + \frac{|\boldsymbol{\omega}|-\sin|\boldsymbol{\omega}|}{|\boldsymbol{\omega}|^2}|\boldsymbol{\omega}|_{,\boldsymbol{\alpha}}\omega_{\boldsymbol{k}}\right)$$

$$\mathcal{K}_{\alpha 3} = -c_{3k}\left(\frac{\sin|\boldsymbol{\omega}|}{|\boldsymbol{\omega}|}\omega_{k,\alpha} + \frac{1-\cos|\boldsymbol{\omega}|}{|\boldsymbol{\omega}|^2}e_{ijk}\omega_{i,\alpha}\omega_j + \frac{|\boldsymbol{\omega}|-\sin|\boldsymbol{\omega}|}{|\boldsymbol{\omega}|^2}|\boldsymbol{\omega}|_{,\boldsymbol{\alpha}}\omega_{\boldsymbol{k}}\right)$$

$$\mathcal{K}_{3\alpha} = 0$$

$$\mathcal{K}_{33} = 0 \tag{2.53}$$

2.3.4 Principle of virtual work

In a pure mechanical theory, the internal potential function for the Cosserat surface depends on the two strain tensors $\boldsymbol{U}$ and $\boldsymbol{\mathcal{K}}$

$$\boldsymbol{\Phi}_{\text{int}}(\boldsymbol{U},\boldsymbol{\mathcal{K}}) = \int_{\mathcal{B}} \rho\,\phi_{\text{int}}(\boldsymbol{U},\boldsymbol{\mathcal{K}})dA \tag{2.54}$$

where ρ is the density of the surface. The force tensor and the couple tensor are defined as

$$\boldsymbol{S} \coloneqq \rho\frac{\partial\phi_{\text{int}}(\boldsymbol{U},\boldsymbol{\mathcal{K}})}{\partial\boldsymbol{U}} \tag{2.55}$$

$$\boldsymbol{T} \coloneqq \rho\frac{\partial\phi_{\text{int}}(\boldsymbol{U},\boldsymbol{\mathcal{K}})}{\partial\boldsymbol{\mathcal{K}}} \tag{2.56}$$

Notice that here $\boldsymbol{S}$ is the Boit-like stress tensor, which is different from but related with the first Piola-Kirchhoff stress tensor $\boldsymbol{S}_I$ in Equation (1.18) and the second Piola-Kirchhoff stress tensor $\boldsymbol{S}_{II}$ in Equation (1.8).

For the Cosserat surface, the principle of virtual work holds

$$\delta\boldsymbol{\Phi}_{\text{int}}(\boldsymbol{U},\boldsymbol{\mathcal{K}}) - \mathcal{W}_{ext} = 0 \tag{2.57}$$

While the external virtual work is defined as

$$\mathcal{W}_{ext} = \int_{\mathcal{B}}(\rho\,\boldsymbol{f}\cdot\delta\boldsymbol{u} + \rho\,\boldsymbol{q}\cdot\boldsymbol{l})dA + \int_{\partial\mathcal{B}}(\boldsymbol{f_s}\cdot\delta\boldsymbol{u} + \boldsymbol{q_s}\cdot\boldsymbol{l})ds \tag{2.58}$$

where ρ is the density at reference configuration, dA is the area element of the curved surface $\mathcal{B}$, and ds is the line element on its boundary $\partial\mathcal{B}$, $\boldsymbol{f}$ and $\boldsymbol{q}$ are the forces and torques on the surface, and $\boldsymbol{f_s}$ and $\boldsymbol{q_s}$ are corresponding forces on the boundary.

With these relations and

$$\boldsymbol{F} = \mathbf{1} + \boldsymbol{u}_{,\alpha} \otimes \boldsymbol{G}^{\alpha} \tag{2.59}$$

along with the geometric boundary conditions, equilibrium equations can be derived:

$$\int_{\mathcal{B}} \left[\rho \frac{\partial \phi_{\text{int}}(\boldsymbol{U},\boldsymbol{\mathcal{K}})}{\partial \boldsymbol{U}} : \delta\boldsymbol{U} + \rho \frac{\partial \phi_{\text{int}}(\boldsymbol{U},\boldsymbol{\mathcal{K}})}{\partial \boldsymbol{\mathcal{K}}} : \delta\boldsymbol{\mathcal{K}}\right] dA - \int_{\mathcal{B}} (\rho\, \boldsymbol{f} \cdot \delta\boldsymbol{u} + \rho\, \boldsymbol{q} \cdot \boldsymbol{l}) dA$$

$$- \int_{\partial\mathcal{B}} (\boldsymbol{f_s} \cdot \delta\boldsymbol{u} + \boldsymbol{q_s} \cdot \boldsymbol{l}) ds = 0 \tag{2.60}$$

$$\int_{\mathcal{B}} (\boldsymbol{S} : \delta\boldsymbol{U} + \boldsymbol{T} : \delta\boldsymbol{\mathcal{K}}) dA - \int_{\mathcal{B}} (\rho\, \boldsymbol{f} \cdot \delta\boldsymbol{u} + \rho\, \boldsymbol{q} \cdot \boldsymbol{l}) dA - \int_{\partial\mathcal{B}} (\boldsymbol{f_s} \cdot \delta\boldsymbol{u} + \boldsymbol{q_s} \cdot \boldsymbol{l}) ds$$

$$= 0 \tag{2.61}$$

The first and second variations of the strain measure $\boldsymbol{U}$ are

$$\delta\boldsymbol{U} = \delta\boldsymbol{R}^{\boldsymbol{T}}\boldsymbol{F} + \boldsymbol{R}^{\boldsymbol{T}}\delta\boldsymbol{F} = -\boldsymbol{L}\boldsymbol{R}^{\boldsymbol{T}}\boldsymbol{F} + \boldsymbol{R}^{\boldsymbol{T}}\delta\boldsymbol{F} \tag{2.62}$$

$$\delta^2\boldsymbol{U} = \boldsymbol{L}\boldsymbol{Y}\boldsymbol{R}^{\boldsymbol{T}}\boldsymbol{F} - \boldsymbol{L}\boldsymbol{R}^{\boldsymbol{T}}\Delta\boldsymbol{F} - \boldsymbol{Y}\boldsymbol{R}^{\boldsymbol{T}}\delta\boldsymbol{F} \tag{2.63}$$

The first and second variations of strain measure $\boldsymbol{\mathcal{K}}$ can be defined by

$$\delta\boldsymbol{\mathcal{K}} = \mathrm{D}\boldsymbol{\mathcal{K}}(\boldsymbol{R};\boldsymbol{l}) = -(\boldsymbol{k}_{\alpha} \times \boldsymbol{l} + \boldsymbol{l}_{,\boldsymbol{\alpha}}) \otimes \boldsymbol{G}^{\alpha} \tag{2.64}$$

$$\delta^2\boldsymbol{\mathcal{K}} = \mathrm{D}^2\boldsymbol{\mathcal{K}}(\boldsymbol{R};\boldsymbol{l},\boldsymbol{y}) = -(\boldsymbol{k}_{\alpha} \times \boldsymbol{y}) \times \boldsymbol{l} \otimes \boldsymbol{G}^{\alpha} - (\boldsymbol{y}_{,\boldsymbol{\alpha}} \times \boldsymbol{l}) \otimes \boldsymbol{G}^{\alpha} \tag{2.65}$$

So

$$\boldsymbol{S} : \delta\boldsymbol{U} + \boldsymbol{T} : \delta\boldsymbol{\mathcal{K}} = \boldsymbol{R}\boldsymbol{S} : \left(\delta\boldsymbol{u}_{,\alpha} \otimes \boldsymbol{G}^{\alpha}\right) + \boldsymbol{S} : \delta\boldsymbol{R}^{\boldsymbol{T}}\boldsymbol{R}\boldsymbol{U} + \frac{1}{2}\boldsymbol{T}$$

$$: \left[\boldsymbol{\varepsilon} : \delta\left(\boldsymbol{R}^{\boldsymbol{T}}\boldsymbol{R}_{,\boldsymbol{\alpha}} \otimes \boldsymbol{G}^{\alpha}\right)\right]$$

$$\boldsymbol{T} : \left[\boldsymbol{\varepsilon} : \left(\boldsymbol{R}^{\boldsymbol{T}}\boldsymbol{R}_{,\alpha} \otimes \boldsymbol{G}^{\alpha}\right)\right] = \boldsymbol{T}\boldsymbol{G}^{\alpha} \cdot \left[\boldsymbol{\varepsilon} : \left(\boldsymbol{R}^{\boldsymbol{T}}\boldsymbol{R}_{,\alpha}\right)\right] = \left[\boldsymbol{\varepsilon} \cdot \left(\boldsymbol{T}\boldsymbol{G}^{\alpha}\right)\right] : \left(\boldsymbol{R}^{\boldsymbol{T}}\boldsymbol{R}_{,\alpha}\right)$$

$$\boldsymbol{S} : \delta\boldsymbol{U} + \boldsymbol{T} : \delta\boldsymbol{\mathcal{K}} = \boldsymbol{R}\boldsymbol{S}\boldsymbol{G}^{\alpha} \cdot \delta\boldsymbol{u}_{,\alpha} + \boldsymbol{U}\boldsymbol{S}^{\boldsymbol{T}} : \boldsymbol{R}^{\boldsymbol{T}}\delta\boldsymbol{R} + \frac{1}{2}\left[\boldsymbol{\varepsilon} \cdot \left(\boldsymbol{T}\boldsymbol{G}^{\alpha}\right)\right] : \delta\left(\boldsymbol{R}^{\boldsymbol{T}}\boldsymbol{R}_{,\alpha}\right)$$

We write $\boldsymbol{S}^{\alpha} = \boldsymbol{S}\boldsymbol{G}^{\alpha}$ and $\boldsymbol{T}^{\alpha} = \boldsymbol{T}\boldsymbol{G}^{\alpha}$, and so we have

$$\boldsymbol{S} : \delta\boldsymbol{U} + \boldsymbol{T} : \delta\boldsymbol{\mathcal{K}} = \boldsymbol{R}\boldsymbol{S}^{\alpha} \cdot \delta\boldsymbol{u}_{,\alpha} - \boldsymbol{R}\boldsymbol{S}\boldsymbol{F}^{\boldsymbol{T}} : \boldsymbol{L} + \boldsymbol{R}\boldsymbol{T}^{\alpha} \cdot \boldsymbol{l}_{,\alpha}$$

The vitual principle equation can be expressed as

$$\int_{\mathcal{B}} \left(\boldsymbol{R}\boldsymbol{S}^{\alpha} \cdot \delta\boldsymbol{u}_{,\alpha} - \boldsymbol{R}\boldsymbol{S}\boldsymbol{F}^{\boldsymbol{T}} : \boldsymbol{L} + \boldsymbol{R}\boldsymbol{T}^{\alpha} \cdot \boldsymbol{l}_{,\alpha}\right) dA - \int_{\mathcal{B}} \left(\rho\, \boldsymbol{f} \cdot \delta\boldsymbol{u} + \rho\, \boldsymbol{q} \cdot \boldsymbol{l}\right) dA$$

$$- \int_{\partial\mathcal{B}} \left(\boldsymbol{f}_{\boldsymbol{s}} \cdot \delta\boldsymbol{u} + \boldsymbol{q}_{\boldsymbol{s}} \cdot \boldsymbol{l}\right) ds = 0 \tag{2.66}$$

Since $\boldsymbol{R}\boldsymbol{S}\boldsymbol{F}^{\boldsymbol{T}} : \boldsymbol{L} = \left(-\boldsymbol{L}\boldsymbol{R}\boldsymbol{S}^{\alpha} \otimes \boldsymbol{x}_{,\alpha}\right) : \boldsymbol{1} = -\left(\boldsymbol{l} \times \boldsymbol{R}\boldsymbol{S}^{\alpha}\right) \cdot \boldsymbol{x}_{,\alpha} = \left(\boldsymbol{x}_{,\alpha} \times \boldsymbol{R}\boldsymbol{S}^{\alpha}\right) \cdot \boldsymbol{l}$

and with the use of the divergence theorem, it becomes

$$\int_{\mathcal{B}} \left[-\frac{1}{G}\left(\sqrt{G}\boldsymbol{R}\boldsymbol{S}^{\alpha}\right)_{,\alpha} \cdot \delta\boldsymbol{u} - \left(\boldsymbol{x}_{,\alpha} \times \boldsymbol{R}\boldsymbol{S}^{\alpha}\right) \cdot \boldsymbol{l} + \frac{1}{G}\left(\sqrt{G}\boldsymbol{R}\boldsymbol{T}^{\alpha}\right)_{,\alpha} \cdot \boldsymbol{l}\right] dA$$

$$+ \int_{\partial\mathcal{B}} \left(\boldsymbol{R}\boldsymbol{S}^{\alpha}\mu_{\alpha} \cdot \delta\boldsymbol{u} - \boldsymbol{R}\boldsymbol{T}^{\alpha}\mu_{\alpha} \cdot \boldsymbol{l}\right) ds - \int_{\mathcal{B}} \left(\rho\, \boldsymbol{f} \cdot \delta\boldsymbol{u} + \rho\, \boldsymbol{q} \cdot \boldsymbol{l}\right) dA$$

$$- \int_{\partial\mathcal{B}} \left(\boldsymbol{f}_{\boldsymbol{s}} \cdot \delta\boldsymbol{u} + \boldsymbol{q}_{\boldsymbol{s}} \cdot \boldsymbol{l}\right) ds = 0 \tag{2.67}$$

μ_{α} are the components of the external normal vector at the boundary $\partial\mathcal{B}$ which lies on the tangent plane of $\mathcal{B}$.

Because $\delta\boldsymbol{u}$ and $\boldsymbol{l}$ are free variations, we have the localized governing equations for the equilibrium, the Euler-Lagrange equations in $\mathcal{B}$,

$$\frac{1}{G}\left(\sqrt{G}\boldsymbol{R}\boldsymbol{S}^{\alpha}\right)_{,\alpha} + \boldsymbol{f} = \boldsymbol{0} \tag{2.68}$$

$$\boldsymbol{x}_{,\alpha} \times \boldsymbol{R}\boldsymbol{S}^{\alpha} - \frac{1}{G}\left(\sqrt{G}\boldsymbol{R}\boldsymbol{T}^{\alpha}\right)_{,\alpha} + \rho\, \boldsymbol{q} = \boldsymbol{0} \tag{2.69}$$

which can be alternatively expressed as

$$\boldsymbol{R}^{\boldsymbol{T}}\boldsymbol{x}_{,\boldsymbol{\alpha}} \times \boldsymbol{S}^{\alpha} - \frac{1}{G}(\sqrt{G}\boldsymbol{T}^{\alpha})_{,\boldsymbol{\alpha}} - \boldsymbol{k}_{\alpha} \times \boldsymbol{T}^{\alpha} + \rho\, \boldsymbol{R}^{\boldsymbol{T}}\boldsymbol{q} = \boldsymbol{0} \tag{2.70}$$

and we also get the natural boundary conditions on $\partial\mathcal{B}$

$$\boldsymbol{R}\boldsymbol{S}^{\alpha}\mu_{\alpha} = \boldsymbol{f}_{\boldsymbol{s}} \tag{2.71}$$

$$\boldsymbol{R}\boldsymbol{T}^{\alpha}\mu_{\alpha} = -\boldsymbol{q}_{\boldsymbol{s}} \tag{2.72}$$

2.4 **Potentials**

The mechanical properties of CNTs are largely determined by the interatomic forces, which are governed by the chemical bonds, which are expressed in terms of interatomic potential models. An ideal potential model should be able to accurately describe the interactions which bind the atoms together.

Empirical potentials are used extensively, which take simple forms of atomic positions alone, which provide great advantages in theoretical simulations. Many interatomic potential models have been developed and reported in the literature, some of them are simple, while some of them are relatively complicated. Using different potential models can result in totally different results. *Wu et al.* (*2008*) pointed out that the use of two generations of Brenner potentials results in totally opposite results in modelling the critical strains of CNTs in tension, as shown in Figure 2.4, where $n = 0$ represents the axisymmetric bifurcation, and $n = 1,2,3$ ... represents the nonaxisymmetric bifurcation. Even by using the same potential model, the use of different parameters leads to a big difference as well. *Wang et al.* (*2006*) demonstrated the difference in modelling Young's modulus of CNTs by using two sets of parameters in Tersoff-Brenner potential, as shown in Figure 2.5.

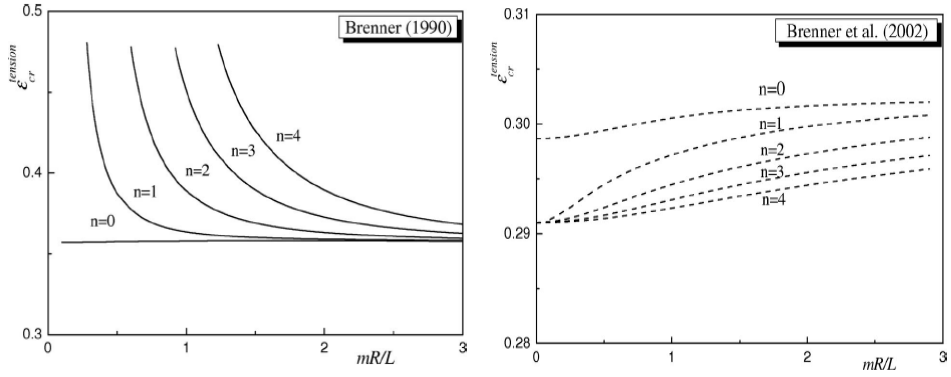

Figure 2-4: Opposite results in modelling critical strain of CNTs in tension by using two generations of Brenner potential (*Wu et al. 2008*)

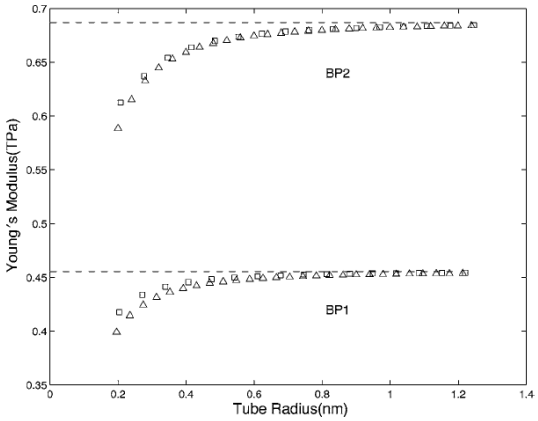

Figure 2-5: Difference of Young's modulus of CNTs by using two sets of parameters in Tersoff-Brenner potential (*Wang et al. 2006*)

That gives us an idea why the theoretical results of the mechanical properties of CNTs exhibit a large scatter, and why we should choose the empirical potential model carefully. Basically, potentials are chosen for different targets in examining different material properties that one wants to study. Therefore, how complicated a potential one chooses depends on what kind of properties it is capable to reproduce. In this research, two types of potentials are chosen for one-dimensional rod modelling and two-dimensional surface modelling, respectively. For one-

dimensional atomic chain modelling, a simple atomistic potential form is chosen based on a force field. For two-dimensional CNT shell modelling, a more complicated second generation REBO potential is chosen.

2.4.1 Atomistic potential based on a force field

Rappi et al. (*1992*) gave a full periodic table force field for a molecular mechanics study. They presented the potential energy of a molecule expressed as a superposition of various bonded interactions and non-bonded interactions of the form

$$V = V_r + V_\theta + V_\phi + V_\omega + V_{vdw} + V_{el} \tag{2.73}$$

Bonded interactions include all the interactions of the atom with its neighbouring atoms. V_r is the bond stretch energy, V_θ is the bond angle bending energy which describes the angular distortions, V_ϕ is the dihedral angle torsion and V_ω is the inversion torsion term. Non-bonded interactions are V_{vdw} that describes the interaction caused by van der Waals forces, and V_{el} that involves the electrostatic interactions.

Bond stretch energy can be expressed as

$$V_r = \frac{1}{2} k_{IJ}(r - r_{IJ})^2 \tag{2.74}$$

or with Morse function

$$V_r = D_{IJ1}\left[e^{-\alpha(r-r_{IJ})} - 1\right]^2 \tag{2.75}$$

k_{IJ} is the force constant, D_{IJ} is the bond dissociation energy, and r_{IJ} is the original bond length .

Angle bond energy for a bond angle θ is given as

$$V_\theta = K_{IJK} \sum_{n=0}^{m} C_n \cos(n\theta) \tag{2.76}$$

which simplifies to

$$V_\theta = \frac{K_{IJK}}{n^2}[1 - \cos(n\theta)] \tag{2.77}$$

The torsion potential for a torsion angle ϕ_{IJKL} is also expressed as a small cosine Fourier expansion

$$V_\phi = K_{IJKL} \sum_{n=0}^{m} C_n \cos(n\phi_{IJKL}) \tag{2.78}$$

where C_n is a shape factor.

The inversion term is given as

$$V_\omega = K_{IJKL}(C_0 + C_1 \cos\omega_{IJKL} + C_2 \cos 2\omega_{IJKL}) \tag{2.79}$$

Van der Waals force interaction is described by a Lennard-Jones 6-12 type expression

$$V_{vdw} = D_{IJ2}\left[-2\left(\frac{x_{IJ}}{x}\right)^6 + \left(\frac{x_{IJ}}{x}\right)^{12}\right] \tag{2.80}$$

where x_{IJ} is the distance between two non- bonded atoms.

Electrostatic interactions are expressed as

$$V_{el} = D_{ij}\left(\frac{Q_i Q_j}{\epsilon R_{ij}}\right) \tag{2.81}$$

where Q_i, Q_j are the charges and R_{ij} is the distance in angstroms.

Li and Chou (*2003*) modelled the deformation of CNTs via a structural mechanics approach, by considering the bonds between two atoms as a load bearing beam members. They built up the potential as the sum of the total energy due to valence of bonded interactions and nonbonded interactions

$$\sum V = \sum (V_r + V_\theta + V_\phi + V_\omega + V_{vdw} + V_{el}) \tag{2.82}$$

They pointed out that the harmonic approximation is good enough to describe the energy when the system undergoes small deformations, so they applied the simplest harmonic forms of the energies and merged the dihedral angle torsion term and the inversion term into a single term, expressed as

$$V_r = \frac{1}{2} k_r (r - r_0)^2 \tag{2.83}$$

$$V_\theta = \frac{1}{2} k_\theta (\theta - \theta_0)^2 \tag{2.84}$$

$$V_\tau = V_\phi + V_\omega = \frac{1}{2} k_\tau (\phi - \phi_0)^2 \tag{2.85}$$

And they were the first ones to point out, through structural mechanics calculation, that the molecular material parameters k_r, k_θ and k_τ stand in direct relation with the structural mechanics parameters of the beam, which is given as

$$k_r = \frac{EA}{L}\,, \qquad k_\theta = \frac{EI}{L}\,, \qquad k_\tau = \frac{GJ}{L} \tag{2.86}$$

where EA, EI, and GJ are three stiffness parameters that describe the stretch, bending, and torsion properties of the beam member. This has been applied widely by researchers afterwards into the finite element modelling of CNTs by setting C-C bond elastic parameters with ANSYS or ABAQUS or other commercial finite element software.

Meo and Rossi (*2006*) proposed a finite element model to simulate mechanical properties of SWCNTs, by using non-linear spring elements to model carbon bonds.

They pointed out the effects of $V_\phi, V_\omega, V_{vdw}$and V_{el} can be neglected for uniaxial loading and small strain assumption, so they only used the first two terms in the energy form.

The bond energy is chosen as another expression of Morse potential

$$V_r = D_e\left\{\left[1 - e^{-\alpha(r-r_0)}\right]^2 - 1\right\} \tag{2.87}$$

with parameters for SWCNTs $r_0 = 0.139\text{nm}$, $D_e = 6.03105 \times 10^{-10}\text{N.nm}$ and $\alpha = 26.25\text{nm}^{-1}$.

The bond angle energy takes the form

$$V_\theta = \frac{1}{2}k_\theta(\theta - \theta_0)^2[1 + k_{sextic}(\theta - \theta_0)^4] \tag{2.88}$$

with the parameters $k_\theta = 0.9 \times 10^{-18}\text{N.m/rad}^2$, $\theta_0 = 2.094\text{rad}$ and $k_{sextic} = 0.754\ \text{rad}^{-4}$.

Avila and Lacerda (*2008*) evaluated Young's modulus and Poisson ratio of SWCNTs by the approach of *Li and Chou* (*2003*) using the relation between structural mechanics parameters and molecular material parameters. They implemented a macro subroutine into ANSYS V.10 and chose $k_r = 6.52 \times 10^{-7}\text{N/nm}$, $k_\theta = 8.76 \times 10^{-10}\text{N.nm/rad}^2$ and $k_\tau = 2.78 \times 10^{-10}\text{N.nm/rad}^2$.

Dun et al. (*2010*) applied a stick-spiral model to calculate the constitutive law for CNTs buckling analysis. They used the potential form

$$\sum V = \sum(V_r + V_\theta)$$

$$= \sum D_e\left\{\left[1 - e^{-\alpha(r-r_0)}\right]^2 - 1\right\} + \sum\frac{1}{2}k_\theta(\theta - \theta_0)^2 \tag{2.89}$$

with $D_e = 0.6031\text{nN.nm}$, $\alpha = 26.25\text{nm}^{-1}$ and $k_\theta = 1.42\text{nN.nm/rad}^2$.

Shokrieh and Rafiee (*2010*) considered the C-C bond as a beam element and studied Young's modulus of CNTs by adopting the potential

$$\sum V = \sum (V_r + V_\theta) = \sum \frac{1}{2} k_r (r - r_0)^2 + \sum \frac{1}{2} k_\theta (\theta - \theta_0)^2 \tag{2.90}$$

with $k_r = 6.52 \times 10^{-7}\text{N/nm}$ and $k_\theta = 8.76 \times 10^{-10}\text{N.nm/rad}^2$.

Parvaneh and Shariati (*2011*) studied the effects of defects and loading on the prediction of Young's modulus of SWCNTs. They adopted the energy form

$$\sum V = \sum (V_r + V_\theta + V_\phi + V_\omega) \tag{2.91}$$

with

$$V_r = D_e \left\{ \left[1 - e^{-\alpha (r - r_0)} \right]^2 - 1 \right\} \tag{2.92}$$

$$V_\theta = \frac{1}{2} k_\theta (\theta - \theta_0)^2 [1 + k_{sextic} (\theta - \theta_0)^4] \tag{2.93}$$

$$V_\phi = \frac{1}{2} k_\phi [1 + \cos(n\phi - \phi_0)] \tag{2.94}$$

$$V_\omega = \frac{1}{2} k_\omega [1 + \cos(n\omega - \omega_0)] \tag{2.95}$$

where $k_\theta = 1.42\text{nN.nm/rad}^2$ and $k_\phi = k_\omega = 0.0418\text{nN.nm}$. They took the dihedral angle torsion and out-of plane torsion into consideration.

Finally, an atomistic potential is chosen in this research by considering the bond stretch energy and the bond angle energy. And the torsion energy is considered in one-dimensional deformation embedded in a three-dimensional space. For one-dimensional deformation embedded in a two-dimensional space, the potential is taking to be

$$\sum V = \sum (V_r + V_\theta)$$

$$= \sum D_e \left\{ \left[1 - e^{-\alpha(r-r_0)} \right]^2 - 1 \right\} + \sum \frac{1}{2} k_\theta (\theta - \theta_0)^2 \qquad (2.96)$$

where $D_e = 0.6031\text{nN.nm}$, $\alpha = 26.25\text{nm}^{-1}$ and $k_\theta = 1.42\text{nN.nm/rad}^2$.

For one-dimensional deformation in a three-dimensional space case, the potential is expressed as

$$\sum V = \sum (V_r + V_\theta + V_\tau)$$

$$= \sum D_e \left\{ \left[1 - e^{-\alpha(r-r_0)} \right]^2 - 1 \right\} + \sum \frac{1}{2} k_\theta (\theta - \theta_0)^2$$

$$+ \sum \frac{1}{2} k_\tau (\phi - \phi_0)^2 \qquad (2.97)$$

where $D_e = 0.6031\text{nN.nm}$, $\alpha = 26.25\text{nm}^{-1}$, $k_\theta = 8.76 \times 10^{-10}\text{N.nm/rad}^2$ and $k_\tau = 2.78 \times 10^{-10}\text{N.nm/rad}^2$.

2.4.2 Potential form for SWCNT

In early stages, the potentials used for molecular mechanics were empirical isotropic pair potentials, e.g. Lennard-Jones potential, Morse potential, etc. They take the form

$$V_{total} = \sum_i \sum_{j>i} V(r_{IJ}) \qquad (2.98)$$

while $V(r_{IJ}) = 0$ when $r_{IJ} > r_c$. r_c is a cut-off radius. In these models, the potential only depends on the distance between two atoms, and does not consider the information about the environment of the atom. For example, Morse potential is given by

$$V(r_{IJ}) = D_e \left[\exp\{-2\alpha(r_{IJ} - r_0)\} - 2\exp\{-\alpha(r_{IJ} - r_0)\} \right] \qquad (2.99)$$

Such potentials were used extensively because of their simplicity. However, these models suffer a major drawback because they do not depend on the atom's environment, which gives no difference for a bulk atom and a surface atom. Therefore, they are inappropriate to apply for Cosserat surface.

In order to involve the bond angle and the neighbouring atoms of a selected atom, more complicated bond order potential forms were developed, among which Tersoff and Brenner's models were proved to be successful.

Brenner (*1990*) presented a Tersoff-Brenner interatomic potential for carbon as

$$V_{REBO} = \sum_{i} \sum_{j=i+1} \left[V_R(r_{IJ}) - \bar{b}_{IJ} V_A(r_{IJ}) \right] \tag{2.100}$$

For atoms I and J, where r_{IJ} is the distance between atoms I and J, V_R and V_A are the repulsive and attractive pair terms given by

$$V_R(r) = \frac{D^{(e)}}{S-1} e^{-\sqrt{2S}\beta\left(r-R^{(e)}\right)} f_c(r) \tag{2.101}$$

$$V_A(r) = \frac{D^{(e)} S}{S-1} e^{-\sqrt{\frac{2}{S}}\beta\left(r-R^{(e)}\right)} f_c(r) \tag{2.102}$$

The parameter $D^{(e)}$, S, β and $R^{(e)}$ are determined from the known physical properties of carbon. The function f_c is merely a smooth cutoff function to limit the range of the potential, and is given by

$$f_c(r) = \begin{cases} 1 & r < R^1 \\ \frac{1}{2}\left(1 + \cos\left(\frac{\pi(r-R^1)}{R^2-R^1}\right)\right) & R^1 < r < R^2 \\ 0 & r > R^2 \end{cases} \tag{2.103}$$

$R^1 = 0.17\text{nm}$ and $R^2 = 0.2\text{nm}$ is chosen as cutoff radius by *Zhang et al.* (*2002*).

The parameter $\bar{b}_{IJ}$ represents a multi-body coupling between the bond from atom I to atom J and the local environment of atom I, and is given by

$$\bar{b}_{IJ} = \left[1 + \sum_{K(\neq I,J)} G(\theta_{IJK}) f_c(r_{IK})\right]^{-\delta} \tag{2.104}$$

where r_{IK} is the distance between atom I and K, f_c is the cutoff function, θ_{IJK} is the angle between bonds *I-J* and *I-K*, and the function G is given by

$$G(\theta) = a_0\left[1 + \frac{{c_0}^2}{{d_0}^2} - \frac{{c_0}^2}{{d_0}^2 + (1+\cos\theta)^2}\right] \tag{2.105}$$

Two sets of parameters for carbon which is given by Brenner (1990):

1. $D^{(e)} = 6.325eV$, $S = 1.29$, $\beta = 15nm^{-1}$, $R^{(e)} = 0.1315nm$, $\delta = 0.80469$, $a_0 = 0.011304$, $c_0 = 19$, $d_0 = 2.5$
2. $D^{(e)} = 6.000eV$, $S = 1.22$, $\beta = 21nm^{-1}$, $R^{(e)} = 0.1390nm$, $\delta = 0.50000$, $a_0 = 0.00020813$, $c_0 = 330$, $d_0 = 3.5$

which gives the equilibrium bond length of CNTs as 0.142 and 0.145nm from the two sets of parameters respectively (*Zhang et al. 2002*).

Bao et al. (*2004*) applied a second-generation reactive empirical bond order (REBO) potential energy expression for hydrocarbons presented by *Brenner* (*2002*). In the REBO potential, the total potential energy of the system is given by

$$V_{REBO} = \sum_i \sum_{j=i+1} \left[V_R(r_{IJ}) - \bar{b}_{IJ} V_A(r_{IJ})\right] \tag{2.106}$$

where r_{IJ} is the distance between atoms *I* and *J*, and $\bar{b}_{IJ}$ is a many-body empirical bond order term. V_R and V_A are repulsive and attractive terms.

$$V_R(r) = f_c(r)\left(1 + \frac{Q}{r}\right) A\exp(-\alpha r) \tag{2.107}$$

$$V_A(r) = f_c(r)\sum_{n=1}^{3} B_n e^{-\beta_n r} \tag{2.108}$$

f_c is a cut-off function which is given by

$$f_c(r) = \begin{cases} 1 & r < R_1 \\ \left\{1 + \cos\left[\dfrac{\pi(r - R_1)}{R_2 - R_1}\right]\right\}/2 & R_1 < r < R_2 \\ 0 & r > R_2 \end{cases} \tag{2.109}$$

which is used to cut off the interactions when atoms become too close, where $R_2 = 0.26\text{nm}$ and $R_1 = 0.17\text{nm}$.

Brenner et al. (*2002*) gave the parameters for carbons as

$Q = 0.3134603\text{Å}$, $A = 10953.544\text{eV}$, $\alpha = 4.7465391\text{Å}^{-1}$, $B_1 = 12388.79\text{eV}$, $B_2 = 17.56741\text{eV}$, $B_3 = 30.71493\text{eV}$, $\beta_1 = 4.720452\text{Å}^{-1}$, $\beta_2 = 1.433213\text{Å}^{-1}$, $\beta_3 = 1.382691\text{Å}^{-1}$.

where $1\text{eV} = 1.602 \times 10^{-19}\text{N. m}$ and $1\text{Å} = 1 \times 10^{-10}\text{m}$.

The bond order function $\bar{b}_{IJ}$ is

$$\bar{b}_{IJ} = \frac{1}{2}\left(b_{IJ}^{\sigma-\pi} + b_{JI}^{\sigma-\pi}\right) + b_{IJ}^{RC} + b_{IJ}^{DH} \tag{2.110}$$

where

$$b_{IJ}^{\sigma-\pi} = \left[1 + \sum_{K(\neq I,J)} f_{cIK}\,(r_{IK}) G\left(\cos\theta_{IJK}\right)\right]^{-1/2} \tag{2.111}$$

$$G\left(\cos\theta_{IJK}\right) = \sum_{n=0}^{5} a_n \left(\cos\theta_{IJK}\right)^n \tag{2.112}$$

For $0^{\text{o}} < \theta < 109.47^{\text{o}}$, $a_0 = 0.27186$, $a_1 = 0.48922$, $a_2 = -0.43286$, $a_3 = -0.56140$, $a_4 = 1.27111$, $a_5 = -0.03793$.

For $109.47^{\text{o}} < \theta < 120^{\text{o}}$, $a_0 = 0.69669$, $a_1 = 5.54440$, $a_2 = 23.4320$, $a_3 = 55.9476$, $a_4 = 69.8760$, $a_5 = 35.3117$.

For $120^{\text{o}} < \theta < 180^{\text{o}}$, $a_0 = 0.28160$, $a_1 = 1.06200$, $a_2 = 2.13400$, $a_3 = 2.53000$, $a_4 = 1.55200$, $a_5 = 0.38560$.

$$b_{IJ}^{RC} = F_{IJ}\left(N_I^t, N_I^t, N_{IJ}^{conj}\right) \tag{2.113}$$

where F is a tricubic spline.

$$N_{IJ}^{conj} = 1 + \left[\sum_{K(\neq I,J)}^{carbon} f_{cIK}(r_{IK})H(x_{IK})\right]^2 + \left[\sum_{L(\neq I,J)}^{carbon} f_{cJL}(r_{JL})H(x_{JL})\right]^2 \quad (2.114)$$

$$H(x_{IK}) = \begin{cases} 1 & x_{IK} < 2 \\ [1 + \cos(2\pi(x_{IK} - 2)]/2 & 2 < x_{IK} < 3 \\ 0 & x_{IK} > 3 \end{cases} \quad (2.115)$$

with $x_{IK} = N_K^t - f_{cIK}(r_{IK})$, and

$$N_I^t = \sum_{K(\neq I,J)}^{carbon\ atoms} f_{cIK}(r_{IK}) \quad (2.116)$$

$$b_{IJ}^{DH} = T_{IJ}\left[\sum_{K(\neq I,J)}\sum_{L(\neq I,J)} (1 - \cos^2\Theta_{IJKL}) f_{cIK}(r_{IK}) f_{cJL}(r_{JL})\right] \quad (2.117)$$

$T_{IJ} = -0.00809675$ for C-C bonds. Θ_{IJKL} is the dihedral angle among four atoms, $\cos\Theta_{IJKL} = \boldsymbol{e}_{JIK} \cdot \boldsymbol{e}_{IJL}$ with $\boldsymbol{e}_{JIK} = \boldsymbol{R}_{JI} \times \boldsymbol{R}_{IK}$ and $\boldsymbol{e}_{IJL} = \boldsymbol{R}_{IJ} \times \boldsymbol{R}_{JL}$.

Since b_{IJ}^{RC} attributes to various radical energies, such as vacancies, it can be neglected in this research, and b_{IJ}^{DH} describes the conjugate terms of the interactions between *I*-*J* bond, which is also neglected for the computation.

2.5 The finite element approach

2.5.1 The finite element formulation

The governing equations of the Cosserat surface in shell theory have been derived in Section 2.4. With the energy forms chosen from Section 2.5, the internal potential can be write as $V(\boldsymbol{U}, \boldsymbol{\mathcal{K}})$.

We can reformulate

$$\int_{\mathcal{B}} (\boldsymbol{S} : \delta\boldsymbol{U} + \boldsymbol{T} : \delta\boldsymbol{\mathcal{K}}) dA - \int_{\mathcal{B}} (\rho\, \boldsymbol{f} \cdot \delta\boldsymbol{u} + \rho\, \boldsymbol{q} \cdot \boldsymbol{l}) dA - \int_{\partial\mathcal{B}} (\boldsymbol{f_s} \cdot \delta\boldsymbol{u} + \boldsymbol{q_s} \cdot \boldsymbol{l}) ds = 0 \tag{2.118}$$

as

$$\int_{\mathcal{B}} \left(\rho \frac{\partial V(\boldsymbol{U}, \boldsymbol{\mathcal{K}})}{\partial \boldsymbol{U}} : \delta\boldsymbol{U} + \rho \frac{\partial V(\boldsymbol{U}, \boldsymbol{\mathcal{K}})}{\partial \boldsymbol{\mathcal{K}}} : \delta\boldsymbol{\mathcal{K}} \right) dA - \int_{\mathcal{B}} (\rho\, \boldsymbol{f} \cdot \delta\boldsymbol{u} + \rho\, \boldsymbol{q} \cdot \boldsymbol{l}) dA - \int_{\partial\mathcal{B}} (\boldsymbol{f_s} \cdot \delta\boldsymbol{u} + \boldsymbol{q_s} \cdot \boldsymbol{l}) ds = 0 \tag{2.119}$$

To build a finite element formulation, we introduce the Euclidean vectors

$$\boldsymbol{u} \coloneqq \begin{Bmatrix} u_1 \\ u_2 \\ u_3 \\ \omega_1 \\ \omega_2 \\ \omega_3 \end{Bmatrix} \tag{2.120}$$

$$\boldsymbol{C}^U(\boldsymbol{u}) \coloneqq \begin{Bmatrix} U_{11}(\boldsymbol{u}) \\ U_{21}(\boldsymbol{u}) \\ U_{12}(\boldsymbol{u}) \\ U_{22}(\boldsymbol{u}) \\ U_{13}(\boldsymbol{u}) \\ U_{23}(\boldsymbol{u}) \end{Bmatrix} \text{ and } \boldsymbol{C}^{\mathcal{K}}(\boldsymbol{u}) \coloneqq \begin{Bmatrix} \mathcal{K}_{11}(\boldsymbol{u}) \\ \mathcal{K}_{21}(\boldsymbol{u}) \\ \mathcal{K}_{12}(\boldsymbol{u}) \\ \mathcal{K}_{22}(\boldsymbol{u}) \\ \mathcal{K}_{13}(\boldsymbol{u}) \\ \mathcal{K}_{23}(\boldsymbol{u}) \end{Bmatrix} \tag{2.121}$$

where $\omega_{1,2,3}$ are the components of $\boldsymbol{\omega}$ that is the eigenvector of the rotation tensor $\boldsymbol{R}$.

Define $\boldsymbol{\Phi}_{ext}$ as the external potential with the relation $\delta\boldsymbol{\Phi}_{ext} = -\mathcal{W}_{ext}$.

Equation (2.119) can now be written as

$$\int_{\mathcal{B}} \left(\rho \frac{\partial V(\boldsymbol{U}(\boldsymbol{u}), \boldsymbol{\mathcal{K}}(\boldsymbol{u}))}{\partial \boldsymbol{C}^{\mathcal{K}}(\boldsymbol{u})} \cdot \mathrm{D}\boldsymbol{C}^{\mathcal{K}}(\boldsymbol{u}; \delta\boldsymbol{u}) + \rho \frac{\partial V(\boldsymbol{U}(\boldsymbol{u}), \boldsymbol{\mathcal{K}}(\boldsymbol{u}))}{\partial \boldsymbol{C}^{U}(\boldsymbol{u})} \cdot \mathrm{D}\boldsymbol{C}^{U}(\boldsymbol{u}; \delta\boldsymbol{u}) \right) dA + \mathrm{D}\boldsymbol{\Phi}_{ext}(\boldsymbol{u}; \delta\boldsymbol{u}) = 0 \tag{2.122}$$

$$\mathrm{D}\boldsymbol{\Phi}_{ext}(\boldsymbol{u}; \delta\boldsymbol{u}) = -\int_{\mathcal{B}} (\rho\, \boldsymbol{f}(\boldsymbol{u}) \cdot \delta\boldsymbol{u} + \rho\, \boldsymbol{q} \cdot \boldsymbol{l}) dA - \int_{\partial\mathcal{B}} (\boldsymbol{f_s}(\boldsymbol{u}) \cdot \delta\boldsymbol{u} + \boldsymbol{q_s} \cdot \boldsymbol{l}) ds$$

$$\boldsymbol{q}\cdot\boldsymbol{l}=\frac{1}{2}\boldsymbol{Q}:\boldsymbol{L}\ ;\quad \boldsymbol{q_s}\cdot\boldsymbol{l}=\frac{1}{2}\boldsymbol{Q_s}:\boldsymbol{L} \tag{2.123}$$

where $\boldsymbol{Q}=\boldsymbol{q}\times\mathbf{1}$, similarly $\boldsymbol{Q_s}=\boldsymbol{q_s}\times\mathbf{1}$.

$$\boldsymbol{L}=\boldsymbol{R}^T\delta\boldsymbol{R}=\boldsymbol{l}\times\mathbf{1} \tag{2.124}$$

$$\boldsymbol{l}=\frac{\sin|\boldsymbol{\omega}|}{|\boldsymbol{\omega}|}\delta\boldsymbol{\omega}+\frac{1-\cos|\boldsymbol{\omega}|}{|\boldsymbol{\omega}|^2}\delta\boldsymbol{\omega}\times\boldsymbol{\omega}+\left(\frac{1}{|\boldsymbol{\omega}|}-\frac{\sin|\boldsymbol{\omega}|}{|\boldsymbol{\omega}|^2}\right)\frac{(\boldsymbol{\omega}\cdot\delta\boldsymbol{\omega})}{|\boldsymbol{\omega}|}\boldsymbol{\omega} \tag{2.125}$$

Let

$$\widehat{\boldsymbol{q}}(\boldsymbol{\omega})=\frac{\sin|\boldsymbol{\omega}|}{|\boldsymbol{\omega}|}\mathbf{1}+\frac{1-\cos|\boldsymbol{\omega}|}{|\boldsymbol{\omega}|^2}\mathbf{1}\times\boldsymbol{\omega}+\left(\frac{1}{|\boldsymbol{\omega}|}-\frac{\sin|\boldsymbol{\omega}|}{|\boldsymbol{\omega}|^2}\right)\frac{(\boldsymbol{\omega}\cdot\mathbf{1})}{|\boldsymbol{\omega}|}\boldsymbol{\omega} \tag{2.126}$$

then the external work can be expressed as

$$\mathrm{D}\boldsymbol{\Phi}_{ext}(\boldsymbol{u};\delta\boldsymbol{u})=-\int_{\mathcal{B}}(\rho\,\boldsymbol{f}(\overline{\boldsymbol{u}})\cdot\delta\overline{\boldsymbol{u}}+\rho\,\widehat{\boldsymbol{q}}(\boldsymbol{\omega})\cdot\delta\boldsymbol{\omega})dA$$

$$-\int_{\partial\mathcal{B}}(\boldsymbol{f_s}(\overline{\boldsymbol{u}})\cdot\delta\overline{\boldsymbol{u}}+\widehat{\boldsymbol{q}}_{\boldsymbol{s}}(\boldsymbol{\omega})\cdot\delta\boldsymbol{\omega})ds \tag{2.127}$$

$$\mathrm{D}\boldsymbol{\Phi}_{ext}(\boldsymbol{u};\delta\boldsymbol{u})=-\int_{\mathcal{B}}\boldsymbol{p}(\boldsymbol{u})\cdot\delta\boldsymbol{u}\ dA-\int_{\partial\mathcal{B}}\boldsymbol{p_s}(\boldsymbol{u})\cdot\delta\boldsymbol{u}\,ds \tag{2.128}$$

where vector $\boldsymbol{p}$ is the generalized force corresponding to $\boldsymbol{u}$.

2.5.2 Updating method

The updating method is designed to be path independent, following the approach presented by *Sansour and Wagner* (*2003*).

At one loading step, equilibrium equations are in displacement field $\boldsymbol{u}_i$ and rotation field $\boldsymbol{R}_i$, with changing of external loading, new state of equilibrium established in new kinematical fields $\boldsymbol{u}_{i+1}$ and $\boldsymbol{R}_{i+1}$. The update of displacement field naturally goes like

$$\boldsymbol{u}_i^j=\boldsymbol{u}_i^{j-1}+\Delta\boldsymbol{u}^j \tag{2.129}$$

here, j is the iteration step, and i is load step.

The rotation increment can be obtained by $\Delta\boldsymbol{R} = \Delta\boldsymbol{L}\boldsymbol{R} = \boldsymbol{R}\Delta\boldsymbol{Y} = \exp(\Delta\boldsymbol{L})$. But the rotation tensor itself cannot be interpolated, only its rotation parameters can. Since $\boldsymbol{R} = \boldsymbol{1}$ at the reference configuration, let rotation vector $\boldsymbol{\omega}_i^{j-1}$ be given at nodel points, where $\boldsymbol{\omega} = \boldsymbol{0}$ at the reference configuration. Instead of $\boldsymbol{R}_i^j = \Delta\boldsymbol{R}\,\boldsymbol{R}_i^{j-1}$, corresponding $\Delta\boldsymbol{l}$ and $\boldsymbol{\omega}_i^j$ can describe rotation tensor with parameters at nodal points which can be interpolated in a classical way.

Quaternion is used to relate a product $\boldsymbol{ab}$ of two vectors $\boldsymbol{a}$ and $\boldsymbol{b}$, expressed as

$$\boldsymbol{ab} = \boldsymbol{a}\cdot\boldsymbol{b} + \mathrm{i}(\boldsymbol{a}\times\boldsymbol{b}) \tag{2.130}$$

where i is a complex number with $\mathrm{i}^2 = -1$.

In the quaternion language, the rotation tensor can be written as $\boldsymbol{R} = \alpha + \mathrm{i}\boldsymbol{\beta}$ and $\boldsymbol{R}^T = \alpha - \mathrm{i}\boldsymbol{\beta}$, and we have $\boldsymbol{R}\boldsymbol{R}^T = \alpha^2 + \boldsymbol{\beta}^2 = \boldsymbol{1}$, which means α and $\boldsymbol{\beta}$ are not independent.

Set

$$\alpha = \cos\left(\frac{|\boldsymbol{\omega}|}{2}\right) \tag{2.131}$$

$$\boldsymbol{\beta} = \sin\left(\frac{|\boldsymbol{\omega}|}{2}\right)\frac{\boldsymbol{\omega}}{|\boldsymbol{\omega}|} \tag{2.132}$$

Let α and $\boldsymbol{\beta}$ at an iteration step j be α_j and $\boldsymbol{\beta}_j$, and let α and $\boldsymbol{\beta}$ for the iteration step be α_Δ and $\boldsymbol{\beta}_\Delta$, we have

$$\alpha_j = \cos\left(\frac{|\boldsymbol{\omega}_j|}{2}\right) \quad \boldsymbol{\beta}_j = \sin\left(\frac{|\boldsymbol{\omega}_j|}{2}\right)\frac{\boldsymbol{\omega}_j}{|\boldsymbol{\omega}_j|}$$

$$\alpha_\Delta = \cos\left(\frac{|\Delta\boldsymbol{\omega}|}{2}\right) \quad \boldsymbol{\beta}_\Delta = \sin\left(\frac{|\Delta\boldsymbol{\omega}|}{2}\right)\frac{\Delta\boldsymbol{\omega}}{|\Delta\boldsymbol{\omega}|} \tag{2.133}$$

Then the updated rotation tensor is

$$\boldsymbol{R}_i^{j+1} = \Delta\boldsymbol{R}\,\boldsymbol{R}_i^j = (\alpha_\Delta + \mathrm{i}\boldsymbol{\beta}_\Delta)(\alpha_j + \mathrm{i}\boldsymbol{\beta}_j)$$
$$= (\alpha_\Delta\alpha_j - \boldsymbol{\beta}_\Delta \cdot \boldsymbol{\beta}_j) + \mathrm{i}(\alpha_\Delta\boldsymbol{\beta}_j + \alpha_j\boldsymbol{\beta}_\Delta - \boldsymbol{\beta}_\Delta \times \boldsymbol{\beta}_j)$$
$$= \alpha_{j+1} + \mathrm{i}\boldsymbol{\beta}_{j+1} \tag{2.134}$$

Then $\boldsymbol{\omega}$ can be interpolated in the classical way.

2.5.3 Four node element interpolation

The constitutive relations are determined by derivatives of the potentials chosen in Section 2.5. The finite element equations are based on the formulation of Equation (2.122). Four node elements are chosen, and same bi-linear interpolations are set for all components of $\boldsymbol{u}$ and $\boldsymbol{\omega}$. The natural co-ordinates ϑ^α on the surface are defined as

$$\vartheta^1(\chi,\zeta) = \sum_{\mathrm{I}=1}^{4} N^{\mathrm{I}}(\chi,\zeta)\,\vartheta_{\mathrm{I}}^{1e}$$
$$\vartheta^2(\chi,\zeta) = \sum_{\mathrm{I}=1}^{4} N^{\mathrm{I}}(\chi,\zeta)\,\vartheta_{\mathrm{I}}^{2e} \tag{2.135}$$

where $\vartheta^{1,2}(\chi,\zeta)$ define the co-ordinates of a point within the element. $\vartheta_{\mathrm{I}}^{1,2e}$ are the co-ordinates on the edges of the element. $N^{\mathrm{I}}(\chi,\zeta)$ are the shape functions defined as

$$N^{\mathrm{I}}(\chi,\zeta) = \frac{1}{4}(1+\chi\chi_{\mathrm{I}})(1+\zeta\zeta_{\mathrm{I}}) \quad (\mathrm{I} = 1,2,3,4) \tag{2.136}$$

with $(\chi_{\mathrm{I}},\zeta_{\mathrm{I}}) \in \{(\text{-}1,\text{-}1);(1,\text{-}1);(1,1);(\text{-}1,1)\}$ and $(\chi,\zeta) \in [\text{-}1,1]\times[\text{-}1,1]$.

For four node element, the displacement field, as well as the rotation field of the element is in matrix

$$\boldsymbol{u}(\chi,\zeta) = \boldsymbol{Q}(\chi,\zeta)\boldsymbol{u}^e \tag{2.137}$$

$\boldsymbol{u}^e$ is $\boldsymbol{u}$ at the nodal points of the element. With four nodes and six degrees of freedom on each node, $\boldsymbol{u}^e \in \mathbb{R}^{24}$, and matrix $\boldsymbol{Q}$ consists of all the shape functions, $\boldsymbol{Q} \subset \mathbb{R}^{6\times 24}$.

The solution is achieved using Newton-Raphson iterative method, where the second derivative of potential $V(\boldsymbol{U}, \boldsymbol{\mathcal{K}})$ with respect to displacement field $\boldsymbol{u}$ must be evaluated, a very involved operation, the details of which are not presented here.

Chapter 3

Atomic Chain: Cosserat Curve

This chapter is meant as a preparation of a full analysis of carbon nanotube (CNT) as a cylindrical shell, where we consider a long slender CNT as an atomic chain model and simulates the deformations of the atomic chain as a one-dimensional straight line to a curve in two-dimensional space as well as in three-dimensional one. The equations for Cosserat curve are derived as a step-down of the general forms of equations in Section 2.3 for Cosserat surface. Atomic chains under bending, torsion and dynamic loadings are studied in section 3.4. This chapter aims to produce qualitative results in modelling CNTs' deformations from relatively simply one-dimensional Cosserat curve theory, meanwhile it builds a platform for further development of the quantitative physical meanings from atomic chain models.

3.1 **Atomic chain modelling**

This section presents a Cosserat curve background of the atomic chain model deforming from one-dimension (1-D) in a two-dimensional (2-D) plane, while the equations for a one-dimensional (1-D) Cosserat curve of a chain deforming in a three-dimensional (3-D) space can be simply derived from Section 2.3 by reducing α to 1.

Let us consider a point $\boldsymbol{X}$ in the $\boldsymbol{e}_1$- $\boldsymbol{e}_3$ plane laying on a curve $\mathcal{C}$ parameterised by the co-ordinate s. Then the position of $\boldsymbol{X}$ at certain time t is given by

$$\boldsymbol{x} = (s + u_1)\boldsymbol{H}^1 + u_3\boldsymbol{H}^3 = (s + u_1)\boldsymbol{G} + u_3\boldsymbol{N} \tag{3.1}$$

Where $\boldsymbol{G}$ is the tangent and $\boldsymbol{N}$ the normal vector at $\mathcal{C}$. The tangent vector at $\mathcal{C}$ in the reference configuration is expressed as

$$\boldsymbol{G} = \frac{\partial \boldsymbol{X}}{\partial s} = \boldsymbol{H}^1 \tag{3.2}$$

and in the current configuration as

$$\boldsymbol{g} = \frac{\partial \boldsymbol{x}}{\partial s} = \left(\frac{\partial s}{\partial s} + \frac{\partial u_1}{\partial s}\right)\boldsymbol{G} + \frac{\partial u_3}{\partial s}\boldsymbol{N} = \left(1 + u_{1,s}\right)\boldsymbol{H}^1 + u_{3,s}\boldsymbol{H}^3 = \boldsymbol{G} + \boldsymbol{u}_{,s} \tag{3.3}$$

where $u_{i,s}$ denote the Cartesian components of $\boldsymbol{u}_{,s}$.

The normal vector is given by

$$\boldsymbol{N} = \boldsymbol{G} \times \boldsymbol{e}_2 = \boldsymbol{H}^3 \tag{3.4}$$

For later usage, the natural basis vectors $\boldsymbol{H}^i$ are related to the Cartesian ones by

$$\boldsymbol{H}^i = c_j^i \boldsymbol{e}_j \tag{3.5}$$

with

$$c_j^i = \boldsymbol{H}^i \cdot \boldsymbol{e}_j$$

With the help of the tangent vectors in the current and reference configurations the deformation gradient is formulated as

$$\boldsymbol{F} = \boldsymbol{g} \otimes \boldsymbol{G} = F_{ij}\boldsymbol{H}^i \otimes \boldsymbol{H}^j = \begin{bmatrix} 1 + u_{1,s} & 0 \\ u_{3,s} & 0 \end{bmatrix} \boldsymbol{H}^i \otimes \boldsymbol{H}^j \quad (i,j = 1,2) \quad (3.6)$$

Or alternatively in the Cartesian frame

$$\boldsymbol{F} = \boldsymbol{g} \otimes \boldsymbol{G} = \begin{bmatrix} (c_1^1)^2 + c_1^1 u_{1,s} & c_1^1 c_3^1 + c_3^1 u_{1,s} \\ c_1^1 c_3^1 + c_1^1 u_{3,s} & (c_3^1)^2 + c_3^1 u_{3,s} \end{bmatrix} \quad (3.7)$$

Now the undeformed chord $\boldsymbol{A}$ is mapped to its deformed equivalent $\boldsymbol{a}$ via the deformation gradient and a rotation tensor $\boldsymbol{R}$, the latter accounts for the curvature of the curve $\mathcal{C}$:

$$\boldsymbol{R} = R_{ij}\boldsymbol{H}^i \otimes \boldsymbol{H}^j = \begin{bmatrix} \cos\omega & -\sin\omega \\ \sin\omega & \cos\omega \end{bmatrix} \quad (3.8)$$

Accordingly, we consider two strain measures, a stretch-like tensor

$$\boldsymbol{U} = \boldsymbol{R}^T\boldsymbol{F} = \begin{bmatrix} (1 + u_{1,s})\cos\omega + u_{3,s}\sin\omega & 0 \\ -(1 + u_{1,s})\sin\omega + u_{3,s}\cos\omega & 0 \end{bmatrix} \quad (3.9)$$

and a change of curvature tensor

$$\boldsymbol{\mathcal{K}} = \begin{bmatrix} \omega_{,s} & 0 \\ 0 & 0 \end{bmatrix} \quad (3.10)$$

This means, we have three kinematical relations to determine the three unknowns u_1, u_3 and ω. It is possible to neglect the stretch component U_{13}, if the number of unknowns is reduced by one. This can be achieved, if $\omega = f(u_{1,s}, u_{3,s})$ and $\boldsymbol{\mathcal{K}} = f(u_{1,ss}, u_{3,ss})$. However, in order to avoid the complexity of higher gradients and the requirement of an independent rotation tensor, $U_{13} \neq 0$ is necessary in this computation.

From Section 2.3, we know that, for the Cosserat surface, the covariant base vectors $\boldsymbol{G}_\alpha$ are

$$\boldsymbol{G}_\alpha = c_{\alpha i}\boldsymbol{e}^i\,, \qquad \boldsymbol{G}_\alpha \cdot \boldsymbol{e}_j = c_{\alpha j} \tag{3.11}$$

Cartesian co-ordinate vectors are related to the inverse base vector $\boldsymbol{G}^\beta$ by

$$\boldsymbol{G}_\alpha \cdot b_{j\beta}\boldsymbol{G}^\beta = c_{\alpha j} \tag{3.12}$$

$$b_{j\alpha} = c_{\alpha j}$$

$$\boldsymbol{e}_j = c_{\alpha j}\boldsymbol{G}^\alpha$$

along with (3.7) and (3.9) , we have

$$\boldsymbol{R}^T\left(\boldsymbol{G} + \boldsymbol{u}_{,s}\right) = c_{11}\left[\cos\omega\left(c_{11} + u_{1,s}\right) + \sin\omega\left(c_{13} + u_{3,s}\right)\right]\boldsymbol{H}^1 \otimes \boldsymbol{G}$$
$$+ c_{33}\left[-\sin\omega\left(c_{11} + u_{1,s}\right) + \cos\omega\left(c_{13} + u_{3,s}\right)\right]\boldsymbol{H}^3 \otimes \boldsymbol{G}$$

When the reference configuration is a straight line, it leads to $c_{11} = 1$ and $c_{13} = 0$.

From (3.9), the components of stretch tensor $\boldsymbol{U}$ can be expressed as

$$U_{11} = \cos\omega(1 + u_1') + \sin\omega\ u_3' \tag{3.13}$$

$$U_{13} = -\sin\omega(1 + u_1') + \cos\omega\ u_3' \tag{3.14}$$

where u_1' stands for $u_{1,s}$ and u_3' stands for $u_{3,s}$.

The variation of the strain energy density W_0 is expressed as

$$\delta W_0 = S_{11}\delta U_{11} + S_{13}\delta U_{13} + T\delta\kappa \tag{3.15}$$

where $\boldsymbol{S}$ is the force tensor and $\boldsymbol{T}$ is the couple tensor, and the couple tensor is a scalar in one-dimensional case.

$$S_{11} = \frac{\partial W_0}{\partial U_{11}} \tag{3.16}$$

$$S_{13} = \frac{\partial W_0}{\partial U_{13}} \tag{3.17}$$

$$T = \frac{\partial W_0}{\partial \kappa} \tag{3.18}$$

The variation of the strain energy density can be further obtained with the relations between the stretch tensor, the curvature tensor and the deformed configuration variables u_1, u_3 and ω:

$$\delta U_{11} = \frac{\partial U_{11}}{\partial u_1}\delta u_1 + \frac{\partial U_{11}}{\partial u_3}\delta u_3 + \frac{\partial U_{11}}{\partial \alpha}\delta\omega$$

$$= \cos\omega\ \delta u_1' + \sin\omega\ \ \delta u_3' + (-\sin\omega(1+u_1') + \cos\omega\ u_3')\delta\omega$$

$$\delta U_{13} = \frac{\partial U_{13}}{\partial u_1}\delta u_1 + \frac{\partial U_{13}}{\partial u_3}\delta u_3 + \frac{\partial U_{13}}{\partial \alpha}\delta\omega$$

$$= -\sin\omega\ \delta u_1' + \cos\omega\ \delta u_3' + (-\cos\omega(1+u_1') - \sin\omega u_3')\delta\omega$$

$$\delta\kappa = \delta\omega'$$

Similarly, the second variations can be derived

$$\Delta\delta U_{11} = \frac{\partial^2 U_{11}}{\partial u_1'\partial\omega}\Delta\omega\delta u_1' + \frac{\partial^2 U_{11}}{\partial u_3'\partial\omega}\Delta\omega\delta u_3' + \frac{\partial^2 U_{11}}{\partial\omega\partial u_1'}\Delta u_1'\delta\omega + \frac{\partial^2 U_{11}}{\partial\alpha\partial u_3'}\Delta u_3'\delta\omega$$

$$+ \frac{\partial^2 U_{11}}{\partial\omega\partial\omega}\Delta\omega\delta\omega$$

$$= -\sin\omega\ \Delta\omega\delta u_1' + \cos\omega\ \Delta\omega\delta u_3' - \sin\omega\ \Delta u_1'\delta\omega + \cos\omega\ \Delta u_3'\delta\omega$$

$$- (\cos\omega(1+u_1') + \sin\omega\ u_3')\Delta\omega\delta\omega$$

$$\Delta\delta U_{13} = \frac{\partial^2 U_{13}}{\partial u_1'\partial\omega}\Delta\omega\delta u_1' + \frac{\partial^2 U_{13}}{\partial u_3'\partial\omega}\Delta\omega\delta u_3' + \frac{\partial^2 U_{13}}{\partial\omega\partial u_1'}\Delta u_1'\delta\omega + \frac{\partial^2 U_{13}}{\partial\omega\partial u_3'}\Delta u_3'\delta\omega$$

$$+ \frac{\partial^2 U_{13}}{\partial\omega\partial\omega}\Delta\omega\delta\omega$$

$$= -\cos\omega\ \Delta\omega\delta u_1' - \sin\omega\ \ \Delta\omega\delta u_3'$$

$$- \cos\omega\ \Delta u_1'\delta\omega - \sin\omega\ \ \Delta u_3'\delta\omega + (\sin\omega(1+u_1')$$

$$- \cos\omega\ u_3')\Delta\omega\delta\omega$$

$$\Delta\delta\kappa = 0$$

The second variation of the strain energy density is

$$\Delta\delta W_0 = S_{11}\Delta\delta U_{11} + S_{31}\Delta\delta U_{13} + T\Delta\delta\kappa + \frac{\partial^2 V}{\partial U_{11}\partial U_{11}}\Delta U_{11}\delta U_{11} + \frac{\partial^2 V}{\partial U_{13}\partial U_{11}}\Delta U_{11}\delta U_{31} + \frac{\partial^2 V}{\partial\kappa\partial U_{11}}\Delta U_{11}\delta\kappa + \frac{\partial^2 V}{\partial U_{11}\partial U_{13}}\Delta U_{13}\delta U_{11} + \frac{\partial^2 V}{\partial U_{13}\partial U_{13}}\Delta U_{13}\delta U_{13} + \frac{\partial^2 V}{\partial\kappa\partial U_{13}}\Delta U_{13}\delta\kappa + \frac{\partial^2 V}{\partial U_{11}\partial\kappa}\Delta\kappa\delta U_{11} + \frac{\partial^2 V}{\partial U_{13}\partial\kappa}\Delta\kappa\delta U_{13} + \frac{\partial^2 V}{\partial\kappa\partial\kappa}\Delta\kappa\delta\kappa \tag{3.19}$$

where $\boldsymbol{n}$ is the stretch modulus like tensor and $\boldsymbol{m}$ is the bending modulus like tensor, where $\boldsymbol{m}$ in one-dimensional case is a scalar, and $\boldsymbol{n}_c$ is the couple modulus like tensor, which is the second derivative of the strain energy density over the strain tensor and the curvature tensor. The component of the stretch modulus like tensor in 11-11 direction gives the tension rigidity which is related to the tension modulus

$$n_{1111} = \frac{\partial^2 W_0}{\partial U_{11}\partial U_{11}} \tag{3.20}$$

The tensor-like bending modulus also known as bending rigidity is related to bending modulus

$$m = \frac{\partial^2 W_0}{\partial\kappa\partial\kappa} \tag{3.21}$$

The shear modulus is related to tensor-like stretch modulus 11-13 component

$$n_{1113} = \frac{\partial^2 W_0}{\partial U_{11}\partial U_{13}} \tag{3.22}$$

The principle of virtual work with total potential V_{total} holds

$$\delta V_{total} - \mathcal{W}_{ext} = 0 \tag{3.23}$$

where $\mathcal{W}_{ext}$ defines the external virtual work, which is given by

$$\mathcal{W}_{ext} = \int_l (\boldsymbol{f}\cdot\delta\boldsymbol{u} + M\,\delta\omega)\,ds \tag{3.24}$$

where $\boldsymbol{f}$ is the external force corresponding to displacement $\boldsymbol{u}$, and M is the external moment.

With two node element modelling atomic chain, the state of equilibrium can be achieved by updating $\boldsymbol{u}$ and α in the iterations, expressed as

$$\boldsymbol{u}_{i+1}^{j} = \boldsymbol{u}_{i+1}^{j-1} + \Delta\boldsymbol{u}^{j} \text{ , and } \omega_{i+1}^{j} = \omega_{i+1}^{j-1} + \Delta\omega^{j}$$

where i is the load step and j is the iteration step.

3.2 Atomic chain deformation in 2-D space

The strain energy density is the total strain energy per unit length

$$W_0 = \frac{1}{L}\sum V \tag{3.25}$$

where L is the length of the chain.

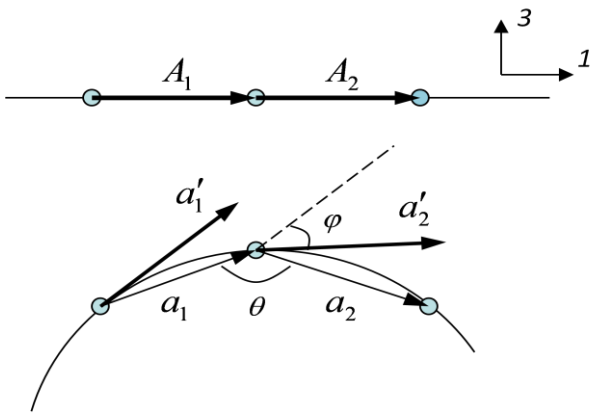

Figure 3-1: Sketch of 1-D atomic chain deforming in 2-D

With the atomic chain model, we consider the total potential V as the sum of the bond stretch energy V_r, the bond angle bending energy V_θ and an additional term V_{shear} which takes into account the shear effect out-of-palne.

$$V = V_r + V_\theta + V_{shear} = k_r(e^{-\alpha(r-r_0)} - 1)^2 + k_\theta(\theta - \theta_0)^2 + k_1 U_{13}^2 \quad (3.26)$$

The stretch energy is a function of the bond length r, and the bending energy is a function of the bond angle θ, as given by the force field mentioned in Section 2.4.1. The additional energy is a function of the shear component of the stretch tensor U_{13}.

Figure 3.1 shows a one-dimensional atomic chain deforming in two-dimensional space. According to the Cauchy-Born rule, the deformed vector on the tangent plane $\boldsymbol{a}'$ is

$$\boldsymbol{a}' = \boldsymbol{F}\boldsymbol{A} \quad (3.27)$$

We consider the real deformed vector at the chord of the curve $\boldsymbol{a}$ by a rotation of the tangent vector $\boldsymbol{a}'$ through an angle α. Then the length of $\boldsymbol{a}$ is

$$a = \sqrt{\boldsymbol{U}^T\boldsymbol{U}}\, A \quad (3.28)$$

In equation (3.26), the relation between the deformed bond length r and the reference bond length r_0 is

$$r = U_{11} r_0 \quad (3.29)$$

The bond angle θ in equation (3.26) can be obtained from

$$\theta = \pi - \kappa\, r \quad (3.30)$$

Then the total energy in equation (3.26) can be expressed as a function of U_{11}, U_{13} and κ.

The standard Cauchy-Born rule provides the change of the bond length via Equation (3.28), and the independent rotation tensor is related to the bond angle by Equation (3.30), the choosing of which is explained in Appendix B.

3.3 Atomic chain deformation in 3-D space

As shown in Figure 3.2, in a three-dimensional case, the atomic chain also deforms in direction 2, so in comparison to the potential in Equation (3.26), we have three more terms: V_ϕ is the torsion potential as mentioned in section 2.4.1, an additional shear energy term considering the shear effect from direction 1 to direction 2, and the spin energy for the rotation in the third dimension (longitudinal rotation).

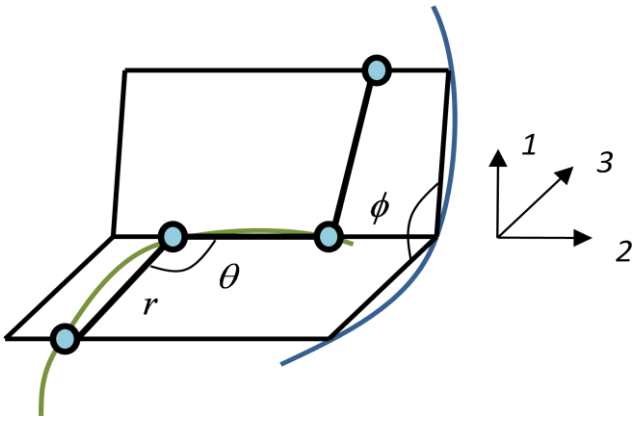

Figure 3-2: Sketch of 1-D atomic chain deforming in 3-D

$$V = V_r + V_\theta + V_\phi + V_{shear} + V_{spin}$$
$$= k_r(e^{-\alpha(r-r_0)} - 1)^2 + k_\theta(\theta - \theta_0)^2 + k_\tau(\phi - \phi_0)^2 + k_1 U_{12}^2$$
$$+ k_2 U_{13}^2 + k_3 \kappa_3^2 \qquad (3.31)$$

Same as in Equation (3.24) and (3.25), the bond length r and the bond angle θ can be obtained by

$$r = U_{11} r_0$$
$$\theta = \pi - \kappa_1 r \qquad (3.32)$$

The angle of the torsion ϕ is related to the second curvature variable κ_2

$$\phi = \pi - \kappa_2 \, r \tag{3.33}$$

Thus the total energy in Equation (3.31) can be expressed as a function of six variables U_{11}, U_{12}, U_{13}, κ_1, κ_2 and κ_3 .

3.4 Results and discussions

3.4.1 1-D to 2-D atomic chain simulation

Figure 3.3 is an atomic chain model with two fixed ends under uniform loading.

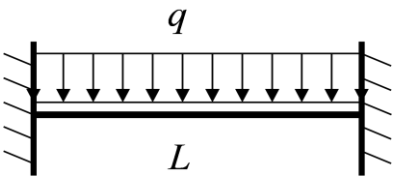

Figure 3-3: Atomic chain model with two fixed ends under uniform load

Figure 3-4: Deformation of atomic chain under small uniform load

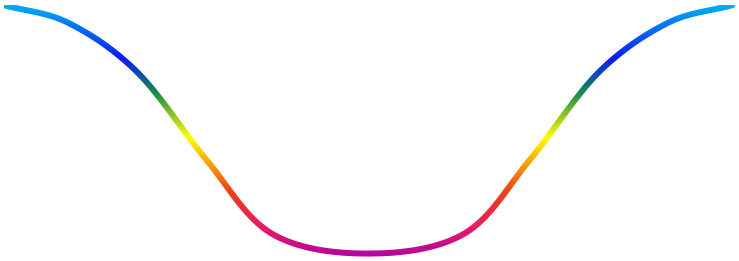

Figure 3-5: Deformation of atomic chain under large uniform load

Figure 3.4 gives the small deformation configuration of the chain under a small loading situation, and Figure 3.5 shows a large deformation configuration under a large loading situation which demonstrates highly non-linear behaviour. Figure 3.5 can be compared with an image of the non-linear behaviour which happens to a two fixed ended noodle stripe under pressure, it shows plastic-like behaviour, but the deformation is reversible.

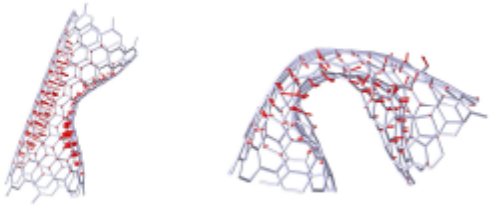

Figure 3-6: Deformation of CNTs under bending (*Huhtala et al. 2002*)

Huhtala et al. (*2002*) demonstrated the deformation of SWCNT under bending as shown in Figure 3.6. Their results of deformation of the top surface of simulated SWCNTs matches the configurations obtained from the atomic chain model.

Figure 3.7 shows an atomic chain model with one fixed end and one free end under a moment loading at the free end. Figure 3.8 gives the deformation of the chain under a small moment situation.

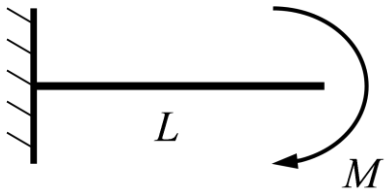

Figure 3-7: Cantilever atomic chain model under moment

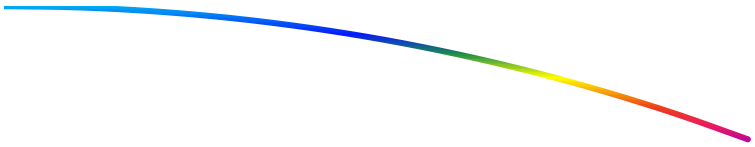

Figure 3-8: Deformation of atomic chain under small moment

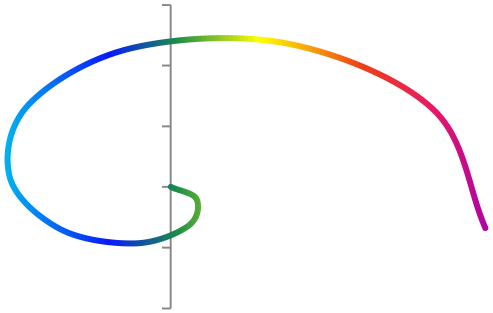

Figure 3-9: Deformation of atomic chain under large moment

The deformation in Figure 3.8 expresses a perfect arc, which fits in with the beam theory from classical continuum mechanics. With the moment increasing, it results in a very large deformation as shown in Figure 3.9. The chain model in Figure 3.9 can be imagined as bending a steel string fixed at its end, except, as well, the final deformation is reversible in this case.

As shown in Figure 3.4 and Figure 3.8, under small loading, the deformation of 1-D atomic chain is similar with the result of 1-D beam model obtained from classical continuum mechanics analysis. With the loading increasing, simulation shows that the atomic chain model is rather flexible and can exhibit very large deformed configurations, as demonstrated in Figure 3.5 and Figure 3.9. Non-

linear behaviour is involved in these large deformations, but they are reversible, i.e. still within the elastic range.

In the study of CNTs, the phenomena of large and reversible distorted configurations which involves no bond-breaking or atomic rearrangements, is called resilience response (*Hertel and Martel, 1998*). It is shown from the figures that the atomic chain model is different from a continuum beam model because the atomic chain can undergo large plastic-like deformations within the elastic range. CNTs also present a variety of these resilience behaviours. *Dai et al.* (*1996*) reported the experimental evidence of CNTs' resilience, which included the ability of CNT to reversibly undergo large non-linear deformations and also their ability to survive a crash during impact. A 1-D atomic chain model can be a qualitative model of CNT when it is considered as a 1-D Cosserat curve, provided the appropriate numerical values of the elastic constants of CNTs are incorporated in the potential forms.

3.4.2 Simulation of 1-D atomic chain in 3-D space

Figure 3.10 is an atomic chain fixed at one end under uniform loading. Figure 3.11 and Figure 3.12 show the deformation results of a 1-D chain in 3-D space and of a 1-D chain in a 2-D space separately.

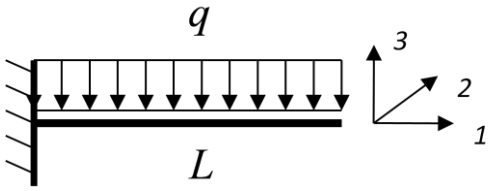

Figure 3-10: Cantilever atomic chain under uniform load

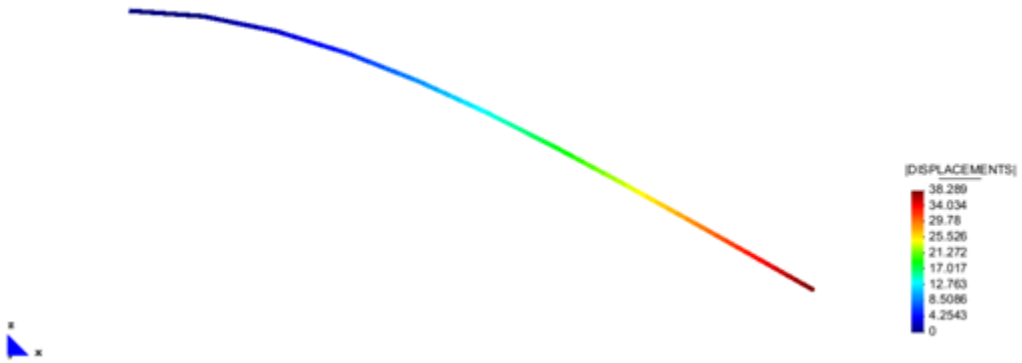

Figure 3-11: Cantilever atomic chain under uniform load in 3-D space

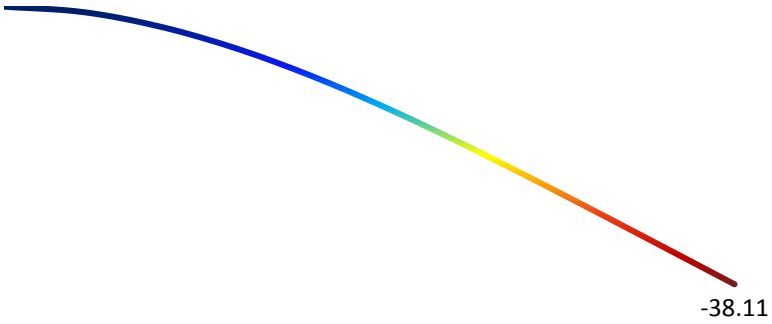

Figure 3-12: Cantilever atomic chain under uniform load in 2-D space

Similarly, Figure 3.13 is an atomic chain model with two hinged ends under uniform loading, and Figure 3.14 shows the deformation of a 1-D chain in 3-D space, whereas Figure 3.15 shows the result of a 1-D chain in 2-D space.

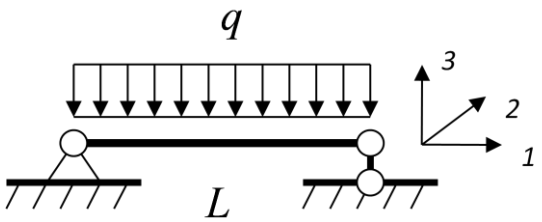

Figure 3-13: Atomic chain with two hinged ends under uniform load

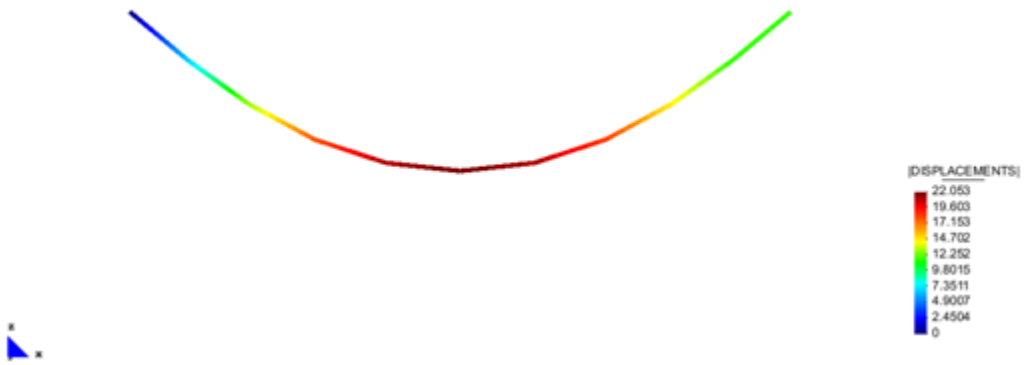

Figure 3-14: Deformation of atomic chain with two hinged ends under uniform load in 3-D space

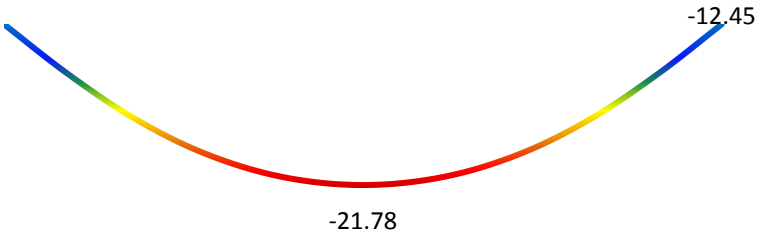

Figure 3-15: Deformation of atomic chain with two hinged ends under uniform load in 2-D space

Same as in Figure 3.7, Figure 3.16 is a cantilever model under moment at the free end in 3-D space. Figure 3.17 and Figure 3.18 demonstrate the deformations computed for 1-D chain model in 3-D space and 2-D space, respectively.

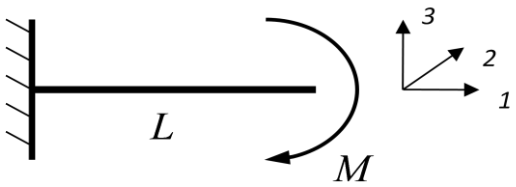

Figure 3-16: Cantilever atomic chain under moment

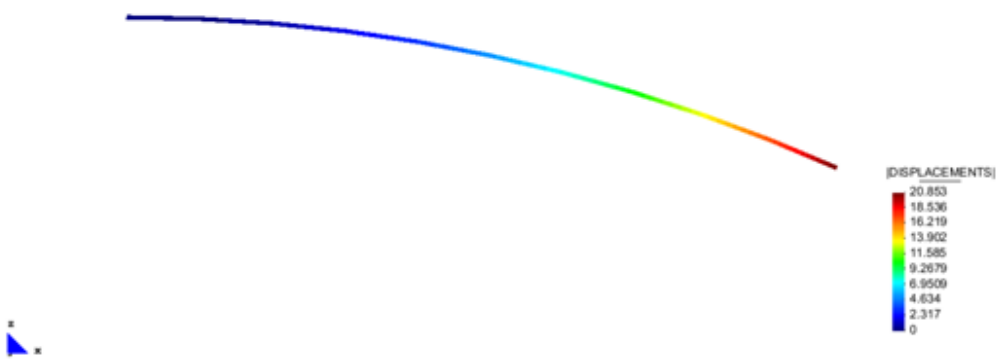

Figure 3-17: Deformation of cantilever atomic chain under moment in 3-D space

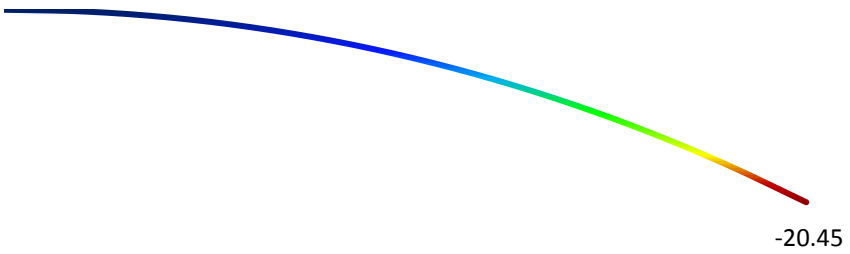

Figure 3-18: Deformation of cantilever atomic chain under moment in 2-D space

In all the cases, the displacements in the 3-D space give slightly larger values than the values in the case of 2-D space. This might be caused by two sets of different parameters applied in the potential forms in these two models, and also the added potential forms should have effects on the results of the final deformations as well. However, the differences are less than 1.0%, so the agreement between the results from the two atomic chain models is acceptable.

3.4.3 The atomic chain as a dynamic rod

A dynamic rod is modelled to simulate an atomic chain under dynamic loading, as shown in Figure 3.19. Atomic chain fixed at one end is modelled as a Cosserat curve, and four sets of moment loading are applied to the chain model in-plane and out-of-plane, the moments are twice larger as in the middle than at the end point of the chain, in order to make an obvious curve that is easier to observe in the results. The moment loadings change with time, increasing linearly to an assigned peak value and then decreasing linearly to zero, as is shown in Figure 3.19.

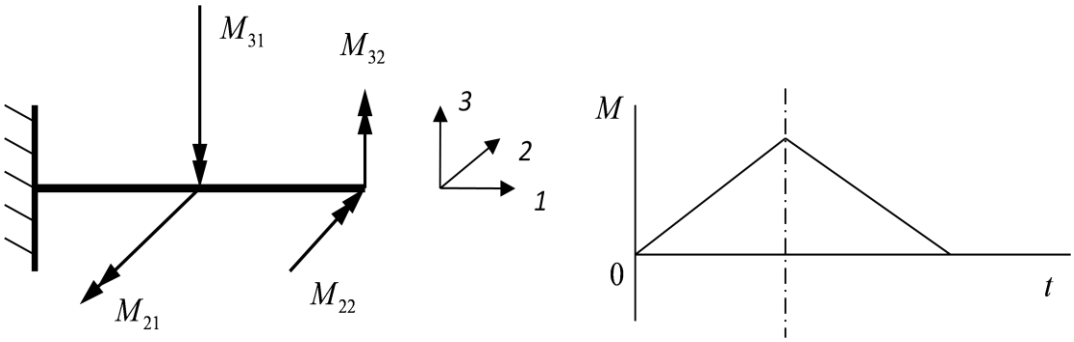

Figure 3-19: Atomic chain dynamic rod

The kinetic energy is chosen of the form

$$T = \frac{1}{2} m\, \dot{\boldsymbol{u}} \cdot \dot{\boldsymbol{u}} + \frac{1}{2} \boldsymbol{\Theta}\, \boldsymbol{\gamma} \cdot \boldsymbol{\gamma} \tag{3.34}$$

where m is the mass, $\dot{\boldsymbol{u}}$ is the velocity, $\boldsymbol{\Theta}$ is the moment of inertia, and $\boldsymbol{\gamma}$ is the rotational velocity, which holds relation of $\boldsymbol{\gamma} = \text{axial}\, \boldsymbol{\Gamma}$. $\boldsymbol{\Gamma}$ is the spin tensor, which is related to rotation tensor $\boldsymbol{R}$ from

$$\dot{\boldsymbol{R}} = \boldsymbol{\Gamma R} \quad \Rightarrow \quad \boldsymbol{\Gamma} = \dot{\boldsymbol{R}} \boldsymbol{R}^T \tag{3.35}$$

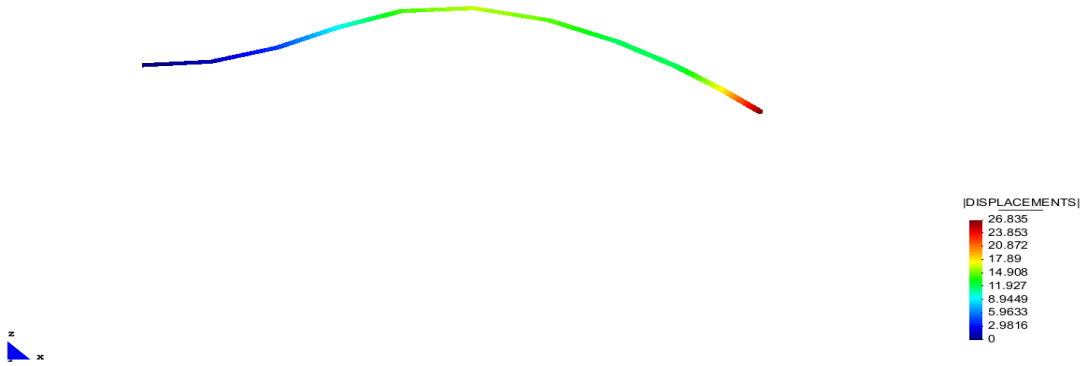

(a) Deformation of dynamic rod on 1-3 plane at time step 100

(b) Deformation of dynamic rod on 1-3 plane at time step 150

(c) Deformation of dynamic rod on 1-3 plane at time step 200

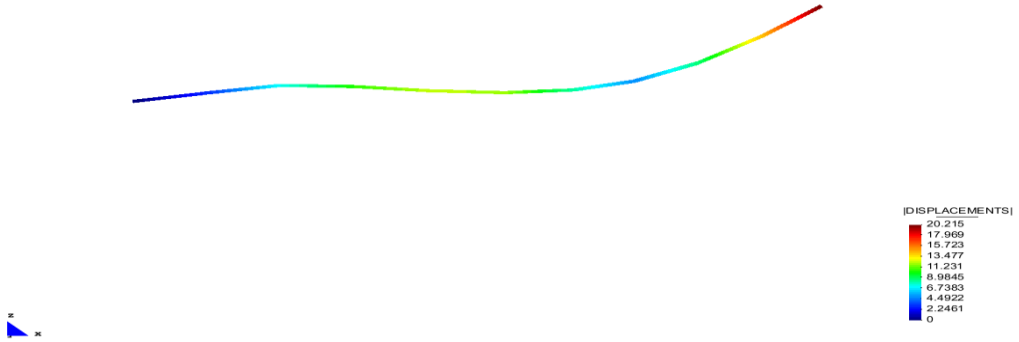

(d) Deformation of dynamic rod on 1-3 plane at time step 250

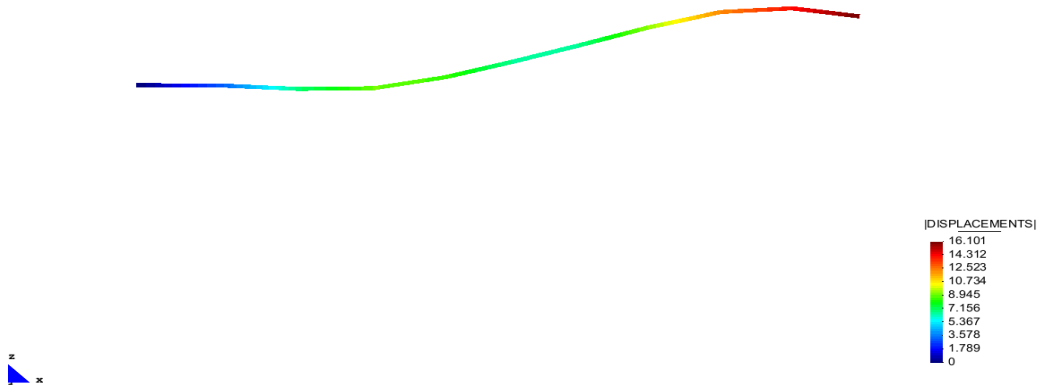

(e) Deformation of dynamic rod on 1-3 plane at time step 300

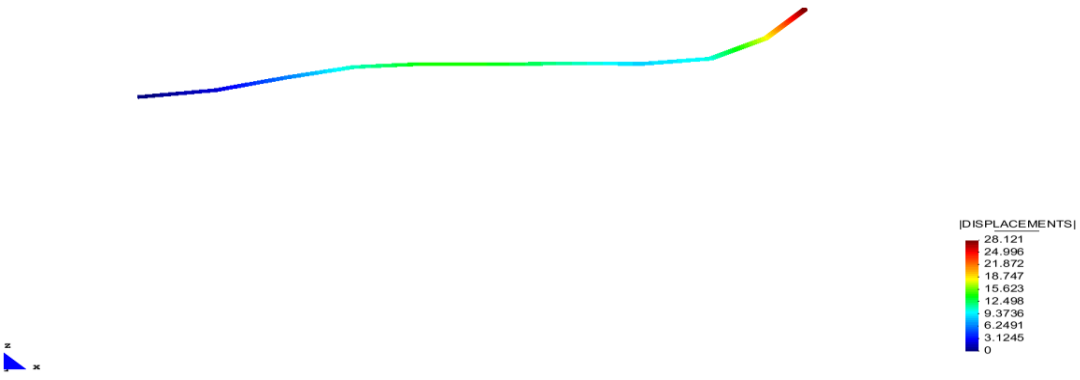

(f) Deformation of dynamic rod on 1-3 plane at time step 300

Figure 3-20: Deformation of dynamic rod on 1-3 plane

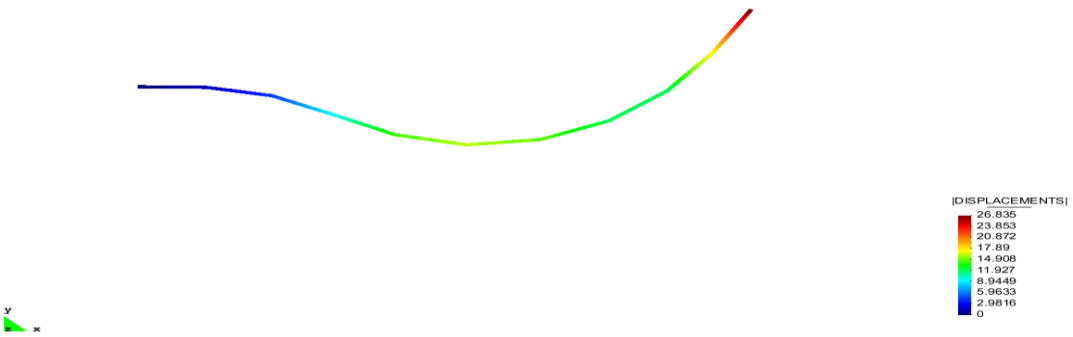

(a) Deformation of dynamic rod on 1-2 plane at time step 100

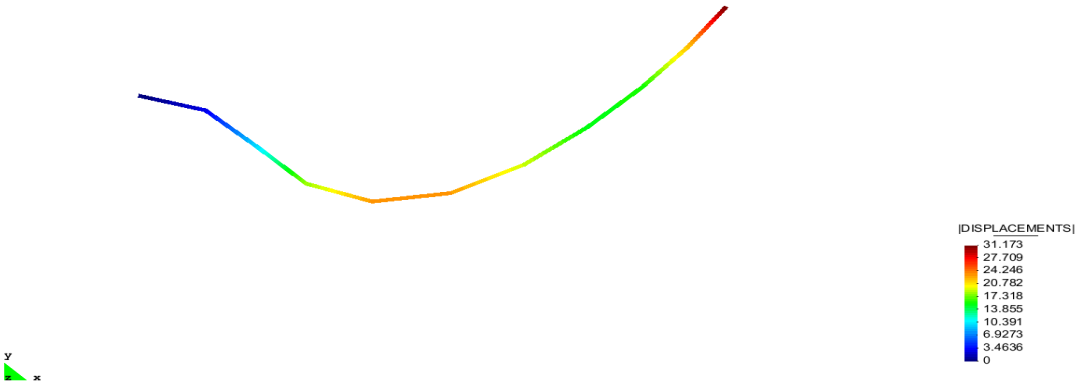

(b) Deformation of dynamic rod on 1-2 plane at time step 150

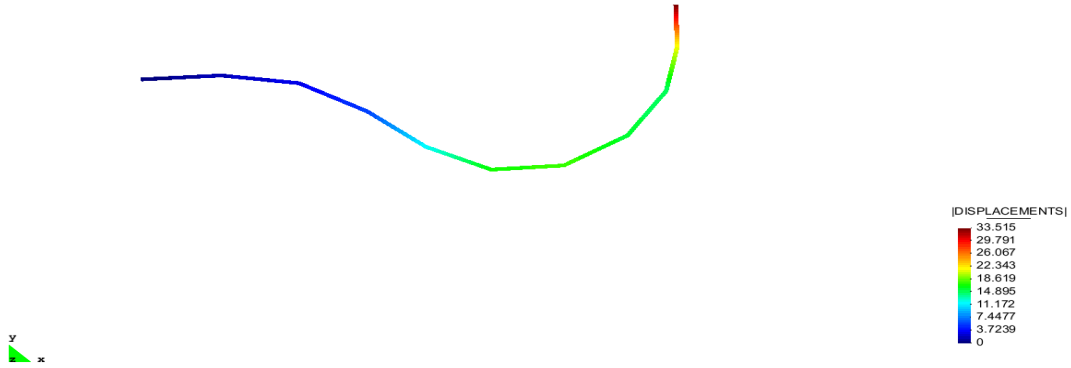

(c) Deformation of dynamic rod on 1-2 plane at time step 200

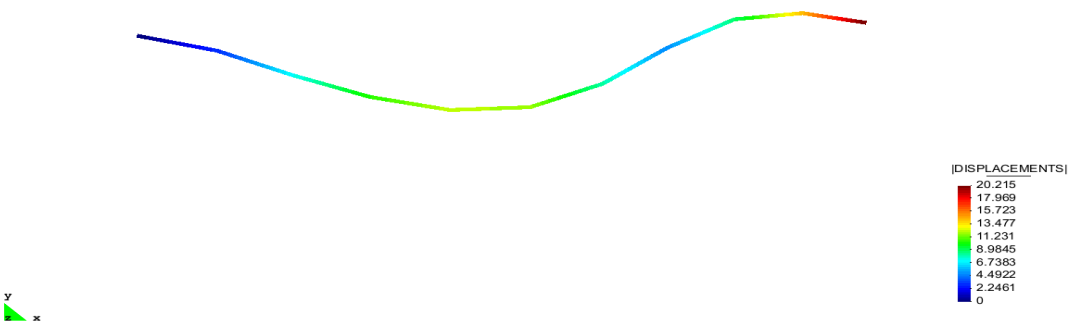

(d) Deformation of dynamic rod on 1-2 plane at time step 250

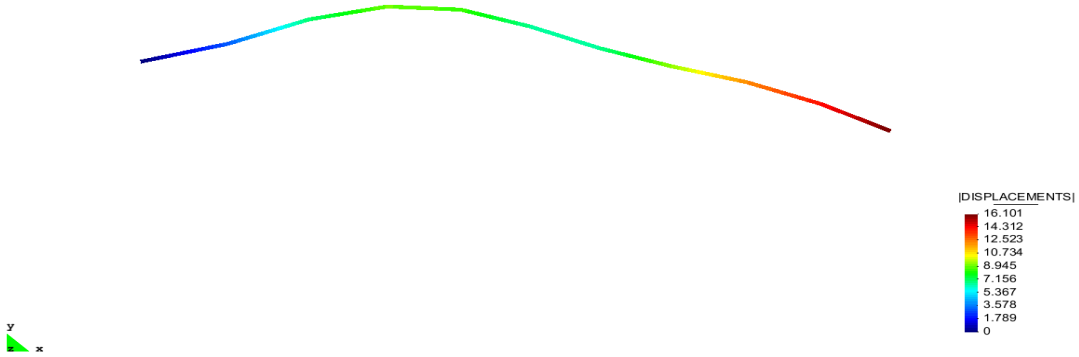

(e) Deformation of dynamic rod on 1-2 plane at time step 300

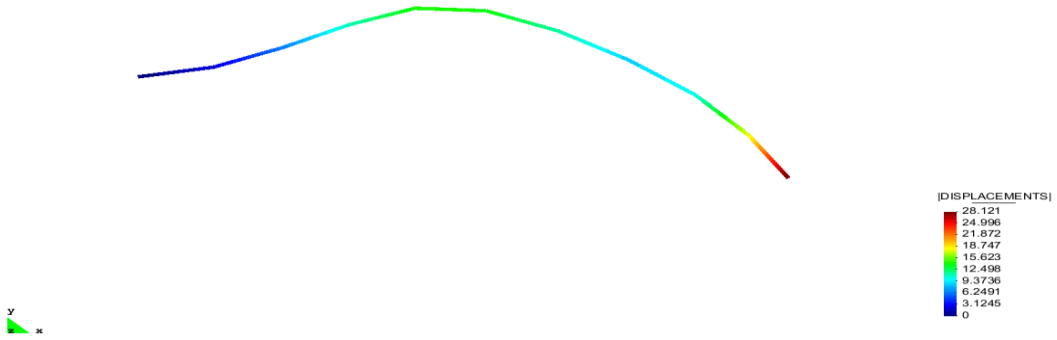

(f) Deformation of dynamic rod on 1-2 plane at time step 350

Figure 3-21: Deformation of dynamic rod on 1-2 plane

(a) Deformation of dynamic rod in isometric view at time step 100

(b) Deformation of dynamic rod in isometric view at time step 150

(c) Deformation of dynamic rod in isometric view at time step 200

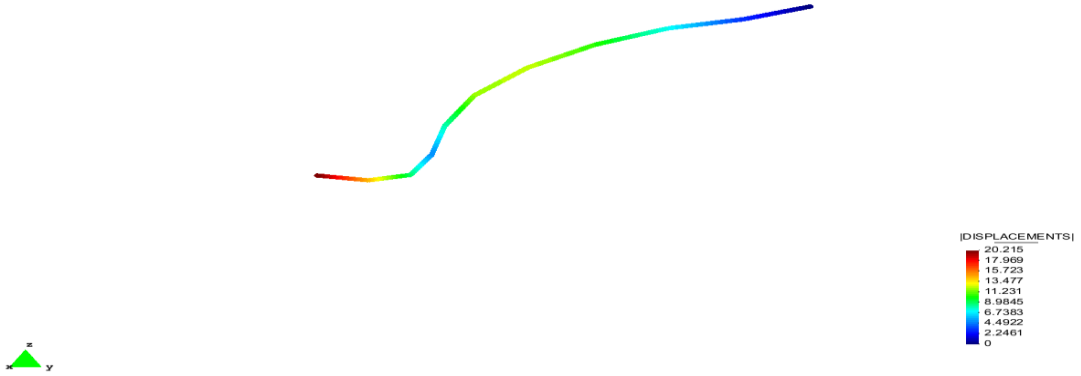

(d) Deformation of dynamic rod in isometric view at time step 250

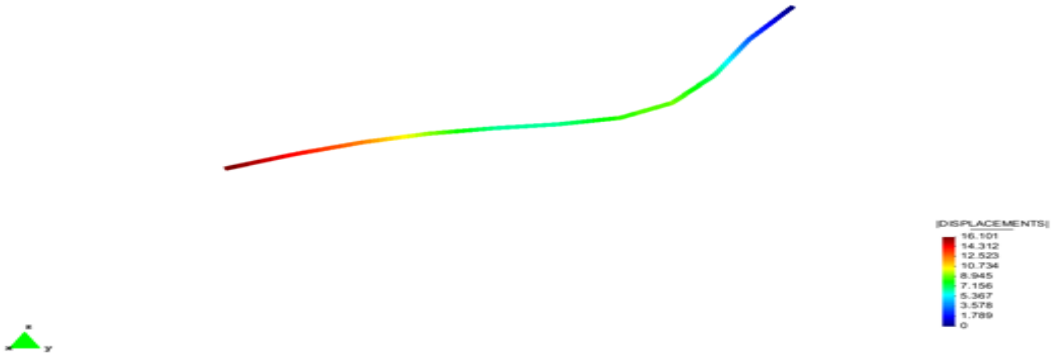

(e) Deformation of dynamic rod in isometric view at time step 300

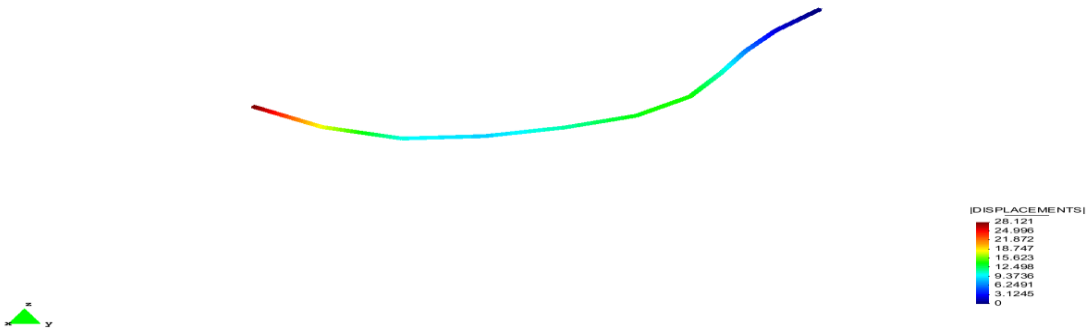

(f) Deformation of dynamic rod in isometric view at time step 350

Figure 3-22: Deformation of dynamic rod in isometric view

With a total of 350 time steps, the configurations of the rod deformation in-plane, i.e. on the 1-3 plane, are shown in Figure 3.20 at time step 100, 150, 200, 250, 300 and 350. Figure 3.21 shows the deformation of the rod in 1-2 plane at time steps 100, 150, 200, 250, 300 and 350. And Figure 3.22 gives an isometric view of the configurations over the same time steps.

The simulation reflects whipping a soft rope, with force or moment applied in-plane and out-of-plane. The external loading increases and decreases with time. Figure 3.22 demonstrates a three-dimensional image of the process, which altogether supports the idea that a 1-D atomic chain model deforming in 3-D space could be considered for simulating CNTs under vibration or under similar dynamic loading cases.

3.4.4 Simulation of atomic chain in torsion

We consider an atomic chain with two hinged ends, with the assumption that both ends allow rotations, and one end allows horizontal movement. As the model of the atomic chain is rather flexible, we can imagine it as a model of a soft thread. First, we add a torsion loading at the end of the thread, as shown in Figure 3.23. Keeping the deformation after torsion, we apply an instant small disturbance on the thread to give it sideways deformation, which is only for the help of the simulation, because in an ideal model, the atomic chain will not buckle under pure compression. After the disturbance, we push one end of the thread to make it bend. The whole loading process is shown in Figure 3.23 and Figure 3.24.

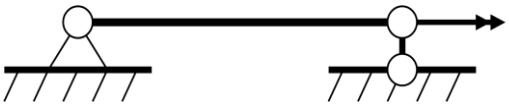

Figure 3-23: Atomic chain model in torsion

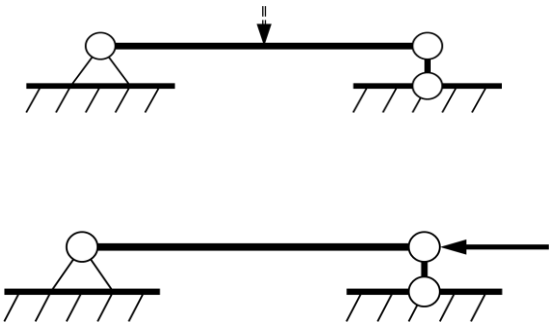

Figure 3-24: A small disturbance and force to buckle

The simulation result shows, after the instant disturbance, that the thread tends to vibrate about a random weak spot with small amplitude, which is shown in Figure 3.25. Because it is a one-dimensional model, we cannot see the torsion deformation of the thread in the figure.

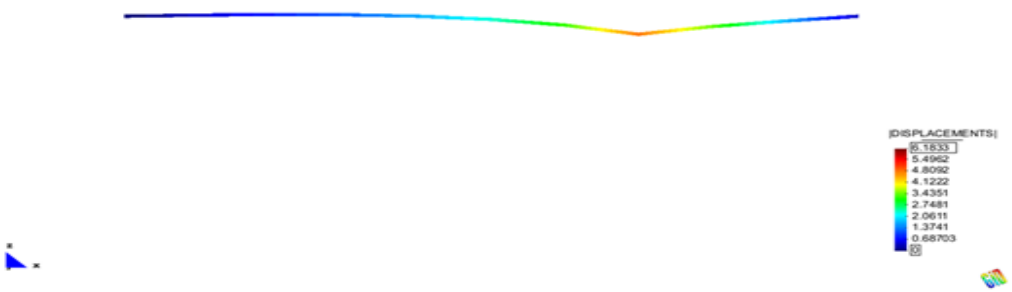

Figure 3-25: Deformation of atomic chain after small disturbance

Figure 3.26 demonstrates the simulation of thread coiling after the disturbance, with the pushing load applied. In reality, if you take a thread, roll it at the ends,

then the two ends bend together, it will result in a DNA-like shape, rotating and twisting, similar to the deformation shown in Figure 3.26, which is the original inspiration of this simulation.

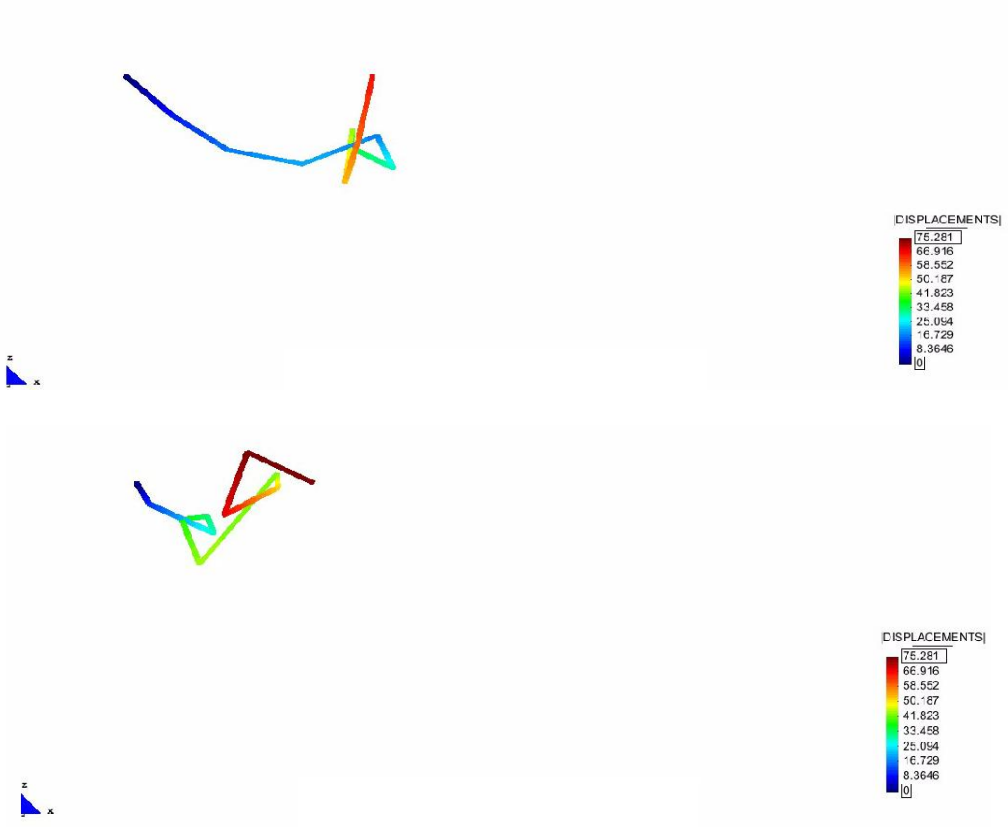

Figure 3-26: Simulation of atomic chain coiling up

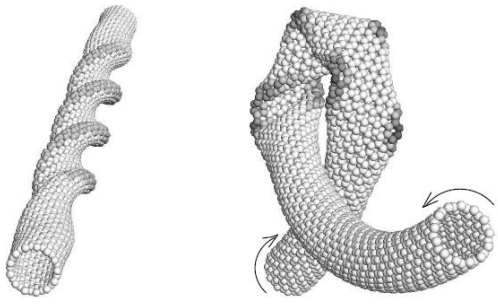

Figure 3-27: Atomistic simulation of torsion of CNT (*Yakobson et al. 1996*)

Yakobson et al. (*1996*) used atomistic methods to simulate the torsion of CNTs, the deformation pattern changed from a straight spiral to sideways buckling and then coils into a loop, as shown in Figure 3.27. The abrupt change is large and non-linear but reversible, that is, CNTs have 'shape memory'. This very feature is captured in the simulation of the atomic chain. It can be realized that the atomic chain model and CNTs have a lot of elastic properties in common. They are flexible in bending, and they can stand extremely large deformations while the change is reversible. Although the numerical values of the results obtained from atomic chain model may not match those of CNTs, they can still provide qualitative information related to simulations of CNTs.

3.4.5 Atomic ring: simulation of cross section of CNT under bending

Kutana and Giapis (*2006*) presented bending deformations of CNTs by the use of molecular dynamics simulations. Figure 3.28 was given as transient deformations of the cross section of SWCNTs under bending. *Vodenitcharova and Zhang* (*2004*) also simulated an atomic ring, cross sectional view of deformed CNT under bending is shown in Figure 3.29. Motivated by these results, an atomic chain, in this case, an atomic ring is simulated as a cross section of a CNT under bending. When CNT is in bending, the bottom of the tube is under tension and the top of the tube is under compression. Thus, it is simulated as a radius-inward pressure at the top of the ring and a radius-outwards stretch at the bottom of the ring, as shown in Figure 3.30. Figure 3.31 depicts the deformed atomic ring as simulated using the present approach.

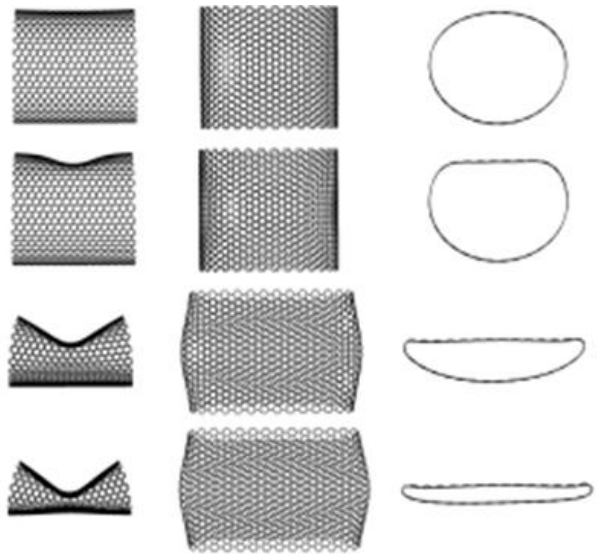

Figure 3-28: Transient deformations of the cross section of SWCNTs under bending (*Kutana and Giapis, 2006*)

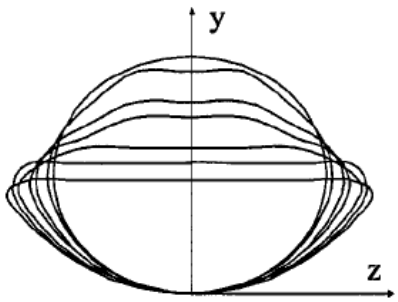

Figure 3-29: Deformed atomic rings in simulating cross section of CNT under bending (*Vodenitcharova and Zhang, 2004*)

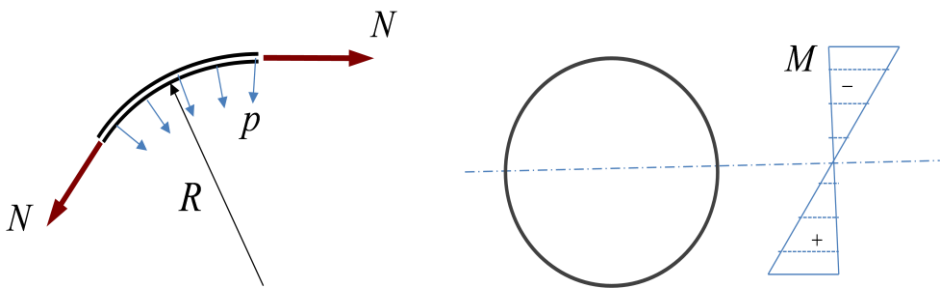

Figure 3-30: Sketch of the strategy of atomic ring in simulation of CNT in bending

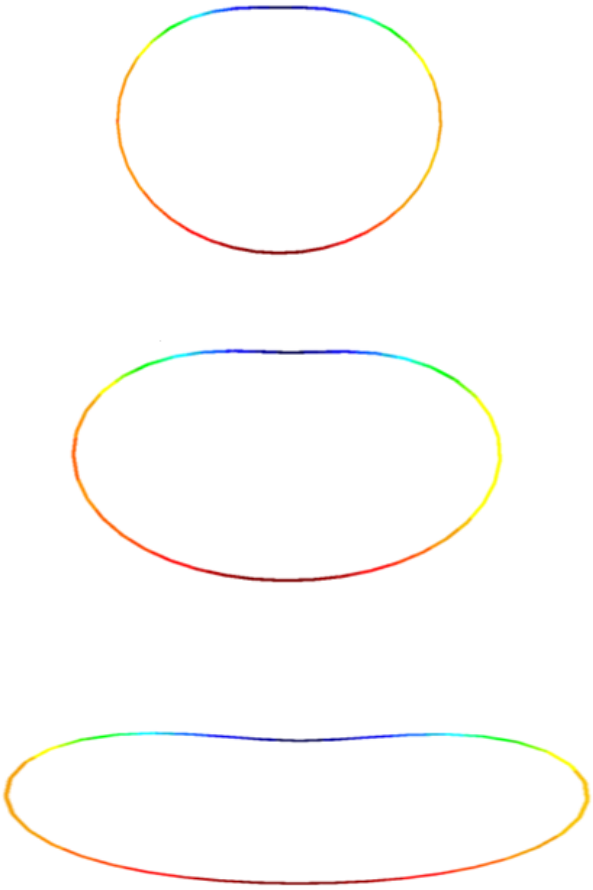

Figure 3-31: Deformed atomic ring in simulating cross section of SWCNT under bending

The real physical meaning of an atomic chain is still under development. All the results given in the sections above are only qualitative results, which, however, capture the elastic behaviour of CNTs in qualitative terms. Although the results do not provide quantitative properties of CNTs, atomic chain models do establish a good preparation for the next step of modelling SWCNTs as Cosserat surface, where the quantitative descriptions for elastic properties of SWCNTs will be demonstrated in Chapter 4.

Chapter 4

Single-walled Carbon Nanotube: Cosserat Surface

This chapter applies the Cosserat surface theory in modelling and simulating carbon nanotubes' (CNTs) behaviours. CNTs are modelled as unrolled two-dimensional graphite sheets or as cylindrical shell models. Potential forms are applied as described in Section 2.4, where, in this chapter, the in-plane and out-of-plane contributions are considered for the calculation of stress fields and moment fields. The mechanical properties of CNTs, such as Young's modulus and Poisson ratio are predicted as tension and bending models, and the deformations of CNTs under bending, compression and torsion loadings are simulated in Section 4.2 to Section 4.6.

4.1 Carbon nanotube modelling

In two dimensions the potential for CNTs is in the form of

$$V_{REBO} = \sum_{i} \sum_{j=i+1} \left[V_R(r_{IJ}) - \bar{b}_{IJ} V_A(r_{IJ}) \right] \tag{4.1}$$

with

$$V_R(r) = f_c(r) \left(1 + \frac{Q}{r}\right) A \exp(-\alpha r) \tag{4.2}$$

$$V_A(r) = f_c(r) \sum_{n=1}^{3} B_n e^{-\beta_n r} \tag{4.3}$$

and

$$f_c(r) = \begin{cases} 1 & r < R_1 \\ \left\{1 + \cos\left[\dfrac{\pi(r - R_1)}{R_2 - R_1}\right]\right\}/2 & R_1 < r < R_2 \\ 0 & r > R_2 \end{cases} \tag{4.4}$$

while

$$\bar{b}_{IJ} = \frac{1}{2}\left(b_{IJ}^{\sigma-\pi} + b_{JI}^{\sigma-\pi}\right) \tag{4.5}$$

where

$$b_{IJ}^{\sigma-\pi} = \left[1 + \sum_{K(\neq I,J)} f_{cIK}(r_{IK}) G\left(\cos\theta_{IJK}\right)\right]^{-1/2} \tag{4.6}$$

$$G\left(\cos\theta_{IJK}\right) = \sum_{n=0}^{5} a_n \left(\cos\theta_{IJK}\right)^n \tag{4.7}$$

where all the quantities are already defined in Section 2.4. The potential is expressed as a function of the three bond lengths and the three bond angles. If an atom *A* and its neighbouring atoms are as shown in Figure 4.1, the potential can be expressed as $V = V(r_{AB}, r_{AC}, r_{AD}, \theta_{BAC}, \theta_{BAD}, \theta_{CAD})$, where r_{AB}, r_{AC} and r_{AD} are the deformed bond lengths of *A*-*B*, *A*-*C* and *A*-*D* bonds, and θ_{BAC}, θ_{BAD} and θ_{CAD}

are the deformed bond angles between *A*-*B* and *A*-*C*, between *A*-*B* and *A*-*D* and between *A*-*C* and *A*-*D* bonds.

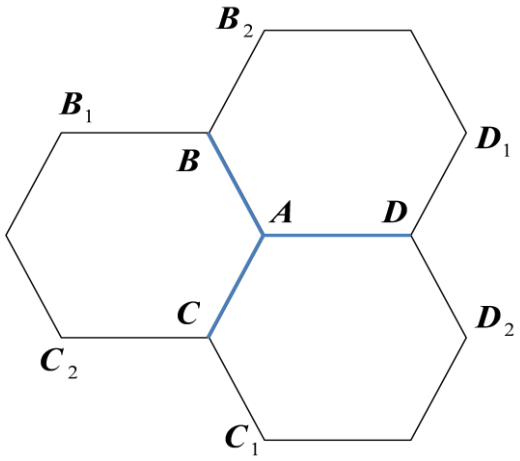

Figure 4-1: Atom A and its first and second nearest neighbours

One may notice, there are also second nearest neighbouring atoms(B_1, B_2, C_1, C_2, D_1, D_2) involved in the potential form. To avoid the lengthy expansion of the total energy form, here only the formula for atom *A* and its neighbours is derived. The same method is applied to atom *B*, *C* and *D*, which gives the final total potential form in terms of $\boldsymbol{U}$ and $\boldsymbol{\mathcal{K}}$ (See Appendix C).

We recall the definition of the curvature tensor

$$\boldsymbol{\mathcal{K}} = \begin{bmatrix} \mathcal{K}_{11} & \mathcal{K}_{12} & \mathcal{K}_{13} \\ \mathcal{K}_{21} & \mathcal{K}_{22} & \mathcal{K}_{23} \\ 0 & 0 & 0 \end{bmatrix} \tag{4.8}$$

and the strain tensor

$$\boldsymbol{U} = \begin{bmatrix} U_{11} & U_{12} & U_{13} \\ U_{21} & U_{22} & U_{23} \\ 0 & 0 & 1 \end{bmatrix} \tag{4.9}$$

The components U_{13}, U_{23} , $\mathcal{K}_{13}$ and $\mathcal{K}_{23}$ contribute to the extra terms for shear energy and spin energy in the total energy formulation. Two principal directions

$\boldsymbol{V}_{\mathrm{I}}$ and $\boldsymbol{V}_{\mathrm{II}}$ can be found on the reference plane. Let $\boldsymbol{A}_1$ and $\boldsymbol{A}_2$ be the components of the undeformed vector $\boldsymbol{A}$ along $\boldsymbol{V}_{\mathrm{I}}$ and $\boldsymbol{V}_{\mathrm{II}}$directions, which then rotate to $\boldsymbol{A}_1'$ and $\boldsymbol{A}_2'$ by the rotation tensors $\boldsymbol{R}_1$ and $\boldsymbol{R}_2$, as shown in Figure 4.2, which define the micro-rotation on the reference plane.

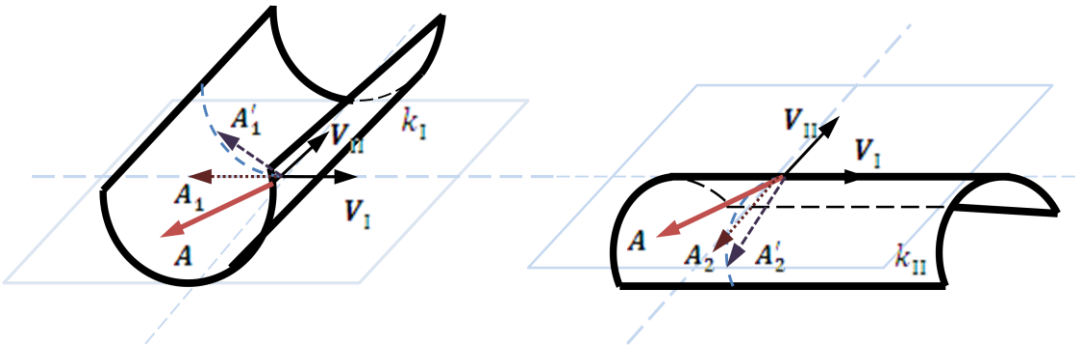

Figure 4-2: Micro-rotation on the reference plane

The principal curvatures k_{I} and k_{II} can be obtained from the equation

$$\det\begin{bmatrix}\mathcal{K}_{11}-k & \mathcal{K}_{12}\\ \mathcal{K}_{21} & \mathcal{K}_{22}-k\end{bmatrix}=0 \tag{4.10}$$

Then, we have

$$k_{\mathrm{I,II}}=\frac{(\mathcal{K}_{11}+\mathcal{K}_{22})\pm\sqrt{(\mathcal{K}_{11}+\mathcal{K}_{22})^2-4(\mathcal{K}_{11}\mathcal{K}_{22}-\mathcal{K}_{12}\mathcal{K}_{21})}}{2} \tag{4.11}$$

The principal directions can be obtained from

$$\begin{bmatrix}\mathcal{K}_{11}-k_{\mathrm{I}} & \mathcal{K}_{12}\\ \mathcal{K}_{21} & \mathcal{K}_{22}-k_{\mathrm{I}}\end{bmatrix}\begin{Bmatrix}V_{1,\mathrm{I}}\\ V_{2,\mathrm{I}}\end{Bmatrix}=\begin{Bmatrix}0\\0\end{Bmatrix} \tag{4.12}$$

They are normalized by

$$V_{1,\mathrm{I}}{}^2+V_{2,\mathrm{I}}{}^2=1 \tag{4.13}$$

resulting in

$$V_{1,\mathrm{I}} = \frac{1}{\sqrt{1+\left(\frac{\mathcal{K}_{11}-k_{\mathrm{I}}}{\mathcal{K}_{12}}\right)^2}}$$

$$V_{2,\mathrm{I}} = \frac{1}{\sqrt{1+\left(\frac{\mathcal{K}_{22}-k_{\mathrm{I}}}{\mathcal{K}_{21}}\right)^2}} \tag{4.14}$$

Thus, the principal directions $\mathrm{V_I}$ and and $\mathrm{V_{II}}$ are obtained as

$$\boldsymbol{V}_{\mathrm{I}} = \begin{Bmatrix} V_{1,\mathrm{I}} \\ V_{2,\mathrm{I}} \end{Bmatrix} = \begin{Bmatrix} \frac{1}{\sqrt{1+\left(\frac{\mathcal{K}_{11}-k_{\mathrm{I}}}{\mathcal{K}_{12}}\right)^2}} \\ \frac{1}{\sqrt{1+\left(\frac{\mathcal{K}_{22}-k_{\mathrm{I}}}{\mathcal{K}_{21}}\right)^2}} \end{Bmatrix}$$

$$\boldsymbol{V}_{\mathrm{II}} = \begin{Bmatrix} V_{1,\mathrm{II}} \\ V_{2,\mathrm{II}} \end{Bmatrix} = \begin{Bmatrix} \frac{1}{\sqrt{1+\left(\frac{\mathcal{K}_{11}-k_{\mathrm{II}}}{\mathcal{K}_{12}}\right)^2}} \\ \frac{1}{\sqrt{1+\left(\frac{\mathcal{K}_{22}-k_{\mathrm{II}}}{\mathcal{K}_{21}}\right)^2}} \end{Bmatrix} \tag{4.15}$$

The lattice vector $\boldsymbol{A'}$ is the vector that the undeformed lattice vector $\boldsymbol{A}$ rotates to after applying the micro-rotation tensor, which is given by

$$\boldsymbol{A'} = \boldsymbol{A}_1' + \boldsymbol{A}_2' = \boldsymbol{R}_1\boldsymbol{A}_1 + \boldsymbol{R}_2\boldsymbol{A}_2 \tag{4.16}$$

where

$$\boldsymbol{A}_1 = (\boldsymbol{V}_{\mathrm{I}} \cdot \boldsymbol{A})\boldsymbol{V}_{\mathrm{I}}$$

$$\boldsymbol{A}_2 = (\boldsymbol{V}_{\mathrm{II}} \cdot \boldsymbol{A})\boldsymbol{V}_{\mathrm{II}} \tag{4.17}$$

Finally

$$\boldsymbol{A'} = \boldsymbol{R}_1(\boldsymbol{V}_{\mathrm{I}} \cdot \boldsymbol{A})\boldsymbol{V}_{\mathrm{I}} + \boldsymbol{R}_2(\boldsymbol{V}_{\mathrm{II}} \cdot \boldsymbol{A})\boldsymbol{V}_{\mathrm{II}} \tag{4.18}$$

The final deformed lattice vector $\boldsymbol{a}'$ is obtained after rotating by $\boldsymbol{R}$ then after stretching by $\boldsymbol{U}$, which is expressed as

$$\boldsymbol{a}' = \boldsymbol{U}\boldsymbol{A}' = \boldsymbol{U}\boldsymbol{R}_1(\boldsymbol{V}_{\mathrm{I}} \cdot \boldsymbol{A})\boldsymbol{V}_{\mathrm{I}} + \boldsymbol{U}\boldsymbol{R}_2(\boldsymbol{V}_{\mathrm{II}} \cdot \boldsymbol{A})\boldsymbol{V}_{\mathrm{II}} \tag{4.19}$$

The vector length after stretch is

$$a = \sqrt{\boldsymbol{U}^T\boldsymbol{U}}A' = \sqrt{\boldsymbol{U}^T\boldsymbol{U}}A \tag{4.20}$$

The strain energy density is the total potential of the atom over the area

$$W_0(\boldsymbol{U}, \boldsymbol{\mathcal{K}}, \boldsymbol{\xi}) = \frac{V(r_{AB}) + V(r_{AC}) + V(r_{AD})}{S_0} \tag{4.21}$$

where $S_0 = \left(3\sqrt{3}/2\right)A_0^2$, A_0 is the undeformed bond length, and

$$\begin{aligned} V(r_{AB}) &= V(r_{AB}, r_{AC}, r_{AD}, \theta_{BAC}, \theta_{BAD}) \\ V(r_{AC}) &= V(r_{AC}, r_{AB}, r_{AD}, \theta_{BAC}, \theta_{CAD}) \\ V(r_{AD}) &= V(r_{AD}, r_{AB}, r_{AC}, \theta_{BAD}, \theta_{CAD}) \end{aligned} \tag{4.22}$$

Considering the shift vector

$$\begin{aligned} \boldsymbol{r}_{AB} &= \boldsymbol{F}(\boldsymbol{r}_{AB}^0 + \boldsymbol{\eta}) \\ \boldsymbol{r}_{AC} &= \boldsymbol{F}(\boldsymbol{r}_{AC}^0 + \boldsymbol{\eta}) \\ \boldsymbol{r}_{AD} &= \boldsymbol{F}(\boldsymbol{r}_{AD}^0 + \boldsymbol{\eta}) \end{aligned} \tag{4.23}$$

Since the length doesn't change during the rotation, the deformed bond length only depends on the strain tensor $\boldsymbol{U}$

$$\begin{aligned} r_{AB}(\boldsymbol{U}, \boldsymbol{\eta}) &= \sqrt{(\boldsymbol{r}_{AB}^0 + \boldsymbol{\eta}) \cdot \boldsymbol{U}^T\boldsymbol{U} \cdot (\boldsymbol{r}_{AB}^0 + \boldsymbol{\eta})} \\ r_{AC}(\boldsymbol{U}, \boldsymbol{\eta}) &= \sqrt{(\boldsymbol{r}_{AC}^0 + \boldsymbol{\eta}) \cdot \boldsymbol{U}^T\boldsymbol{U} \cdot (\boldsymbol{r}_{AC}^0 + \boldsymbol{\eta})} \\ r_{AD}(\boldsymbol{U}, \boldsymbol{\eta}) &= \sqrt{(\boldsymbol{r}_{AD}^0 + \boldsymbol{\eta}) \cdot \boldsymbol{U}^T\boldsymbol{U} \cdot (\boldsymbol{r}_{AD}^0 + \boldsymbol{\eta})} \end{aligned} \tag{4.24}$$

where $\boldsymbol{r}_{AB}^0$, $\boldsymbol{r}_{AC}^0$ and $\boldsymbol{r}_{AD}^0$ are the undeformed bond vectors between *A*-*B*, *A*-*C* and *A*-*D* atoms.

On the other hand, the bond angles are related to the curvature tensor $\boldsymbol{\mathcal{K}}$

$$\boldsymbol{r}_{AB} = \boldsymbol{U}\boldsymbol{R}_1(\boldsymbol{V}_{\mathrm{I}} \cdot (\boldsymbol{r}_{AB}^0 + \boldsymbol{\eta}))\boldsymbol{V}_{\mathrm{I}} + \boldsymbol{U}\boldsymbol{R}_2(\boldsymbol{V}_{\mathrm{II}} \cdot (\boldsymbol{r}_{AB}^0 + \boldsymbol{\eta}))\boldsymbol{V}_{\mathrm{II}}$$

$$\boldsymbol{r}_{AC} = \boldsymbol{U}\boldsymbol{R}_1(\boldsymbol{V}_{\mathrm{I}} \cdot (\boldsymbol{r}_{AC}^0 + \boldsymbol{\eta}))\boldsymbol{V}_{\mathrm{I}} + \boldsymbol{U}\boldsymbol{R}_2(\boldsymbol{V}_{\mathrm{II}} \cdot (\boldsymbol{r}_{AC}^0 + \boldsymbol{\eta}))\boldsymbol{V}_{\mathrm{II}}$$

The bond angle between *A*-*B* and *A*-*C* bond can be obtained from

$$\theta_{BAC} = \arccos\frac{\boldsymbol{r}_{AB} \cdot \boldsymbol{r}_{AC}}{r_{AB}r_{AC}}$$

$$= \arccos\frac{(\boldsymbol{R}_1(\boldsymbol{V}_{\mathrm{I}} \cdot (\boldsymbol{r}_{AB}^0 + \boldsymbol{\eta}))\boldsymbol{V}_{\mathrm{I}} + \boldsymbol{R}_2(\boldsymbol{V}_{\mathrm{II}} \cdot (\boldsymbol{r}_{AB}^0 + \boldsymbol{\eta}))\boldsymbol{V}_{\mathrm{II}}) \cdot \boldsymbol{U}^T\boldsymbol{U} \cdot (\boldsymbol{R}_1(\boldsymbol{V}_{\mathrm{I}} \cdot (\boldsymbol{r}_{AC}^0 + \boldsymbol{\eta}))\boldsymbol{V}_{\mathrm{I}} + \boldsymbol{R}_2(\boldsymbol{V}_{\mathrm{II}} \cdot (\boldsymbol{r}_{AC}^0 + \boldsymbol{\eta}))\boldsymbol{V}_{\mathrm{II}})}{\sqrt{(\boldsymbol{r}_{AB}^0 + \boldsymbol{\eta}) \cdot \boldsymbol{U}^T\boldsymbol{U} \cdot (\boldsymbol{r}_{AB}^0 + \boldsymbol{\eta})}\sqrt{(\boldsymbol{r}_{AC}^0 + \boldsymbol{\eta}) \cdot \boldsymbol{U}^T\boldsymbol{U} \cdot (\boldsymbol{r}_{AC}^0 + \boldsymbol{\eta})}}$$

Similarly, we can get the other two bond angles from

$$\boldsymbol{r}_{AD} = \boldsymbol{U}\boldsymbol{R}_1(\boldsymbol{V}_{\mathrm{I}} \cdot (\boldsymbol{r}_{AD}^0 + \boldsymbol{\eta}))\boldsymbol{V}_{\mathrm{I}} + \boldsymbol{U}\boldsymbol{R}_2(\boldsymbol{V}_{\mathrm{II}} \cdot (\boldsymbol{r}_{AD}^0 + \boldsymbol{\eta}))\boldsymbol{V}_{\mathrm{II}}$$

$$\theta_{BAD} = \arccos\frac{\boldsymbol{r}_{AB} \cdot \boldsymbol{r}_{AD}}{r_{AB}r_{AD}}$$

$$\theta_{CAD} = \arccos\frac{\boldsymbol{r}_{AC} \cdot \boldsymbol{r}_{AD}}{r_{AC}r_{AD}} \tag{4.25}$$

Define the bond lengths r_{AB}, r_{AC}, r_{AD} as a_i (*i*=1,2,3) and the bond angles θ_{BAC}, θ_{BAD}, θ_{CAD} as θ_i (*i*=1,2,3), then the potential can be expressed in terms of $\boldsymbol{U}, \boldsymbol{\mathcal{K}}$ and $\boldsymbol{\eta}$. For simplicity, we write W instead of W_0 to present the strain energy density for the rest of this section. Then the internal degree of freedom $\boldsymbol{\eta}$ can be determined by minimizing the strain energy density $W(\boldsymbol{U}, \boldsymbol{\mathcal{K}}; \boldsymbol{\eta})$ with respect to $\boldsymbol{\eta}$

$$\frac{\partial W}{\partial \boldsymbol{\eta}} = \boldsymbol{0} \;\Rightarrow\; \boldsymbol{\eta} = \boldsymbol{\eta}(\boldsymbol{U}, \boldsymbol{\mathcal{K}}) \tag{4.26}$$

$$\frac{\partial W}{\partial \boldsymbol{\eta}} = \sum_{i=1}^{3}\left(\frac{\partial W}{\partial a_i}\frac{\partial a_i}{\partial \boldsymbol{\eta}} + \frac{\partial W}{\partial \theta_i}\frac{\partial \theta_i}{\partial \boldsymbol{\eta}}\right) \tag{4.27}$$

Strain energy density W again can be written as a function of the strain tensor $\boldsymbol{U}$ and the curvature tensor $\boldsymbol{\mathcal{K}}$

$$W = W\big(\boldsymbol{U}, \boldsymbol{\mathcal{K}}; \boldsymbol{\eta}(\boldsymbol{U}, \boldsymbol{\mathcal{K}})\big) \tag{4.28}$$

The force tensor can be obtained from

$$\boldsymbol{S} = \frac{dW}{d\boldsymbol{U}} = \frac{\partial W}{\partial \boldsymbol{U}} + \frac{\partial W}{\partial \boldsymbol{\eta}}\frac{\partial \boldsymbol{\eta}}{\partial \boldsymbol{U}} = \frac{\partial W}{\partial \boldsymbol{U}} \tag{4.29}$$

where

$$\frac{\partial W}{\partial U_{ab}} = \sum_{i=1}^{3}\left(\frac{\partial W}{\partial a_i}\frac{\partial a_i}{\partial U_{ab}} + \frac{\partial W}{\partial \theta_i}\frac{\partial \theta_i}{\partial U_{ab}}\right) \tag{4.30}$$

The couple tensor can be calculated from

$$\boldsymbol{T} = \frac{dW}{d\boldsymbol{\mathcal{K}}} = \frac{\partial W}{\partial \boldsymbol{\mathcal{K}}} + \frac{\partial W}{\partial \boldsymbol{\eta}}\frac{\partial \boldsymbol{\eta}}{\partial \boldsymbol{\mathcal{K}}} = \frac{\partial W}{\partial \boldsymbol{\mathcal{K}}} \tag{4.31}$$

where

$$\frac{\partial W}{\partial \mathcal{K}_{ab}} = \sum_{i=1}^{3}\left(\frac{\partial W}{\partial a_i}\frac{\partial a_i}{\partial \mathcal{K}_{ab}} + \frac{\partial W}{\partial \theta_i}\frac{\partial \theta_i}{\partial \mathcal{K}_{ab}}\right) = \sum_{i=1}^{3}\frac{\partial W}{\partial \theta_i}\frac{\partial \theta_i}{\partial \mathcal{K}_{ab}} \tag{4.32}$$

The tensor-like stretch modulus reads

$$\boldsymbol{n} = \frac{d\boldsymbol{S}}{d\boldsymbol{U}} = \frac{\partial \boldsymbol{S}}{\partial \boldsymbol{U}} + \frac{\partial \boldsymbol{S}}{\partial \boldsymbol{\eta}} \cdot \frac{\partial \boldsymbol{\eta}}{\partial \boldsymbol{U}} = \frac{\partial^2 W}{\partial \boldsymbol{U}\partial \boldsymbol{U}} + \frac{\partial^2 W}{\partial \boldsymbol{U}\partial \boldsymbol{\eta}} \cdot \frac{\partial \boldsymbol{\eta}}{\partial \boldsymbol{U}} \tag{4.33}$$

with the relation of

$$\frac{d(\partial W/\partial \boldsymbol{\eta})}{d\boldsymbol{U}} = \boldsymbol{0}$$

one can derive

$$\frac{\partial(\partial W/\partial \boldsymbol{\eta})}{\partial \boldsymbol{U}} + \frac{\partial(\partial W/\partial \boldsymbol{\eta})}{\partial \boldsymbol{\eta}} \cdot \frac{\partial \boldsymbol{\eta}}{\partial \boldsymbol{U}} = \boldsymbol{0}$$

$$\frac{\partial \boldsymbol{\eta}}{\partial \boldsymbol{U}} = -\left(\frac{\partial^2 W}{\partial \boldsymbol{\eta}\partial \boldsymbol{\eta}}\right)^{-1} \cdot \frac{\partial^2 W}{\partial \boldsymbol{\eta}\partial \boldsymbol{U}}$$

Then $\boldsymbol{n}$ is obtained as

$$\boldsymbol{n} = \frac{\partial^2 W}{\partial \boldsymbol{U}\partial \boldsymbol{U}} - \frac{\partial^2 W}{\partial \boldsymbol{U}\partial \boldsymbol{\eta}} \cdot \left(\frac{\partial^2 W}{\partial \boldsymbol{\eta}\partial \boldsymbol{\eta}}\right)^{-1} \cdot \frac{\partial^2 W}{\partial \boldsymbol{\eta}\partial \boldsymbol{U}} \tag{4.34}$$

where

$$\frac{\partial^2 W}{\partial U_{ab}\partial U_{kl}} = \sum_{i=1}^{3}\sum_{j=1}^{3}\left(\frac{\partial^2 W}{\partial a_i \partial a_j}\frac{\partial a_j}{\partial U_{kl}}\frac{\partial a_i}{\partial U_{ab}} + \frac{\partial^2 W}{\partial a_i \partial \theta_j}\frac{\partial \theta_j}{\partial U_{kl}}\frac{\partial a_i}{\partial U_{ab}} + \frac{\partial W}{\partial a_i}\frac{\partial^2 a_i}{\partial U_{ab}\partial U_{kl}}\right.$$
$$\left. + \frac{\partial^2 W}{\partial \theta_i \partial a_j}\frac{\partial a_j}{\partial U_{kl}}\frac{\partial \theta_i}{\partial U_{ab}} + \frac{\partial^2 W}{\partial \theta_i \partial \theta_j}\frac{\partial \theta_j}{\partial U_{kl}}\frac{\partial \theta_i}{\partial U_{ab}} + \frac{\partial W}{\partial \theta_i}\frac{\partial^2 \theta_i}{\partial U_{ab}\partial U_{kl}}\right)$$

$$\frac{\partial^2 W}{\partial U_{ab}\partial \eta_p} = \sum_{i=1}^{3}\sum_{j=1}^{3}\left(\frac{\partial^2 W}{\partial a_i \partial a_j}\frac{\partial a_j}{\partial \eta_p}\frac{\partial a_i}{\partial U_{ab}} + \frac{\partial^2 W}{\partial a_i \partial \theta_j}\frac{\partial \theta_j}{\partial \eta_p}\frac{\partial a_i}{\partial U_{ab}} + \frac{\partial W}{\partial a_i}\frac{\partial^2 a_i}{\partial U_{ab}\partial \eta_p}\right.$$
$$\left. + \frac{\partial^2 W}{\partial \theta_i \partial a_j}\frac{\partial a_j}{\partial \eta_p}\frac{\partial \theta_i}{\partial U_{ab}} + \frac{\partial^2 W}{\partial \theta_i \partial \theta_j}\frac{\partial \theta_j}{\partial \eta_p}\frac{\partial \theta_i}{\partial U_{ab}} + \frac{\partial W}{\partial \theta_i}\frac{\partial^2 \theta_i}{\partial U_{ab}\partial \eta_p}\right)$$

$$\frac{\partial^2 W}{\partial \eta_p \partial \eta_q} = \sum_{i=1}^{3}\sum_{j=1}^{3}\left(\frac{\partial^2 W}{\partial a_i \partial a_j}\frac{\partial a_j}{\partial \eta_q}\frac{\partial a_i}{\partial \eta_p} + \frac{\partial^2 W}{\partial a_i \partial \theta_j}\frac{\partial \theta_j}{\partial \eta_q}\frac{\partial a_i}{\partial \eta_p} + \frac{\partial W}{\partial a_i}\frac{\partial^2 a_i}{\partial \eta_p \partial \eta_q}\right.$$
$$\left. + \frac{\partial^2 W}{\partial \theta_i \partial a_j}\frac{\partial a_j}{\partial \eta_q}\frac{\partial \theta_i}{\partial \eta_p} + \frac{\partial^2 W}{\partial \theta_i \partial \theta_j}\frac{\partial \theta_j}{\partial \eta_q}\frac{\partial \theta_i}{\partial \eta_p} + \frac{\partial W}{\partial \theta_i}\frac{\partial^2 \theta_i}{\partial \eta_p \partial \eta_q}\right)$$

$$\frac{\partial^2 W}{\partial \eta_q \partial U_{kl}} = \sum_{i=1}^{3}\sum_{j=1}^{3}\left(\frac{\partial^2 W}{\partial a_i \partial a_j}\frac{\partial a_j}{\partial U_{kl}}\frac{\partial a_i}{\partial \eta_q} + \frac{\partial^2 W}{\partial a_i \partial \theta_j}\frac{\partial \theta_j}{\partial U_{kl}}\frac{\partial a_i}{\partial \eta_q} + \frac{\partial W}{\partial a_i}\frac{\partial^2 a_i}{\partial \eta_q \partial U_{kl}}\right.$$
$$\left. + \frac{\partial^2 W}{\partial \theta_i \partial a_j}\frac{\partial a_j}{\partial U_{kl}}\frac{\partial \theta_i}{\partial \eta_q} + \frac{\partial^2 W}{\partial \theta_i \partial \theta_j}\frac{\partial \theta_j}{\partial U_{kl}}\frac{\partial \theta_i}{\partial \eta_q} + \frac{\partial W}{\partial \theta_i}\frac{\partial^2 \theta_i}{\partial \eta_q \partial U_{kl}}\right)$$

The tensor-like bending modulus reads

$$\boldsymbol{m} = \frac{d\boldsymbol{T}}{d\boldsymbol{\mathcal{K}}} = \frac{\partial \boldsymbol{T}}{\partial \boldsymbol{\mathcal{K}}} + \frac{\partial \boldsymbol{T}}{\partial \boldsymbol{\eta}} \cdot \frac{\partial \boldsymbol{\eta}}{\partial \boldsymbol{\mathcal{K}}} = \frac{\partial^2 W}{\partial \boldsymbol{\mathcal{K}} \partial \boldsymbol{\mathcal{K}}} + \frac{\partial^2 W}{\partial \boldsymbol{\mathcal{K}} \partial \boldsymbol{\eta}} \cdot \frac{\partial \boldsymbol{\eta}}{\partial \boldsymbol{\mathcal{K}}} \qquad (4.35)$$

Similarly from

$$\frac{d(\partial W/\partial \boldsymbol{\eta})}{d\boldsymbol{\mathcal{K}}} = \boldsymbol{0}$$

$$\frac{\partial \boldsymbol{\eta}}{\partial \boldsymbol{\mathcal{K}}} = -\left(\frac{\partial^2 W}{\partial \boldsymbol{\eta} \partial \boldsymbol{\eta}}\right)^{-1} \cdot \frac{\partial^2 W}{\partial \boldsymbol{\eta} \partial \boldsymbol{\mathcal{K}}}$$

$$\boldsymbol{m} = \frac{\partial^2 W}{\partial \boldsymbol{\mathcal{K}} \partial \boldsymbol{\mathcal{K}}} - \frac{\partial^2 W}{\partial \boldsymbol{\mathcal{K}} \partial \boldsymbol{\eta}} \cdot \left(\frac{\partial^2 W}{\partial \boldsymbol{\eta} \partial \boldsymbol{\eta}}\right)^{-1} \cdot \frac{\partial^2 W}{\partial \boldsymbol{\eta} \partial \boldsymbol{\mathcal{K}}} \qquad (4.36)$$

where

$$\frac{\partial^2 W}{\partial \mathcal{K}_{ab}\partial \mathcal{K}_{kl}} = \sum_{i=1}^{3}\sum_{j=1}^{3}\left(\frac{\partial^2 W}{\partial a_i \partial a_j}\frac{\partial a_j}{\partial \mathcal{K}_{kl}}\frac{\partial a_i}{\partial \mathcal{K}_{ab}} + \frac{\partial^2 W}{\partial a_i \partial \theta_j}\frac{\partial \theta_j}{\partial \mathcal{K}_{kl}}\frac{\partial a_i}{\partial \mathcal{K}_{ab}}\right.$$

$$+\frac{\partial W}{\partial a_i}\frac{\partial^2 a_i}{\partial \mathcal{K}_{ab}\partial \mathcal{K}_{kl}} + \frac{\partial^2 W}{\partial \theta_i \partial a_j}\frac{\partial a_j}{\partial \mathcal{K}_{kl}}\frac{\partial \theta_i}{\partial \mathcal{K}_{ab}} + \frac{\partial^2 W}{\partial \theta_i \partial \theta_j}\frac{\partial \theta_j}{\partial \mathcal{K}_{kl}}\frac{\partial \theta_i}{\partial \mathcal{K}_{ab}}$$

$$\left.+\frac{\partial W}{\partial \theta_i}\frac{\partial^2 \theta_i}{\partial \mathcal{K}_{ab}\partial \mathcal{K}_{kl}}\right)$$

$$= \sum_{i=1}^{3}\sum_{j=1}^{3}\left(\frac{\partial^2 W}{\partial \theta_i \partial \theta_j}\frac{\partial \theta_j}{\partial \mathcal{K}_{kl}}\frac{\partial \theta_i}{\partial \mathcal{K}_{ab}} + \frac{\partial W}{\partial \theta_i}\frac{\partial^2 \theta_i}{\partial \mathcal{K}_{ab}\partial \mathcal{K}_{kl}}\right)$$

$$\frac{\partial^2 W}{\partial \mathcal{K}_{ab}\partial \eta_p} = \sum_{i=1}^{3}\sum_{j=1}^{3}\left(\frac{\partial^2 W}{\partial a_i \partial a_j}\frac{\partial a_j}{\partial \eta_p}\frac{\partial a_i}{\partial \mathcal{K}_{ab}} + \frac{\partial^2 W}{\partial a_i \partial \theta_j}\frac{\partial \theta_j}{\partial \eta_p}\frac{\partial a_i}{\partial \mathcal{K}_{ab}} + \frac{\partial W}{\partial a_i}\frac{\partial^2 a_i}{\partial \mathcal{K}_{ab}\partial \eta_p}\right.$$

$$\left.+\frac{\partial^2 W}{\partial \theta_i \partial a_j}\frac{\partial a_j}{\partial \eta_p}\frac{\partial \theta_i}{\partial \mathcal{K}_{ab}} + \frac{\partial^2 W}{\partial \theta_i \partial \theta_j}\frac{\partial \theta_j}{\partial \eta_p}\frac{\partial \theta_i}{\partial \mathcal{K}_{ab}} + \frac{\partial W}{\partial \theta_i}\frac{\partial^2 \theta_i}{\partial \mathcal{K}_{ab}\partial \eta_p}\right)$$

$$= \sum_{i=1}^{3}\sum_{j=1}^{3}\left(\frac{\partial^2 W}{\partial \theta_i \partial a_j}\frac{\partial a_j}{\partial \eta_p}\frac{\partial \theta_i}{\partial \mathcal{K}_{ab}} + \frac{\partial^2 W}{\partial \theta_i \partial \theta_j}\frac{\partial \theta_j}{\partial \eta_p}\frac{\partial \theta_i}{\partial \mathcal{K}_{ab}}\right.$$

$$\left.+\frac{\partial W}{\partial \theta_i}\frac{\partial^2 \theta_i}{\partial \mathcal{K}_{ab}\partial \eta_p}\right)$$

$$\frac{\partial^2 W}{\partial \eta_p \partial \eta_q} = \sum_{i=1}^{3}\sum_{j=1}^{3}\left(\frac{\partial^2 W}{\partial a_i \partial a_j}\frac{\partial a_j}{\partial \eta_q}\frac{\partial a_i}{\partial \eta_p} + \frac{\partial^2 W}{\partial a_i \partial \theta_j}\frac{\partial \theta_j}{\partial \eta_q}\frac{\partial a_i}{\partial \eta_p} + \frac{\partial W}{\partial a_i}\frac{\partial^2 a_i}{\partial \eta_p \partial \eta_q}\right.$$

$$\left.+\frac{\partial^2 W}{\partial \theta_i \partial a_j}\frac{\partial a_j}{\partial \eta_q}\frac{\partial \theta_i}{\partial \eta_p} + \frac{\partial^2 W}{\partial \theta_i \partial \theta_j}\frac{\partial \theta_j}{\partial \eta_q}\frac{\partial \theta_i}{\partial \eta_p} + \frac{\partial W}{\partial \theta_i}\frac{\partial^2 \theta_i}{\partial \eta_p \partial \eta_q}\right)$$

$$\frac{\partial^2 W}{\partial \eta_q \partial \mathcal{K}_{kl}} = \sum_{i=1}^{3}\sum_{j=1}^{3}\left(\frac{\partial^2 W}{\partial a_i \partial a_j}\frac{\partial a_j}{\partial \mathcal{K}_{kl}}\frac{\partial a_i}{\partial \eta_q} + \frac{\partial^2 W}{\partial a_i \partial \theta_j}\frac{\partial \theta_j}{\partial \mathcal{K}_{kl}}\frac{\partial a_i}{\partial \eta_q} + \frac{\partial W}{\partial a_i}\frac{\partial^2 a_i}{\partial \eta_q \partial \mathcal{K}_{kl}}\right.$$

$$\left. + \frac{\partial^2 W}{\partial \theta_i \partial a_j}\frac{\partial a_j}{\partial \mathcal{K}_{kl}}\frac{\partial \theta_i}{\partial \eta_q} + \frac{\partial^2 W}{\partial \theta_i \partial \theta_j}\frac{\partial \theta_j}{\partial \mathcal{K}_{kl}}\frac{\partial \theta_i}{\partial \eta_q} + \frac{\partial W}{\partial \theta_i}\frac{\partial^2 \theta_i}{\partial \eta_q \partial \mathcal{K}_{kl}}\right)$$

$$= \sum_{i=1}^{3}\sum_{j=1}^{3}\left(\frac{\partial^2 W}{\partial a_i \partial \theta_j}\frac{\partial \theta_j}{\partial \mathcal{K}_{kl}}\frac{\partial a_i}{\partial \eta_q} + \frac{\partial^2 W}{\partial \theta_i \partial \theta_j}\frac{\partial \theta_j}{\partial \mathcal{K}_{kl}}\frac{\partial \theta_i}{\partial \eta_q} + \frac{\partial W}{\partial \theta_i}\frac{\partial^2 \theta_i}{\partial \eta_q \partial \mathcal{K}_{kl}}\right)$$

In the non-linear calculation, the minimizing of the strain energy density $W(\boldsymbol{U}, \boldsymbol{\mathcal{K}}; \boldsymbol{\eta})$ with respect to $\boldsymbol{\eta}$ carries out by an updating procedure where the change of $\boldsymbol{\eta}$ is calculated by

$$\frac{\partial^2 W}{\partial \boldsymbol{\eta} \partial \boldsymbol{\eta}} \Delta \boldsymbol{\eta} = -\frac{\partial W}{\partial \boldsymbol{\eta}} \;\Rightarrow\; \Delta \boldsymbol{\eta} = -\left(\frac{\partial^2 W}{\partial \boldsymbol{\eta} \partial \boldsymbol{\eta}}\right)^{-1}\frac{\partial W}{\partial \boldsymbol{\eta}} \tag{4.37}$$

By inserting $\boldsymbol{\eta}$ into the potential, the stress fields and the modulus fields can be calculated via a finite element method presented in Section 2.5.

4.2 Graphite sheet: Young's modulus and Poisson ratio

Ijimia (*1991*) discovered CNTs and predicted SWCNTs' Young's modulus to be about 1TPa. The following years much experimental research had been carried out to confirm CNTs' Young's modulus. Tension tests, bending methods, thermal vibration tests had been applied, and the experimental results of Young's modulus for SWCNTs ranged from 0.81TPa to 1.28TPa (*Wong et al. 1997, Krishnan et al. 1998, Salvatat et al. 1999*). Meanwhile, some researchers concentrated on theoretical studies of the elastic modulus of CNTs. Various theories and

methodologies had been presented, and the reported numerical values for Young's modulus of SWCNTs ranged from 0.5TPa to 6TPa, as shown in Table 4.1. The experimental data demonstrated a large scatter already due to the high frequencies of errors from machines and manual processing at the nano-scale. Compared with a range of 0.47TPa from experimental results, more surprisingly the theoretical results have a range of scatter up to 5.5TPa. *Yakobson* (*1996*) first addressed this ridiculous large scatter of the reported results for CNTs' Young's modulus, which is now known as 'Yakobson's paradox'. *Huang et al.* (*2006*) discussed this issue and identified the cause of 'Yakobson's paradox' as being the 'ill-defined' CNTs' wall thickness from various theories and methodologies and also different types of loading situations.

Theoretically, the tension rigidity, or just 'Eh', should be good enough to present the elastic tension properties of CNTs, however, to compare with other authors' results, here we apply the linear classical continuum mechanics assumption of shell theory, which leads us to solve for Young's modulus E, Poisson's ratio ν, and a case by case defined wall thickness h. The tension rigidity is the 11-11 component of the stretch modulus

$$n_{1111} = \frac{Eh}{1-\nu^2} \tag{4.38}$$

Poisson's ratio is captured in the 11-22 component of the stretch modulus-like tensor

$$n_{1122} = \nu\frac{Eh}{1-\nu^2} \tag{4.39}$$

and the bending rigidity is the dominating component in the bending modulus defined as m^*

$$m^* = \frac{Eh^3}{12(1-\nu^2)} \tag{4.40}$$

From (4.38) to (4.40), Poisson's ratio can be calculated by

$$\nu = \frac{n_{1122}}{n_{1111}} \tag{4.41}$$

The defined tube wall thickness is given by

$$h = \sqrt{12\frac{m^*}{n_{1111}}} \tag{4.42}$$

and Young's modulus is expressed as

$$E = n_{1111}\frac{1-\nu^2}{h} \tag{4.43}$$

In this section, we consider a graphite sheet with the reference configuration being a flat surface lying in the 1-2 plane. Two methods are considered to calculate Young's modulus. One is via tension simulation by stretching the graphite sheet, which provides the results of Poisson's ratio ν and tension rigidity Eh, while the other method is by bending a sheet fixed at one end providing a cantilever which has bending rigidity involved, and so provides the virtual wall thickness to finally compute Young's modulus.

Figure 4.3 shows a sketch of the tension method. A graphite sheet under uni-axial loading is designed. Due to the geometric symmetry, we take one quarter of the sheet, and set the boundary as shown in Figure 4.3, which allows stretching in direction 2 and breathing in direction 1. *b* is the width of the sheet, *L* is the length, and *p* is the uniform stretch loading in direction 2 and *u* is the displacement in axial direction. A zigzag SWCNT is studied, and *L* is chosen to be 8nm, while *b* is changing from 1nm to 8nm.

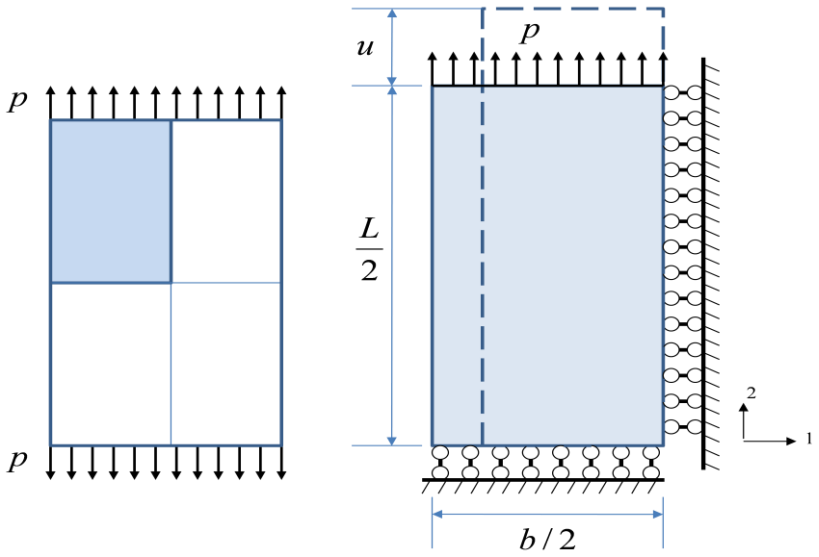

Figure 4-3: Graphite sheet under uniform stretch loading

Young's modulus E can be also calculated with the stress-strain ($\sigma - \varepsilon$) relation as

$$\sigma = \frac{p}{h} = E\varepsilon \tag{4.44}$$

The p-ε relation is given in Figure 4.4 for b=1, 2 and 3nm, where the vertical axis p is defined by units of force per length and the horizontal axis is the change in length. The p-ε relation is non-linear, which means the modulus-like tensor and further the tension rigidity both change when the loading increases. As Figure 4.4 shows, there is a trend that the tension rigidity decreases with an increasing sheet width, but the beginning ratios for all cases have only small differences. The values, i.e. the tension rigidity, change from 240 N/m to 800 N/m. If the initial value is chosen to be the tension rigidity, which provides Eh= 240 N/m (0.240TPa.nm), the result is similar to the values obtained from *Arroyo and Belytschko* (*2004*), *Guo et al.* (*2006*), and *Wang et al.* (*2006*), where results of SWCNTs' Young's modulus up to 0.69TPa with wall thickness of 0.334 or 0.34nm, i.e. Eh=0.230 or 0.235TPa.nm were presented.

If we do not consider the initial value to calculate Young's modulus, some value in the non-linear p-ε relation curve has to be found to define it. For simplicity, one can select a changing point as shown in Figure 4.4, and calculate the proportional ratio as well as the value of Eh. Alternatively, we select the changing point and define a selected area, e.g. 50 points around the selected point, and refer to the values of n_{1111} and n_{1122}, and then calculate the average value of Eh and ν . The latter method is chosen here. From the selected point and selected area, we find the stretch modulus-like tensor components, and then from the relation of tension rigidity and shear component, the results have been computed with an average Eh=320.5N/m and an average Poisson ratio of 0.395. If the wall thickness is chosen to be 0.34nm, which is the effective SWCNT wall thickness provided by most of other authors, then Young's modulus of graphite sheet attains the value of 0.943TPa, which is within the range of experimental results.

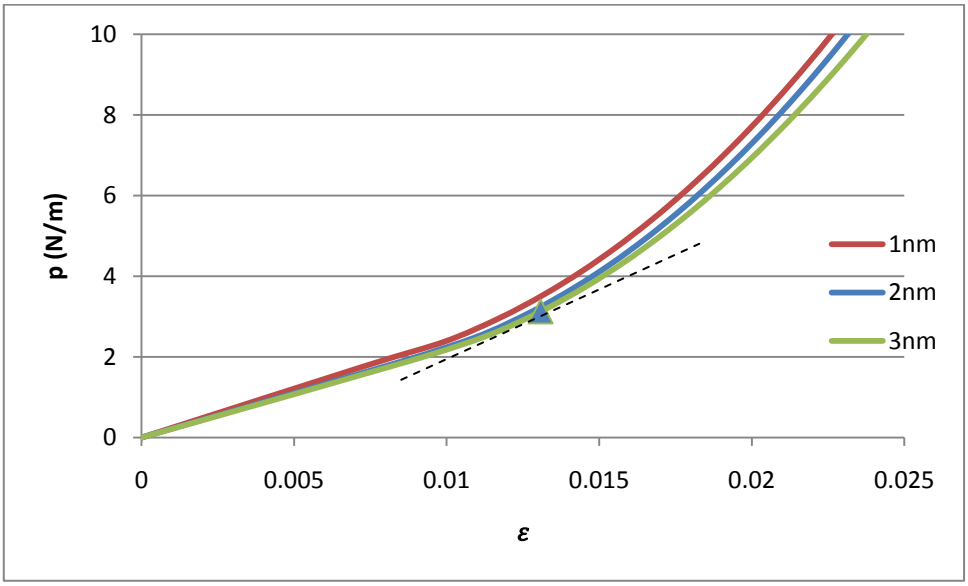

Figure 4-4: Strain and stretch loading relationship from tension method

The bending method is sketched in Figure 4.5. A cantilever graphite sheet is under uniform loading in the third direction. A zigzag SWCNT with L = 8nm, while b is changing from 1nm to 8nm, is investigated. The loading and displacement relationship is also non-linear, so we use the same method to select the point and area and find the dominating bending modulus-like tensor component from the calculation. With the bending method, and from the relation of the bending rigidity and tension rigidity, an average Young's modulus of graphite sheet of 5.526TPa is calculated, with a corresponding average wall thickness of 0.058nm. A comparison of numerical results for Young's modulus, wall thickness and tension rigidity of SWCNTs or graphite sheets with other authors is presented in Table 4.1.

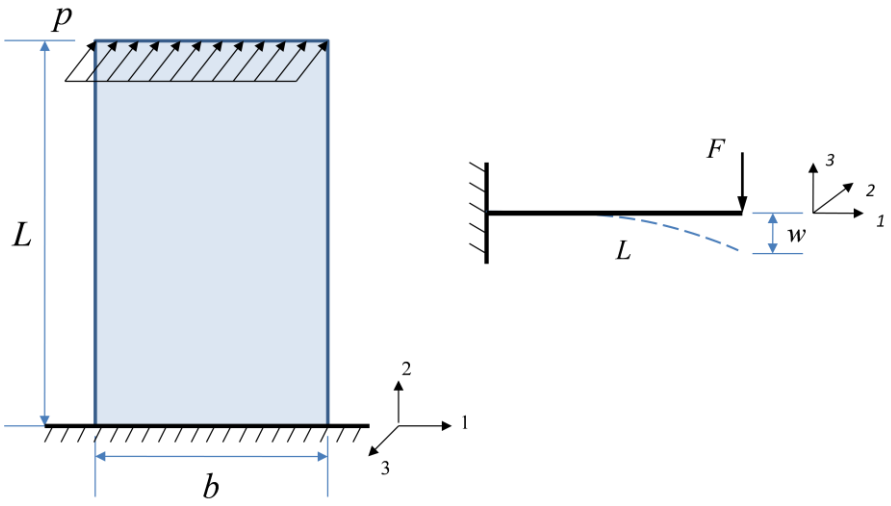

Figure 4-5: Graphite sheet under bending with uniform loading at the free end

It shows little differences of Young's modulus and Possion ratio with respect to the sheet width and sheet aspect ratio b/L in this graphite sheet computation.

Natsuki et al. (*2004*) calculated Poisson ratio, they presented results varied from 0.27 to 0.33 for zigzag SWCNTs. *Avila and Lacerda* (*2008*) reported an average Poisson value of SWCNTs ranging from 0.15 to 0.29. *Arroyo and Belytschko* (*2004*) applied expentential Cauchy-Born rule by using the first generation Tersoff-Brenner potential and gave poisson ratio to be 0.412. *Guo et al.* (*2006*) used higher order Cauchy-Born rule by using the same interatomic potential form as *Arroyo and Belytschko* (*2004*), and they obtained Poisson ratio to be 0.429. The Poisson ratio obtained from second generation Brenner potential, which is closer to the ones reported from atomistic methods, is observed to be lower than the one computed from first generation potentials which proves that the second generation Brenner potential is more adequate to describe the internal structure of CNTs.

Table 4-1: Comparison of Young's modulus and tension rigidity

Authors	Wall thickness h (nm)	Young's modulus E (TPa)	Tension rigidity Eh (N/m)
Yakobson et al. (1996)	0.066	5.5	363.0
Hernandez et al. (1998)	0.34	1.24	421.6
Zhou et al. (2000)	0.074	5.1	377.4
Tu and Ou-yang (2002)	0.075	4.7	352.5
Gao and Li (2003)	0.066	5.5	363.0
Jin and Yuan (2003)	0.34	1.238	420.9
Li and Chou (2003)	0.34	1.01	343.4
Pantano et al. (2004)	0.075	4.84	363.0
Tserpes and Papanikos (2005)	0.147	2.395	352.1
Guo et al. (2006)	0.34	0.69	234.6
Wang et al. 1 (2006)	0.34	0.69	234.6
Meo and Rossi (2006)	0.34	0.945	321.3
Wang et al. 2 (2006)	0.334	1.01	337.3
Avila and Lacerda (2008)	0.34	1.005	341.7
Lei et al. (2011)	0.34	1.04	353.6
Parvaneh and Shariati (2011)	0.34	1.170	397.8
Present	0.058	5.526	320.5

4.3 **Cylindrical shell model: tension**

Cylindrical shell model under stretch is designed as shown in Figure 4.6. Uniform stretching load is applied at both ends of the cylindrical shell. The length of the tube is fixed to L=8nm, the load at both ends is of a constant value of F=16nN, while the uniform load applied is p=16nN/b, with b being the width of sheet and $b = \pi D$, where D is the diameter of the tube, and u is the displacement. Since the displacement and force curve is non-linear, it is again flexible to choose which tangent value to go for and we decide to use a different method from Section 4.2. So we choose the alternative straight forward method, in this case, to calculate SWCNT's Young's modulus directly from the displacement u, with the relation

$$\sigma = \frac{p}{h} = E\varepsilon \;\Rightarrow\; E = \frac{F}{bh}\cdot\frac{L}{u} = \frac{FL}{\pi Dhu} \tag{4.45}$$

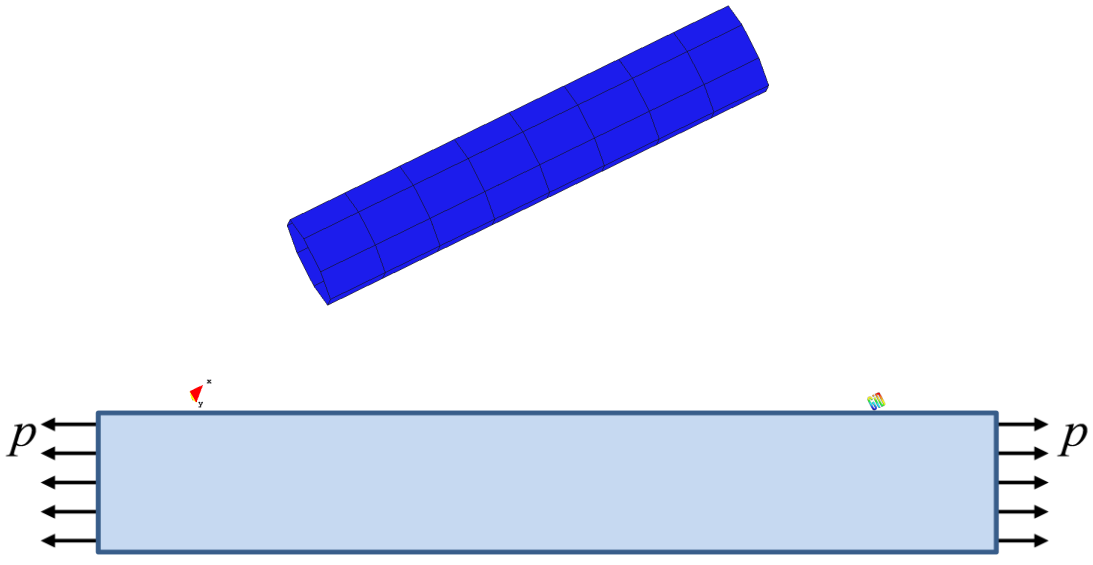

Figure 4-6: Sketch of cylindrical shell model under tension

First, an armchair SWCNT is studied and tube diameters are chosen from 0.407nm increasing to 4.746nm, i.e. from (3,3) to (35,35) armchair SWCNTs. In order to compare the results reasonably with other authors' results, the effective wall thickness is chosen to be 0.34 nm as they did. Part of the results of deformations of SWCNT under stretching are shown in Figure 4.7. Results of values are listed in Table 4.2. The dependence of Young's modulus of armchair SWCNT on tube diameter is shown in Figure 4.8.

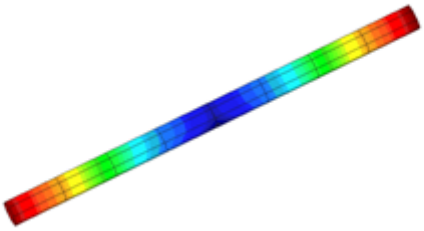

(a) Deformation of cylindrical shell under tension (D=0.542nm; L=8nm)

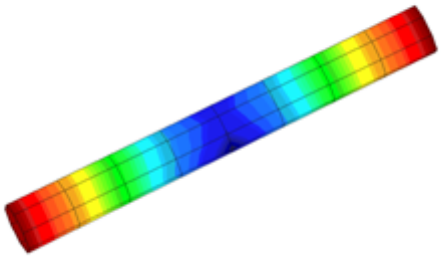

(b) Deformation of cylindrical shell under tension (D=0.949nm; L=8nm)

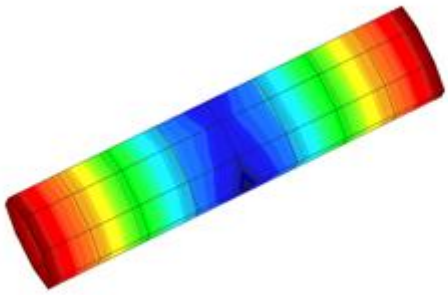

(c) Deformation of cylindrical shell under tension (D=1.898nm; L=8nm)

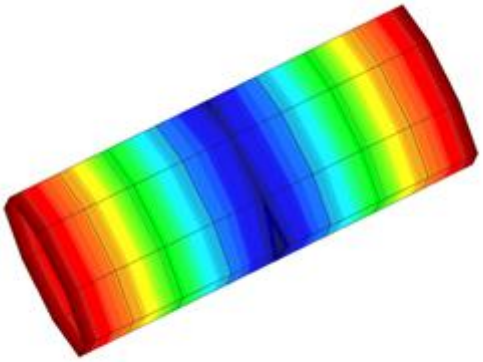

(d) Deformation of cylindrical shell under tension (D=3.254nm; L=8nm)

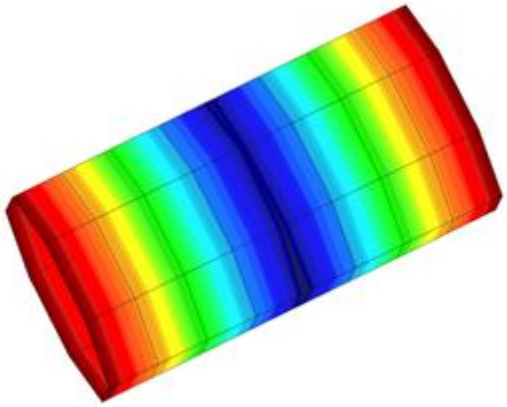

(e) Deformation of cylindrical shell under tension (D=4.339nm; L=8nm)

Figure 4-7: Deformation of cylindrical shell model under tension

Table 4-2: Dependence of Young's modulus on tube diameter for armchair SWCNTs

Diameter D (nm)	Displacement u (nm)	Tension rigidity Eh (N/m)	Young's modulus (TPa)
0.542	0.226237	332.0	0.977
1.085	0.134154	280.0	0.823
1.492	0.103227	264.6	0.778
1.898	0.083827	256.0	0.753
2.305	0.070461	250.8	0.738
2.848	0.057684	248.0	0.730
3.390	0.048704	246.8	0.726
3.797	0.043567	246.3	0.724
4.746	0.035005	245.2	0.721

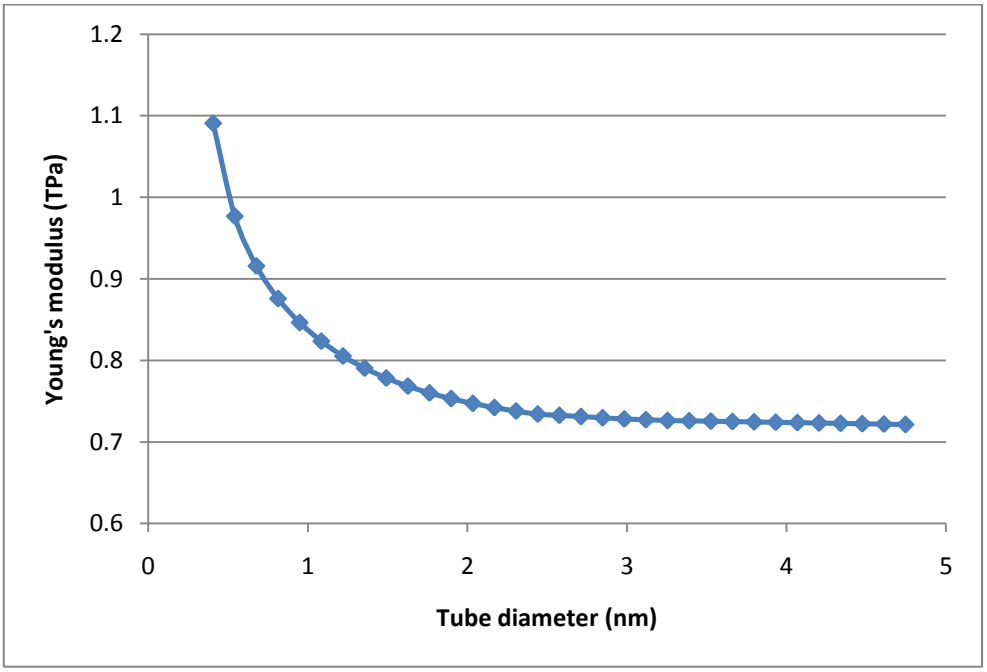

Figure 4-8: Dependence of Young's modulus on tube diameter for armchair SWCNTs

The same method is applied to zigzag SWCNTs with length L=8nm, and F= 16nN. Accordingly, (6,0) to (60,0) zigzag SWCNTs are studied. Part of the results are listed in Table 4.3. The resulting values of Young's modulus for zigzag SWCNTs as well as for armchair SWCNTs are converging at 0.72TPa. *Parvaneh and Shariati* (*2011*) applied atomistic modelling with the help of the software ABAQUS, produced results for Young's modulus of zigzag SWCNTs under axial tension and compared it with two other authors, as shown in Figure 4.10. The results computed in this research, as shown in Figure 4.9, are in good agreement with *Natsuki et al.* (*2003*) when the tube diameter is less than 1nm, and the results are in good agreement with *Shen and Li* (*2004*) when tube diameter is larger than 1nm.

Table 4-3: Dependence of Young's modulus on tube diameter for zigzag SWCNTs

Diameter D (nm)	Displacement u (nm)	Tension rigidity Eh (N/m)	Young's modulus (TPa)
0.470	0.212707	407.8	1.199
0.783	0.157699	330.0	0.971
1.252	0.113149	287.5	0.846
1.722	0.088466	267.4	0.786
2.192	0.072412	256.7	0.755
2.662	0.060748	252.0	0.741
3.131	0.052113	249.7	0.734
3.601	0.045597	248.1	0.730
4.697	0.035132	246.9	0.726

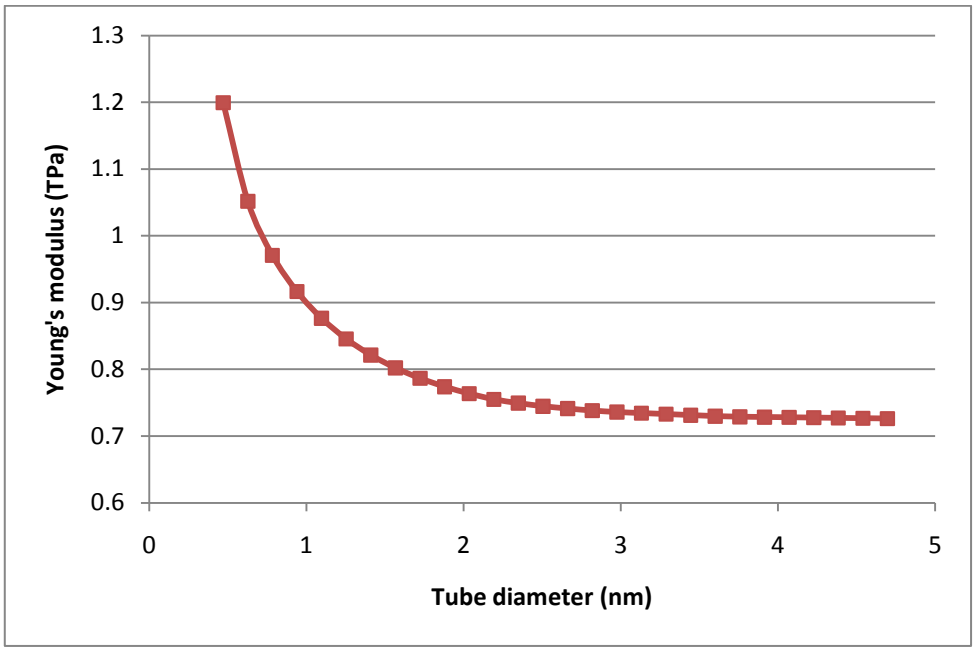

Figure 4-9: Dependence of Young's modulus on tube diameter for zigzag SWCNTs

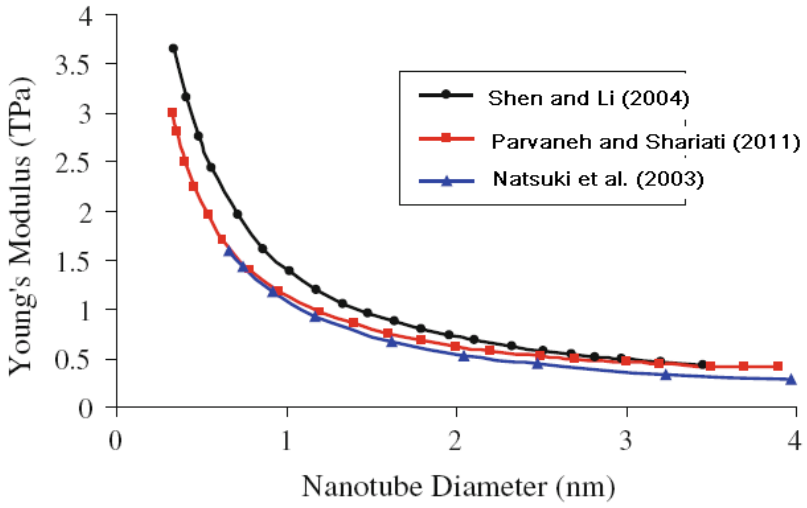

Figure 4-10: Dependence of Young's modulus on tube diameter for zigzag SWCNTs (*Parvaneh and Shariati, 2011*)

Lei et al. (*2011*) presented a molecular mechanics model to predict Young's modulus of SWCNTs. They obtained the curve of results with the same trend, as shown in Figure 4.12, although they arrived a minimum value of Young's modulus around 1.04TPa, and showed that Young's modulus of zigzag SWCNTs

is slightly larger than the one of armchair SWCNTs. We obtained comparable results, and the values become very close with the tube diameter increasing.

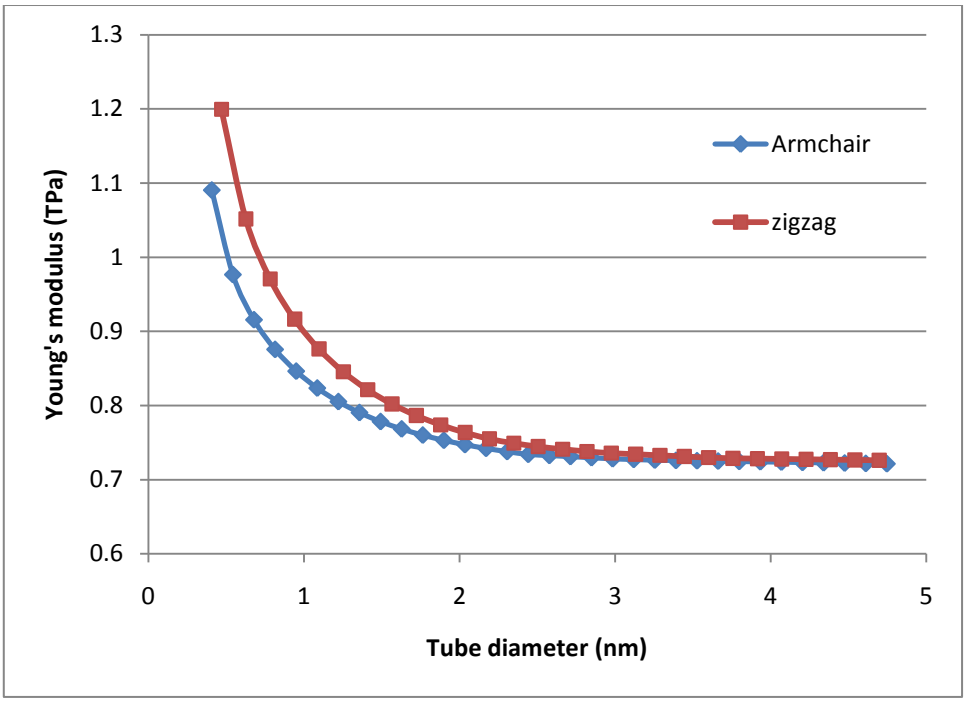

Figure 4-11: Comparison of Young's modulus for armchair and zigzag SWCNTs

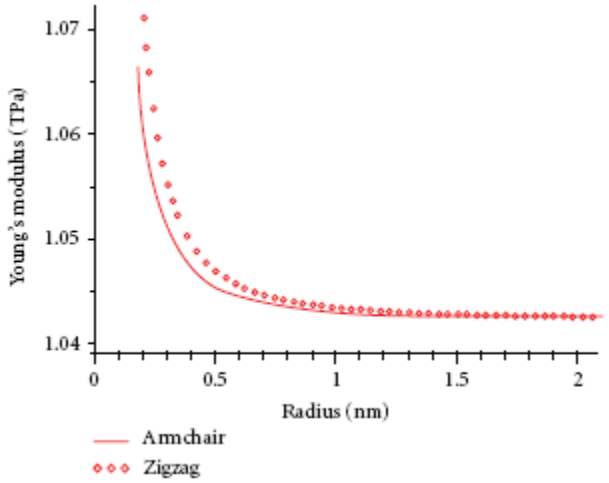

Figure 4-12: Comparison of Young's modulus for armchair and zigzag SWCNTs (*Lei et al. 2011*)

4.4 Cylindrical shell model: bending

4.4.1 One end fixed bending

First a cylindrical shell under bending is considered with one end fixed and external force applied at the free end, as shown in Figure 4.13. An armchair SWCNT is modelled, with length L=16nm and a diameter changing from 0.407nm to 4.746nm. The deformation after bending is as shown in Figure 4.14.

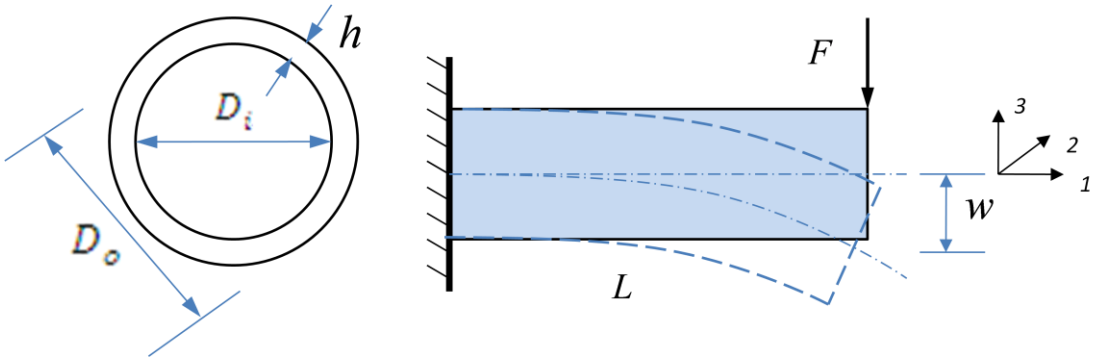

Figure 4-13: Sketch of one end fixed cylindrical shell model under bending

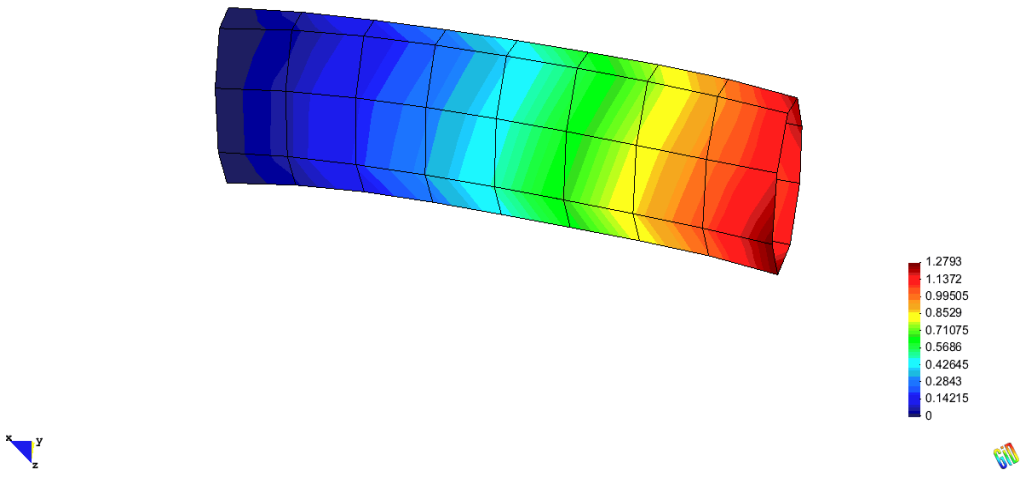

Figure 4-14: Deformation of one end fixed cylindrical shell under bending (D=4.339nm; L=16nm)

Within small deformations, from classical continuum mechanics beam theory, the deflection at the free end has a relation with the external force as

$$w = \frac{FL^3}{3EI} \;\Rightarrow\; EI = \frac{FL^3}{3w} \tag{4.46}$$

I is the cross section moment of inertia which is calculated as

$$I = \frac{1}{64}\pi(D_o^4 - D_i^4) \tag{4.47}$$

with D_o and D_i as the outer and inner diameters of the cylindrical cross section, as shown in Figure 4.13. If h is defined as the thickness of the shell, then $D_o = D + h$ and $D_i = D - h$, where D is the diameter of the mid-surface of the cylindrical shell. Hence

$$I = \frac{1}{8}\pi(D^3 h + D h^3) \tag{4.48}$$

which means that with the bending rigidity *EI* obtained from this model and the tension rigidity *Eh* computed from a cylindrical shell stretching model, we can compute the shell thickness as we did in the graphite sheet model.

Results of bending rigidity *EI* against diameter are shown in Figure 4.15. Young's modulus, calculated for *h*=0.34nm, is shown in Figure 4.16. For models with diameter under 1nm, we obtain extremely high values of Young's modulus, but with the diameter increasing to more than 2nm, it tends to be steady around 0.72 TPa, similar to the results obtained from the cylindrical shell tension model, only slightly larger. Young's modulus has been calculated for *h*=0.058nm, as well as for *h*=0.34nm and for *h*=0.15nm. The results computed from cylindrical shell tension model, and from this bending model with different tube thicknesses are compared in Figure 4.17. For three sets of different diameters separately, they all converge to the same value eventually, for *h*=0.34nm *E*=0.72TPa, for *h*=0.15nm

E=1.62TPa, and for h=0.058nm E=4.26TPa. By observing the results, it is obvious that for predicting Young's modulus, tension models give much more stable results compared to bending models.

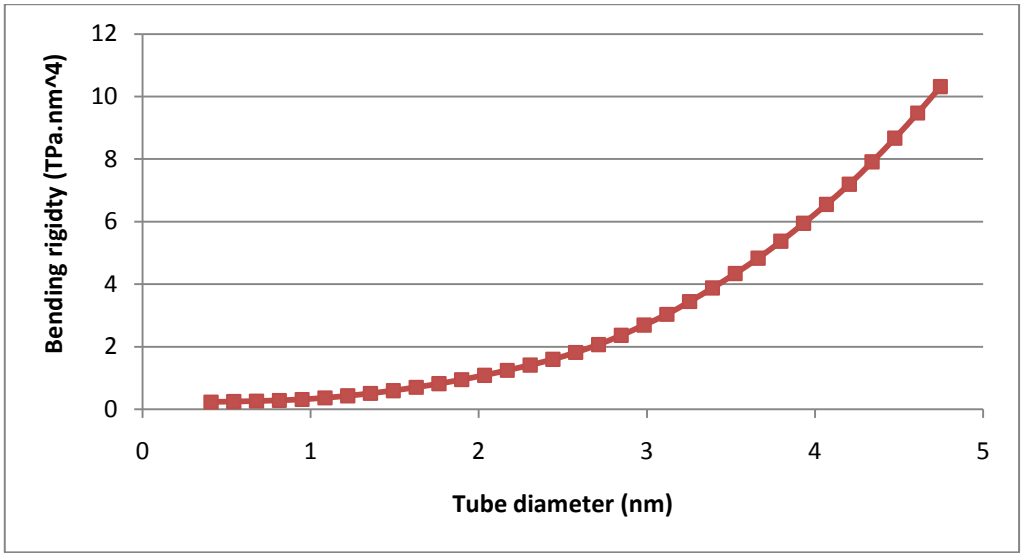

Figure 4-15: Relationship of bending rigidity against tube diameter (one end fixed bending)

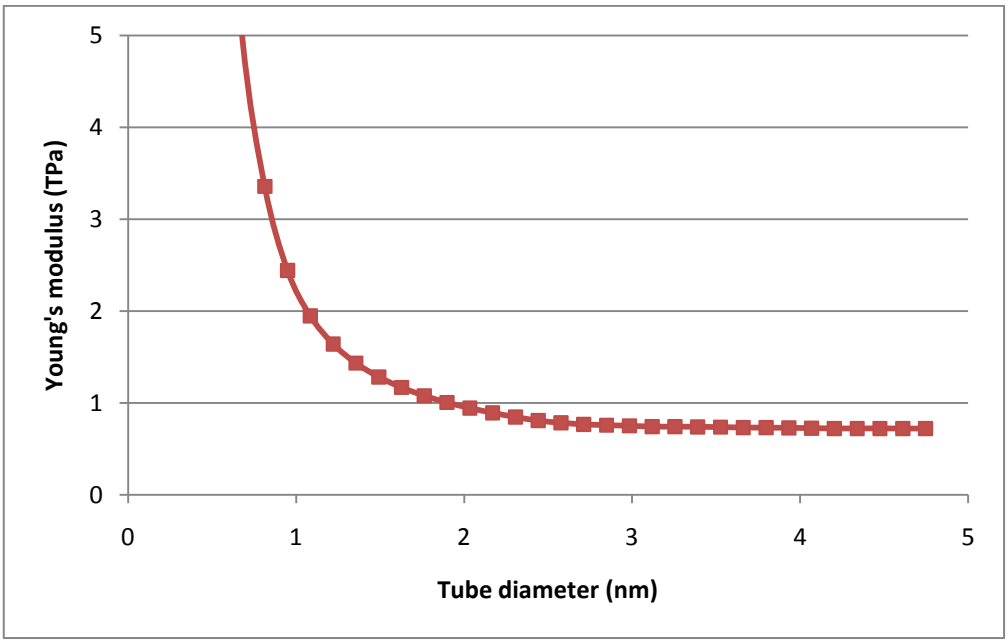

Figure 4-16: Relationship of Young's modulus against tube diameter for cylindrical shell mode under bending (one end fixed bending)

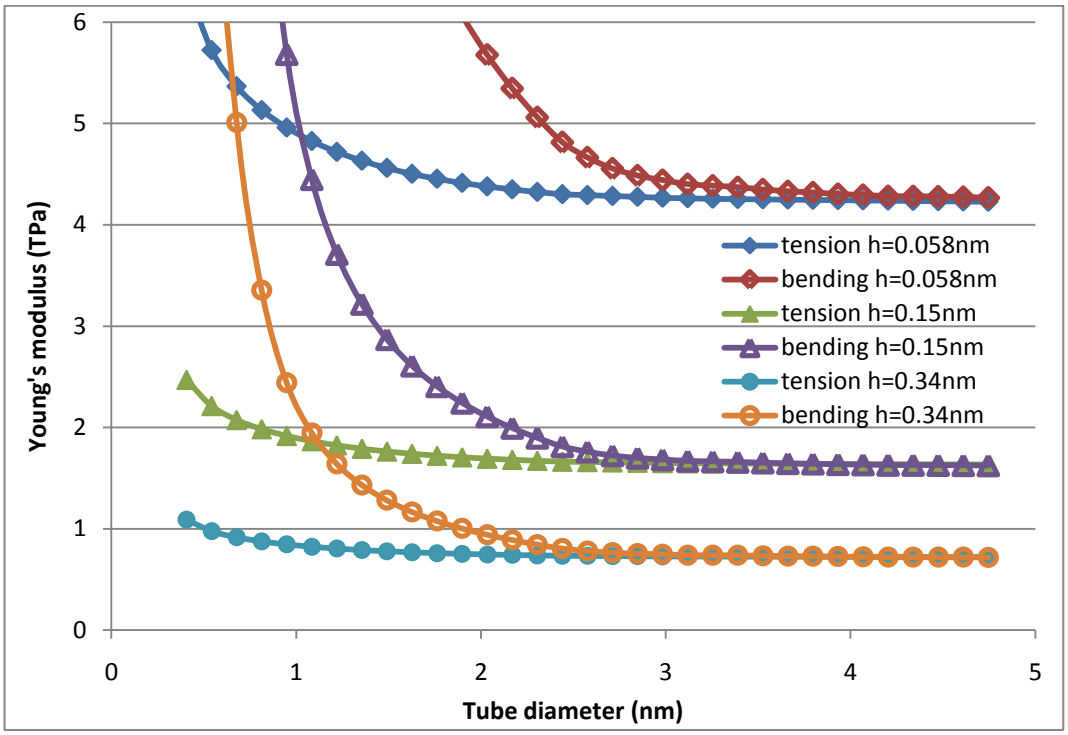

Figure 4-17: Comparison of Young's modulus for cylindrical shell model from tension method and bending method with different wall thickness (*h*)

Gao and Li (*2003*) applied a simple Bernoulli-Euler beam theory and used molecular potential energy. By considering bending for a graphite sheet treated as a unrolled SWCNT, they derived similar curve for Young's modulus as function of the wall thickness as shown in Figure 4.18.

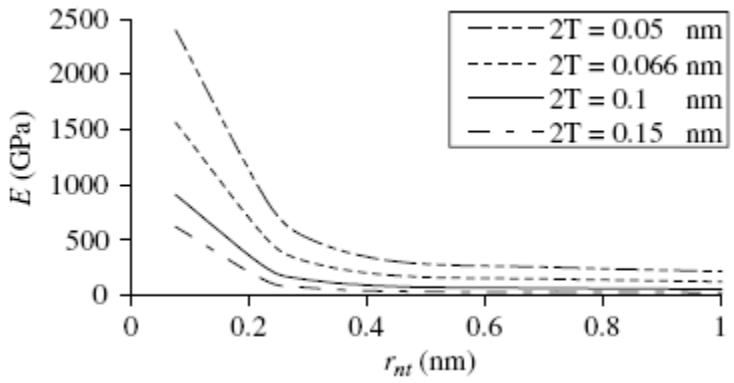

Figure 4-18: Young's modulus varying with SWCNT wall thickness (2T) (*Gao and Li, 2003*)

4.4.2 Two end fixed bending

A second example of cylindrical shell model under bending is designed with both ends fixed and an external force applied in the middle, as shown in Figure 4.19. An armchair SWCNT with length L=16nm and a diameter changing from 0.407nm to 4.746nm, is studied. Deformation after bending is shown in Figure 4.20.

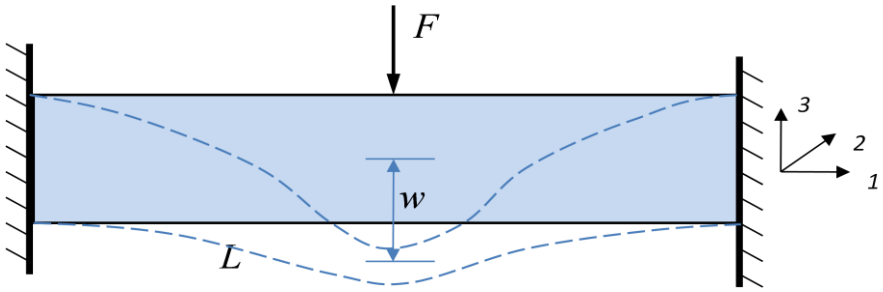

Figure 4-19: Sketch of two end fixed cylindrical shell model under bending

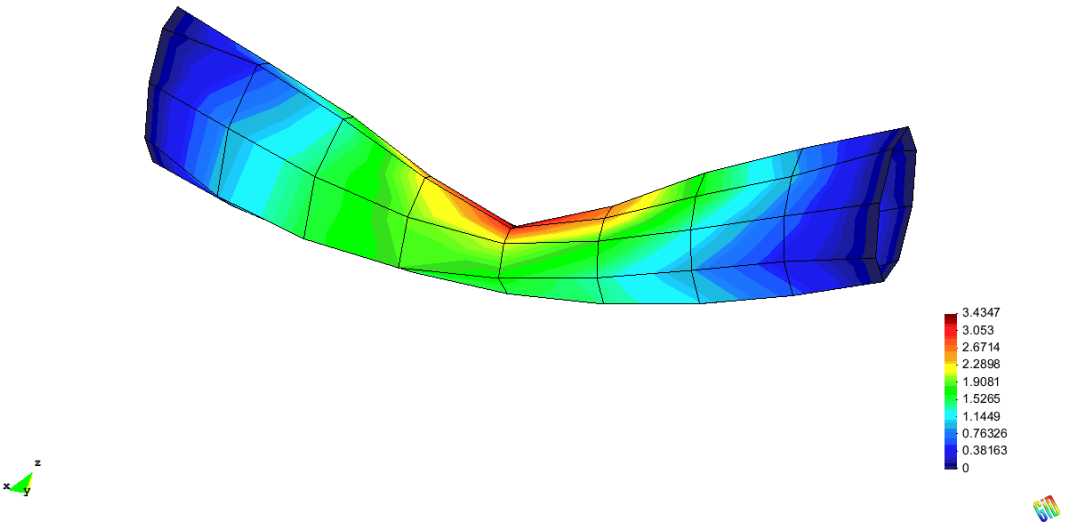

Figure 4-20: Deformation of two end fixed cylindrical shell under bending (D=3.390nm; L=16nm)

From classical continuum beam theory, the deflection in the middle of the beam has a relation with the external force as

$$w = \frac{FL^3}{192EI} \Rightarrow EI = \frac{FL^3}{192w} \tag{4.49}$$

The results of bending rigidity *EI* against diameter as well as comparisons with results from the case of one end fixed cylindrical shell are shown in Figure 4.21. Results of Young's modulus calculated for h=0.34nm and comparisons with results from cylindrical shell tension method and cylindrical shell with one end fixed model are shown in Figure 4.22.

As for Young's modulus, two end fixed model also presents a super large value for those sets with tube diameter under 1.5nm, which might be caused by the effects of the large ratio between tube wall thickness and the small tube diameter in application of shell theory in bending situation. These large values drop down fast with tube diameter increasing. Not only with this drawback, the model does not produce Young's modulus converging at 0.72TPa, the value keeps going down towards zero with a large tube diameter. This might be caused by the local bending of SWCNT structure. As demonstrated by *Parvaneh and Shariati* (*2011*) with atomistic modelling, for two end fixed SWCNTs, there was global bending which happened with a large aspect ratio (*L/D*), and there was local bending that happened with a small aspect ratio, as shown in Figure 4.27. With local bending of SWCNT, the bending happens at the surface of the tube locally and does not affect properties for the rest of the tube, therefore the elastic properties of SWCNTs cannot be calculated with equations from classical continuum beam theory anymore.

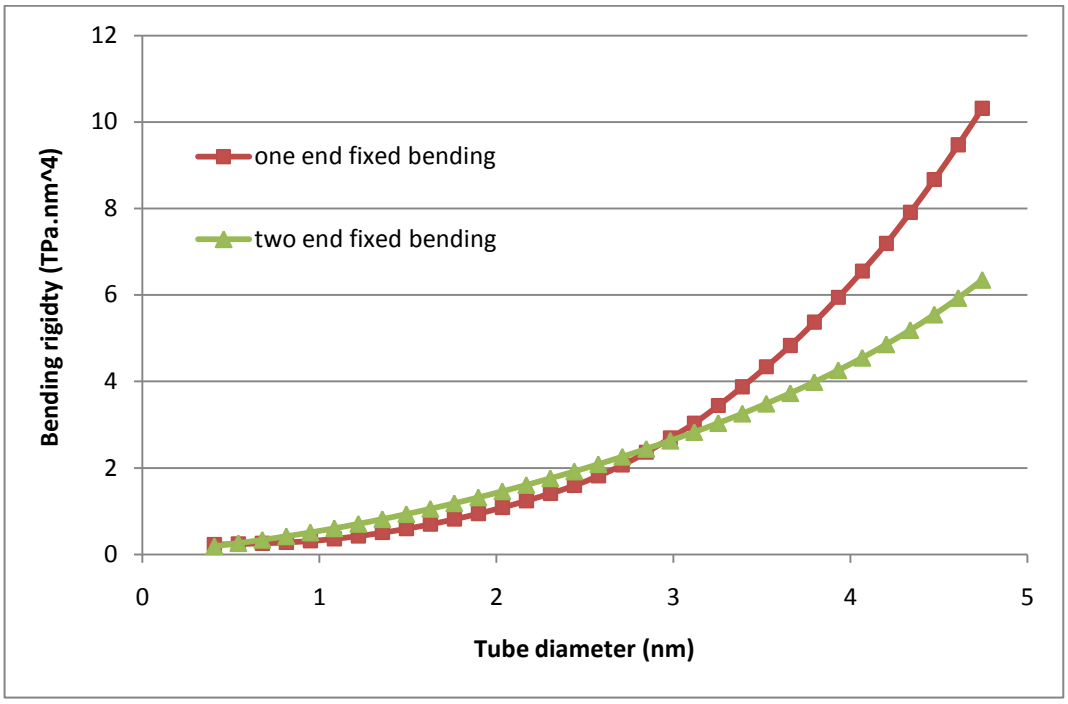

Figure 4-21: Relationship of bending rigidity against tube diameter and comparison (two end fixed bending)

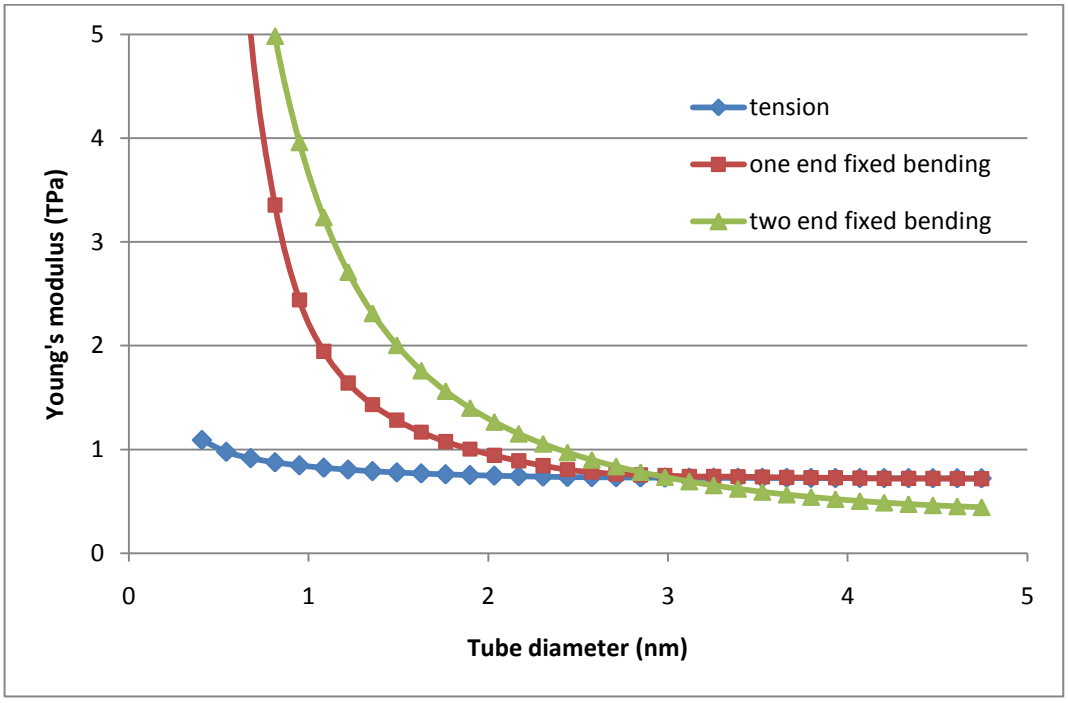

Figure 4-22: Relationship of Young's modulus against tube diameter for cylindrical shell mode under bending and comparison (two end fixed bending)

4.4.3 Simply supported bending

This cylindrical shell model is designed to be simply supported and with external force applied in the middle, as shown in Figure 4.23. An armchair SWCNT with length L=16nm and a diameter changing from 0.407nm to 4.746nm, is studied. Deformation after bending is shown in Figure 4.24.

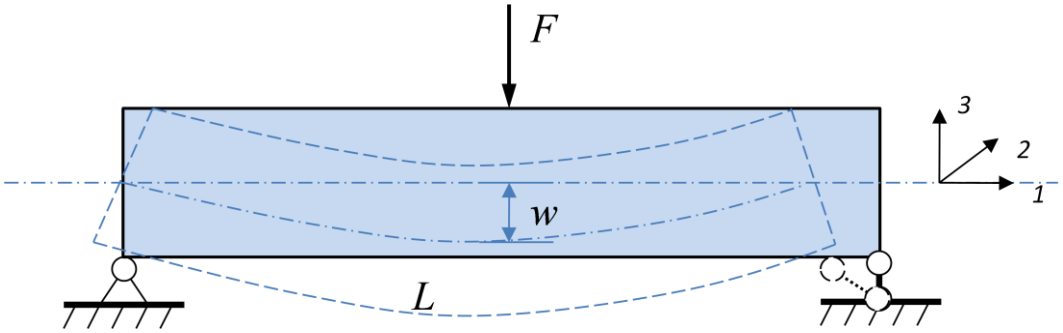

Figure 4-23: Sketch of simply supported cylindrical shell model under bending

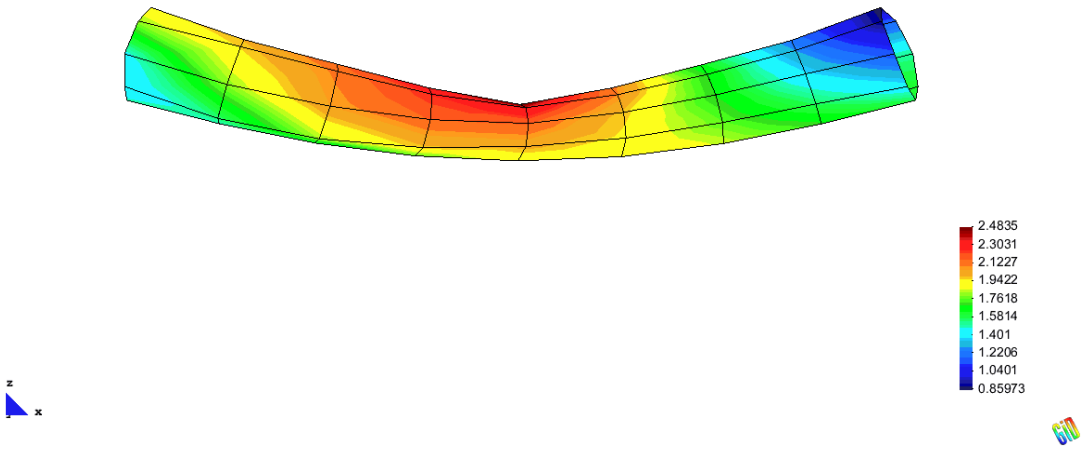

Figure 4-24: Deformation of two end fixed cylindrical shell under bending (D=1.898nm; L=16nm)

Under small deformation, classical continuum beam theory gives the deflection in the middle of the beam related to the external force as

$$w = \frac{FL^3}{48EI} \Rightarrow EI = \frac{FL^3}{48w} \tag{4.50}$$

Results from the bending rigidity *EI* against diameter and comparisons with the other two bending models are shown in Figure 4.25. The pattern of bending rigidity from simply supported cylindrical shell model is similarly parallel to the pattern of the two fixed end model. A value of *EI* for the tension model is also calculated, with Young's modulus obtained from the tension model and the cross sectional moment of inertia for tube diameter *h*=0.34nm. The values are slightly smaller than the ones obtained from the one end fixed bending model but they coincide after 3nm.

Young's modulus is also computed for simply supported bending model with wall thickness *h*=0.34nm and comparisons with the other two bending models along with cylindrical shell tension model is shown in Figure 4.26. The result for Young's modulus is that it is smaller in the case of simply supported cylindrical shell model than in the case of two end fixed bending model. The values drop down fast and tend towards zero as those given by the two end fixed bending model. At diameter between 2.2 nm and 3.4nm, i.e. aspect ratio between 4.7 and 7.3, all four sets of models can provide reasonable results. When the diameter is smaller than 1nm, three sets of bending models produce unreasonable large values of Young's modulus, which might be because that the tube radius is similar to the tube thickness, then Cosserat surface which models SWCNT becomes a thick shell, or even an almost solid beam, therefore the result of calculation from

Cosseart surface shell theory is no longer valid anymore in the bending situation. When the tube diameter is larger than 3nm, the tension model and the one end fixed bending model provide similar Young's modulus of 0.72TPa, whereas the two end fixed and simply supported cylindrical shell model produce results towards zero, which is not reasonable, since the local bending mode as mentioned before would be involved and the SWCNT structure at the surface might have changed, thus the equations from classical elastic beam theory can no more be applied for computations.

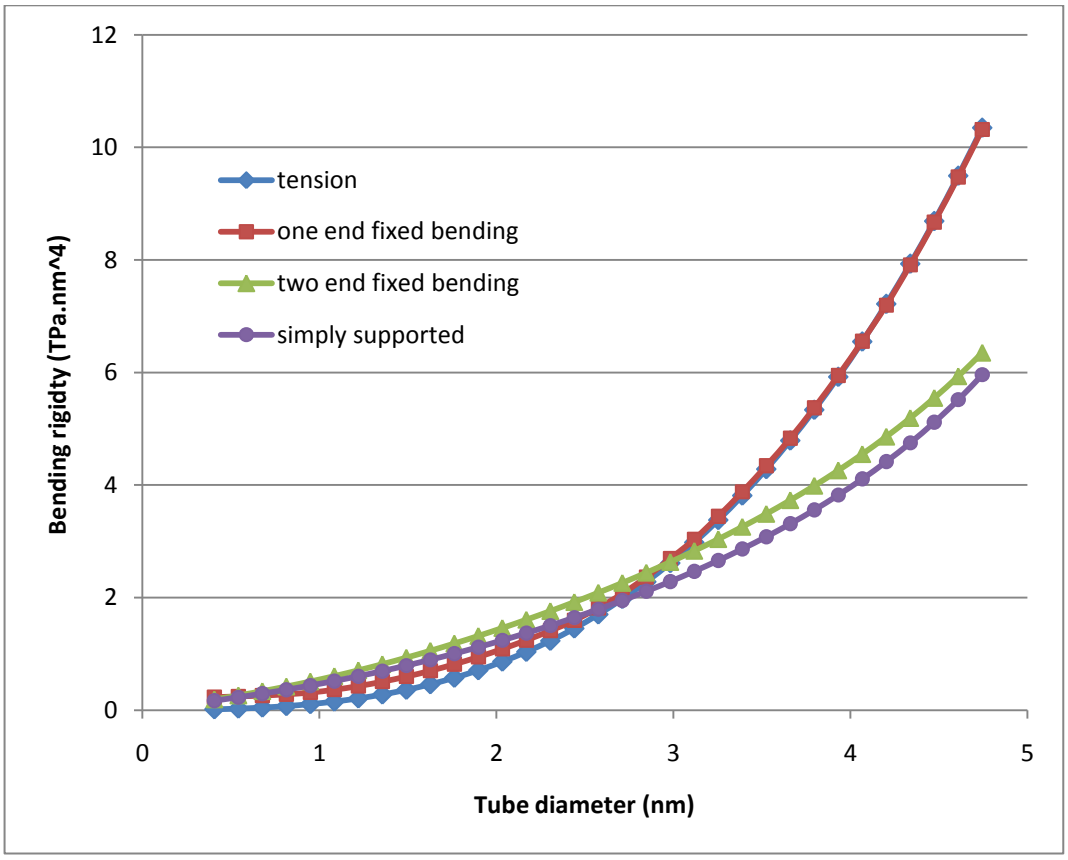

Figure 4-25: Relationship of bending rigidity against tube diameter and comparison (two end fixed bending)

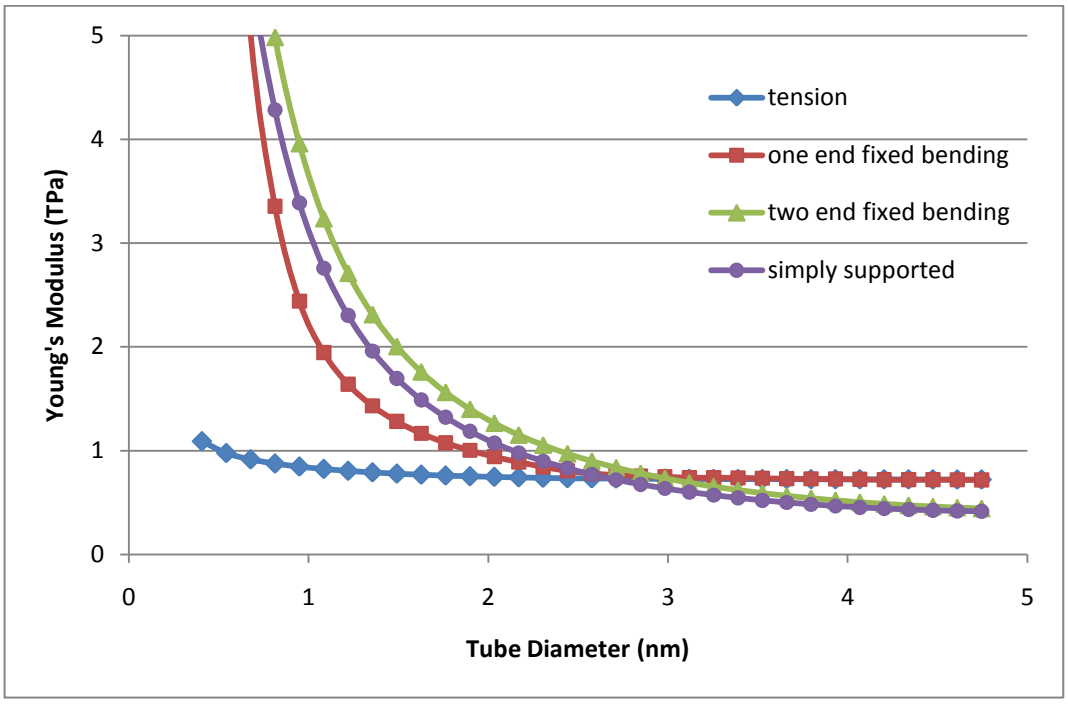

Figure 4-26: Relationship of Young's modulus against tube diameter for cylindrical shell mode under bending and comparison (two end fixed bending)

From all the results shown above, a conclusion is drawn with respect to the application of shell model for SWCNT in bending, that in case of prediction of Young's modulus, direct tension model can provide reasonable results, and one end fixed bending model can produce similar results with a large tube diameter, whereas two end fixed and simply supported bending models only can be trusted within certain range. All three sets of bending models lead to unreasonable large values of Young's modulus when the tube diameter is smaller than 1nm, which indicates that bending models in calculation of Young's modulus have to be applied carefully, and a serious consideration should be taken before using equations from classical beam theory or shell theory because some of the assumptions may not be valid any more when the wall thickness and the tube

diameter are of the same order, or when the inner structure of SWCNT changes during the calculation.

Parvaneh and Shariati (*2011*) adopted atomistic modelling and presented four type of bending deformations with, (a) global bending of one end fixed SWCNT, (b) local bending of two end fixed SWCNT, (c) global bending of two end fixed SWCNT, and (d) global bending of simply supported SWCNT. We simulate the same four types of bending modes, as shown in Figure 4.28.

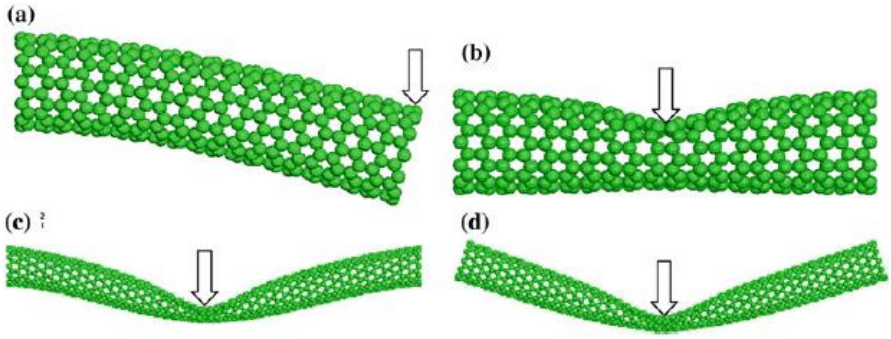

Figure 4-27: Global bending and local bending of SWCNTs (*Parvaneh and Shariati, 2011*)

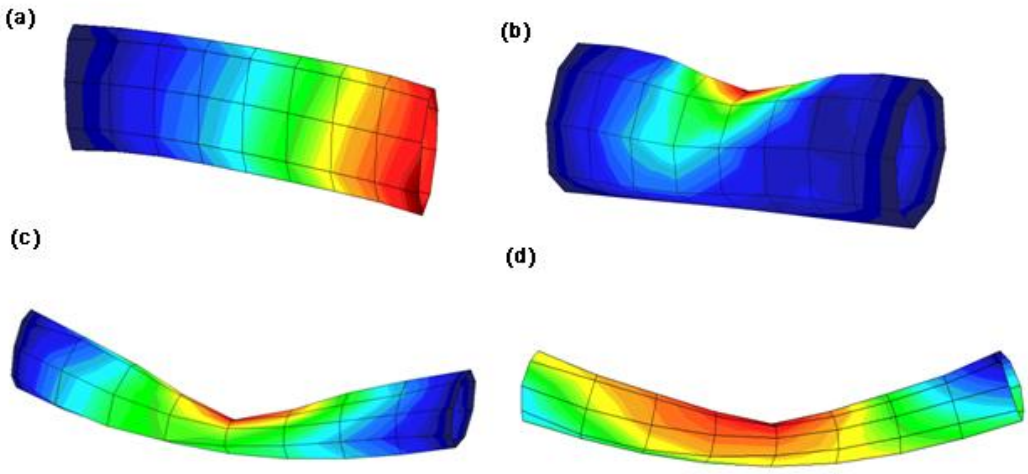

Figure 4-28: Different bending modes of SWCNTs

4.4.4 Two end fixed bending (under uniform loading)

Yang and E (*2006*) suggested an example of an armchair SWCNT, where a force was applied to each atom of the tube in vertical direction. The configurations of the deflected SWCNT are shown in Figure 4.29. And the maximum deflections of SWCNT calculated by molecular dynamics (MD), Euler-Bernoulli beam theory (linear) and local Cauchy-Born rule (LBC) are shown in Figure 4.31.

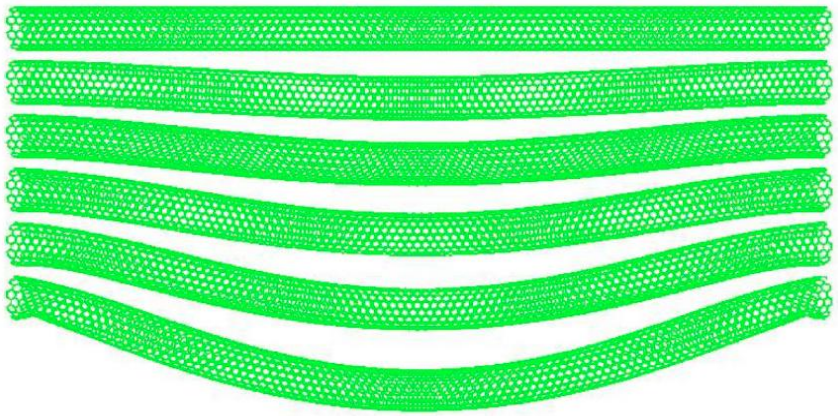

Figure 4-29: Configurations of deflected armchair SWCNT (*Yang and E, 2006*)

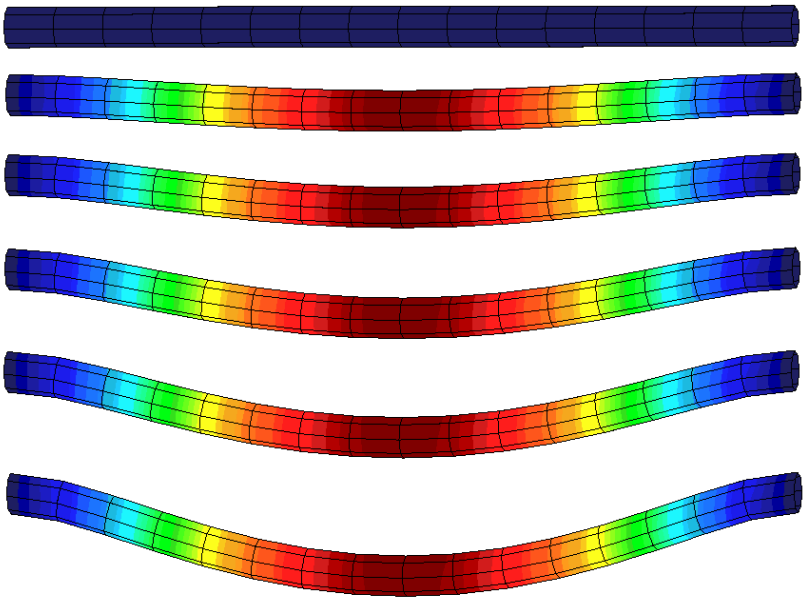

Figure 4-30: Configurations of deflected armchair SWCNT under uniform loading

Similar calculation is carried out in this research for a (9,9) armchair SWCNT with tube length L=24nm. The configurations of deflected SWCNT are shown in Figure 4.30, and the relationship between maximum deflection and external load is shown in Figure 4.31. Both of the figures are in good agreement with results from *Yang and E* (*2006*). They pointed out that, with large deflection, continuum theory will no longer hold because two ends of the tube will buckle as shown for the last tube in Figure 4.29 and Figure 4.30.

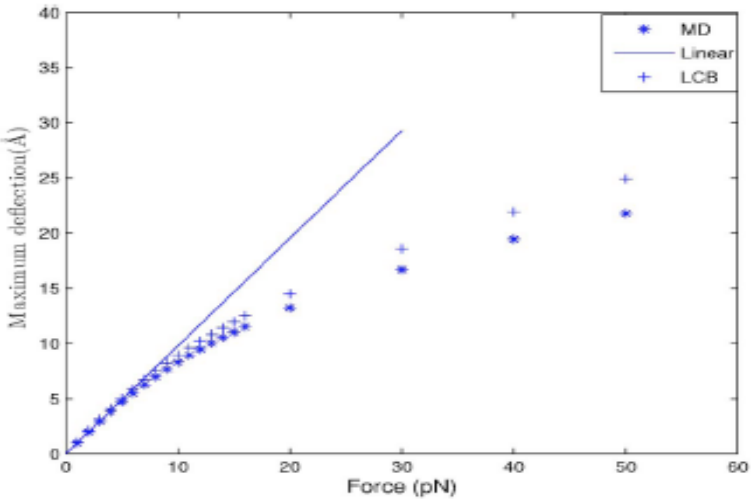

Figure 4-31: Relationship of maximum deflection and external load (*Yang and E, 2006*)

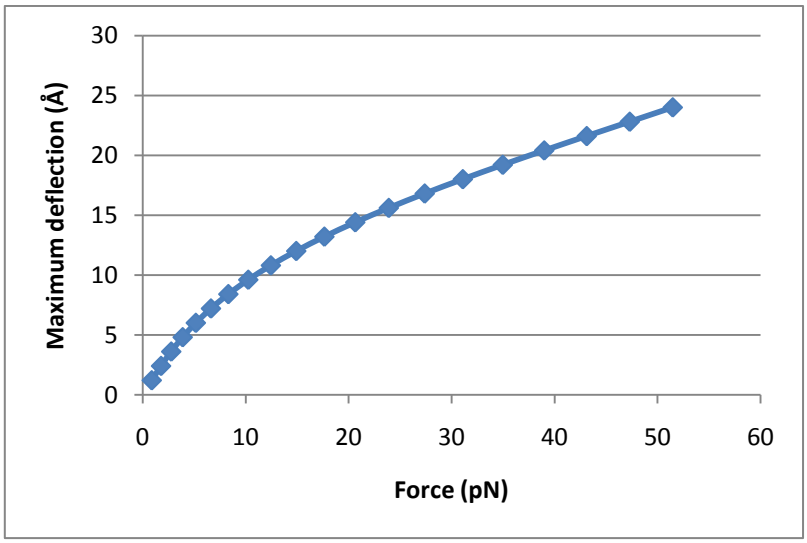

Figure 4-32: Relationship of maximum deflection and external load

4.5 **Cylindrical shell model: buckling**

For one end fixed cylindrical shell, two types of buckling modes have been observed in this research, as shown in Figure 4.33. *Yakobson et al.* (*1996*) adopted molecular dynamics method to simulate buckling of SWCNTs under axial compression, and provided the simulations as shown in Figure 4.34. Our cylindrical shell in this research is able to capture the first two buckling patterns.

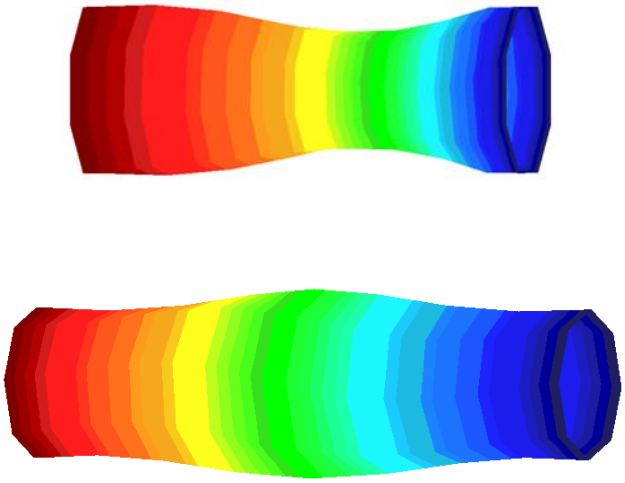

Figure 4-33: Two buckling patterns of SWCNTs under axial compression

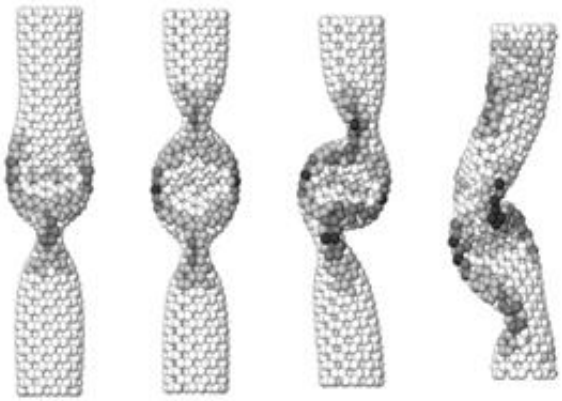

Figure 4-34: Simulations of buckling patterns of SWCNTs under axial compression (*Yakobson et al. 1996*)

For a cylindrical shell with applied compression at both ends, as shown in Figure 4.35, the buckling deformation is shown in Figure 4.36.

Figure 4-35: Sketch of cylindrical shell model under stretching

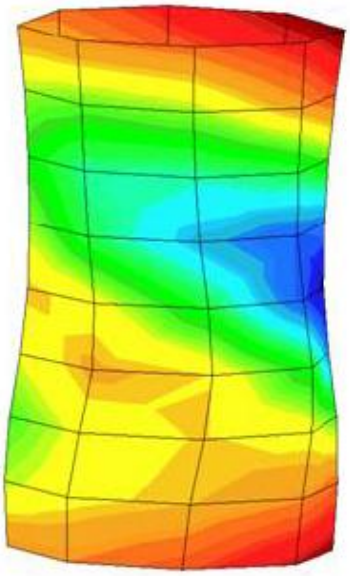

Figure 4-36: Deformation of cylindrical shell under compression (D=4.266nm; L=8nm)

Zigzag SWCNTs are studied, with the tube length fixed to L=16nm, and the tube diameter ranging from 0.939nm to 3.757nm. The critical bucking strain is captured via a force-strain relationship as shown in Figure 4.37. The same method is applied to capture the critical strains for SWCNTs with length L=16nm as listed in Table 4.4 and plotted out in Figure 4.38. It is shown that the critical buckling strain decreases when the tube diameter increases for a fixed length, but the differences are not significant.

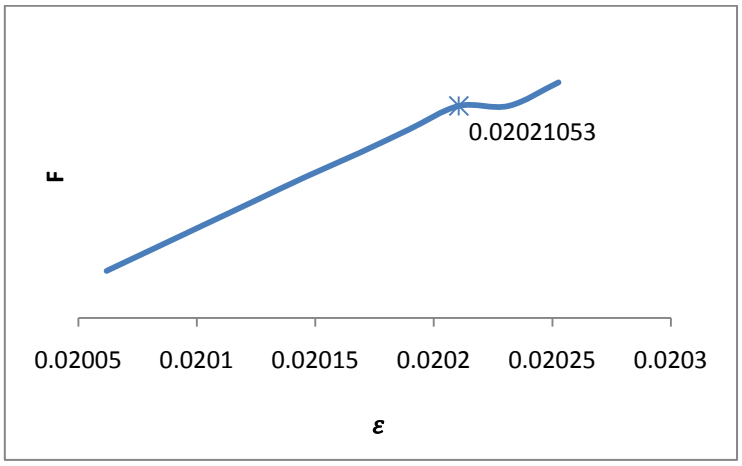

(a) Force-strain relationship of cylindrical shell under compression (D=3.288nm; L=16nm)

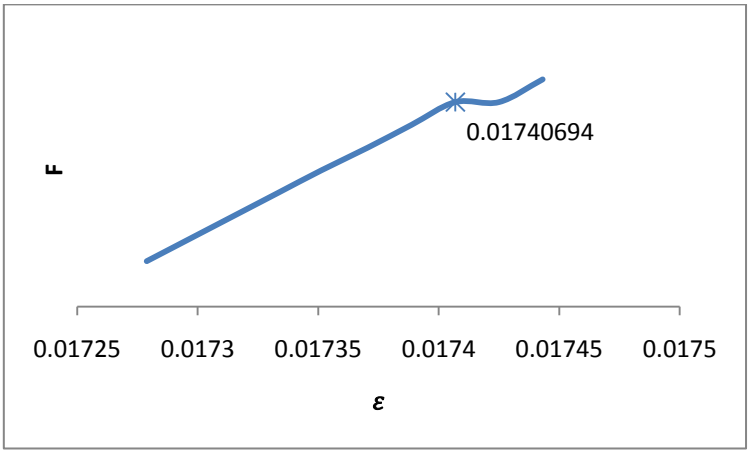

(b) Force-strain relationship of cylindrical shell under compression (D=3.757nm; L=16nm)

Figure 4-37: Force-strain relationship of cylindrical shell under compression with various tube diameters

Table 4-4: Critical strains for zigzag SWCNTs with different tube diameters

Diameter (nm)	0.939	1.409	1.879	2.348	2.818	3.288	3.757
Critical strain	0.0417	0.0334	0.0286	0.0259	0.0231	0.0202	0.0174

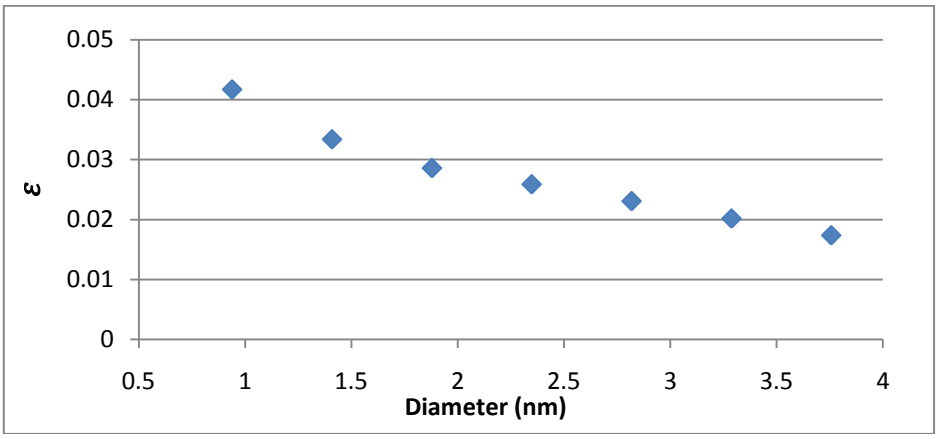

Figure 4-38: Critical strains of zigzag SWCNTs under compression with fixed length

Variations of critical strain with respect to tube diameter are compared in Figure 4.39 with results from three other authors all of which gained from atomistic simulations. While *Wang et al.* (*2005*) fixed the tube length to 10.1 nm, *Zhou et al.* (*2007*) fixed the tube length to 11.0 nm. Their specimens were also studied with different chiralities. Differences in tube lengths and chiralities may be the cause of the differences in critical strains.

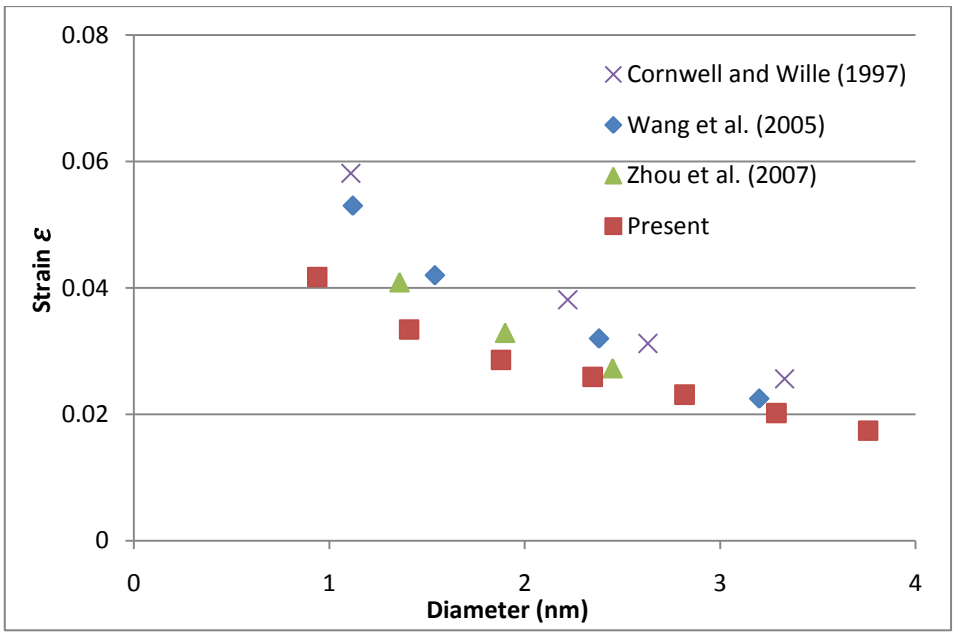

Figure 4-39: Comparison of variation of critical strains with respect to tube diameter

Second sets of zigzag SWCNTs are studied with respect to the aspect ratio *L/D*, by fixing the tube diameter to *D*=1.409nm with the tube length ranging from 8nm to 40nm. The critical bucking strain is captured from the force strain relationship as shown in Figure 4.40. It is shown that the curve of the force-strain relationship here varies from what is shown in Figure 4.36, where the aspect ratio is relatively small. Apparently after a certain aspect ratio, the force-strain relationship decreases beyond the critical strain, i.e. the tube is less stiff. Critical strains for SWCNTs with diameter *D*=1.409nm are listed in Table 4.5.

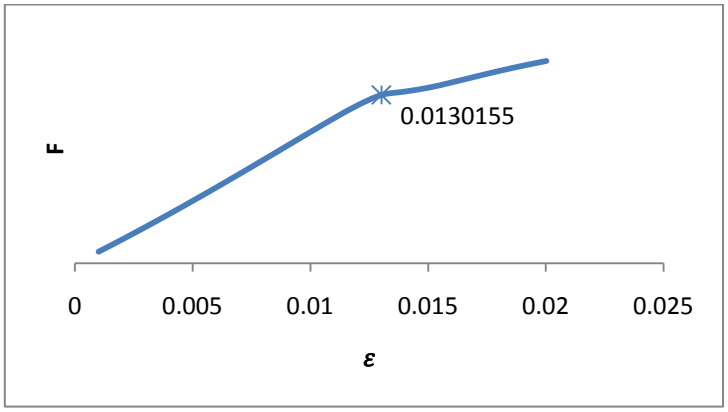

(a) Force-strain relationship of cylindrical shell under compression (D=1.409nm; L=32nm)

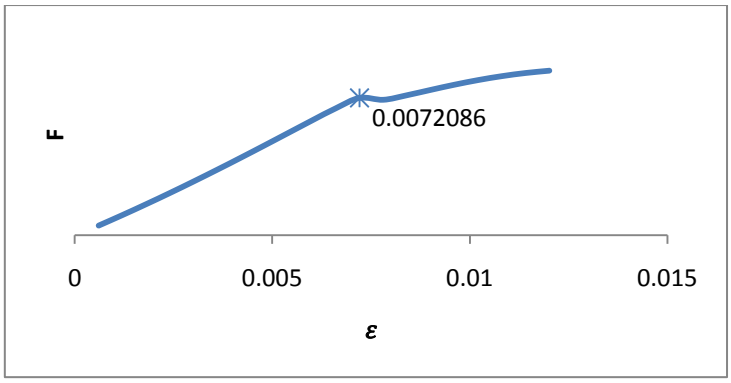

(b) Force-strain relationship of cylindrical shell under compression (D=1.409nm; L=40nm)

Figure 4-40: Force-strain relationship of cylindrical shell under compression with various tube lengths

Table 4-5: Critical strains for zigzag SWCNTs with different aspect ratio

Tube length (nm)	8	16	24	32	40
Aspect ratio	5.68	11.36	17.03	22.71	28.39
Critical strain	0.0556	0.0334	0.0220	0.0130	0.0072

Batra and Sears (*2007*) applied molecular mechanics to predict critical buckling strains for zigzag SWCNTs with tube diameter D=1.19nm, and the tube lengths changing from 10.12 nm to 24.51nm. *Zhang et al.* (*2009*) assessed nonlocal beam and shell models in predicting buckling strains of SWCNTs with tube diameter D=0.94nm, and tube lengths changing from 2.8 nm to 30nm. The results for critical buckling strains with respect to aspect ratios of SWCNTs together with comparisons with results from two authors mentioned above are presented in Figure 4.41. The results obtained here are in good agreements with the literature, and it is shown that the critical buckling strain decreases when the tube length increases with a fixed tube diameter for SWCNTs.

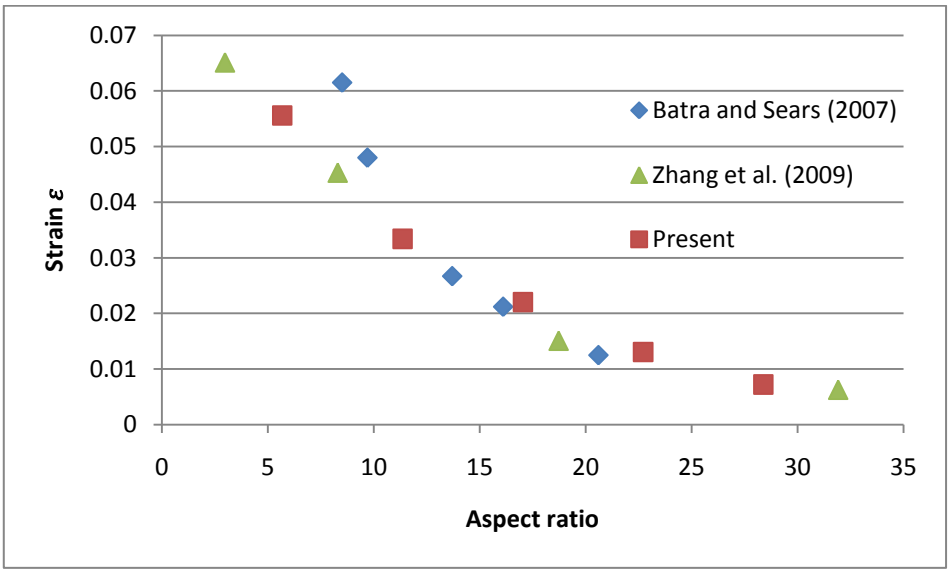

Figure 4-41: Comparison of variation of critical strains with respect to aspect ratio

It is observed that when the tube aspect ratio becomes larger, modelled SWCNT buckles sideways under axial compression rather than the buckling pattern in Figure 4.36. Buckling deformations for slender SWCNTs are simulated as shown in Figure 4.42, which shows the bending deformations. *Liew et al.* (*2006*) performed molecular dynamics approach and simulated the deformations for SWCNT bundle under axial compression as shown in Figure 4.43, as well as proved in this research that buckling under compression should present bending deformations for slender SWCNTs.

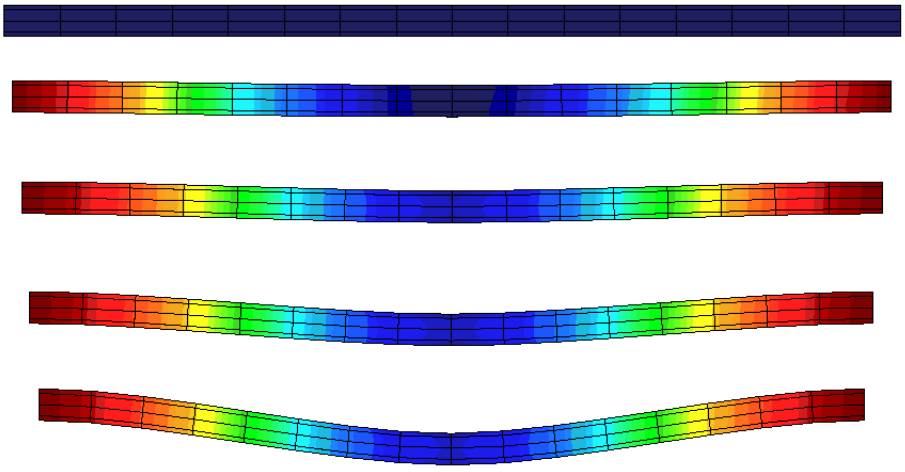

Figure 4-42: Deformation of cylindrical shell under compression (D=1.409nm; L=40nm)

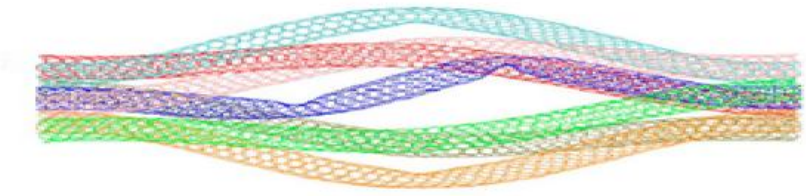

Figure 4-43: Bending deformations of SWCNT bundle under axial compression (*Liew et al. 2006*)

Zhang et al. (*2009*) applied molecular dynamics (MD) and simulated three types of buckling modes depending on the aspect ratios of SWCNTs, as shown in Figure 4.44 (a). In this research three similar results are obtained with similar aspect ratios for SWCNTs, as shown in Figure 4.44 (b). The results present a shell-like buckling mode when the aspect ratio *L/D* is small, a beam-like bending buckling mode when aspect ratio is large, and a shell-beam mixed buckling mode when the aspect ratios are in between certain range. Our results are in good agreements with results from *Zhang et al.* (*2009*).

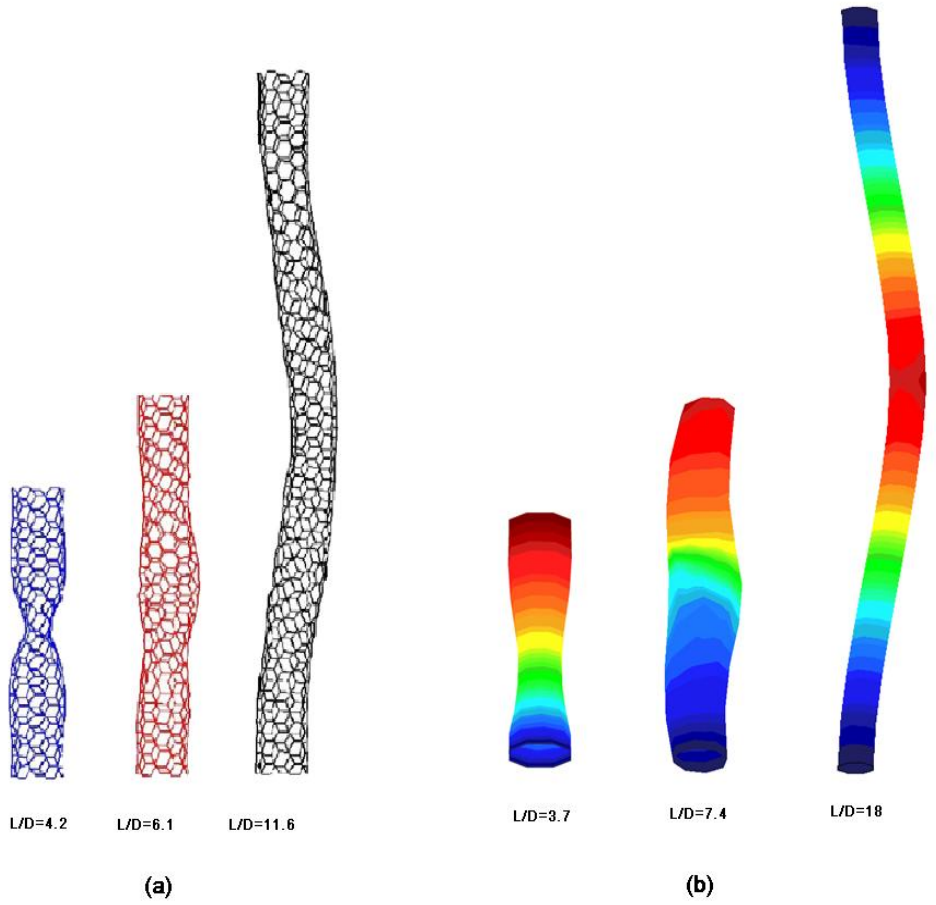

Figure 4-44: Three types of buckling modes of SWCNTs under axial compression depending on the aspect ratios (a) results from *Zhang et al.* (*2009*) (b) present results

4.6 Cylindrical shell model: twisting

A cylindrical shell under torsion with a zigzag SWCNT and external torques at both ends, as shown in Figure 4.45, is examined next. Twisting deformations with different twisting angles are shown in Figure 4.46. The relationship between the external torque and the twisting angle is drawn in Figure 4.47.

Figure 4-45: Sketch of cylindrical shell model under torsion

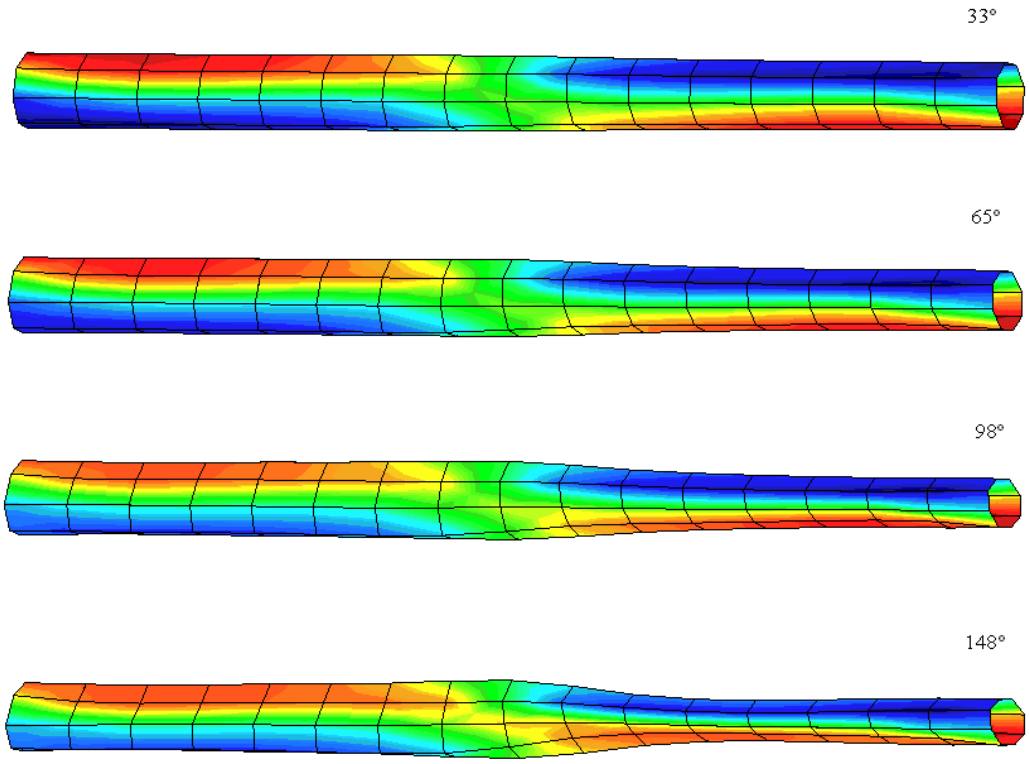

Figure 4-46: Deformations of cylindrical shell model under torsion

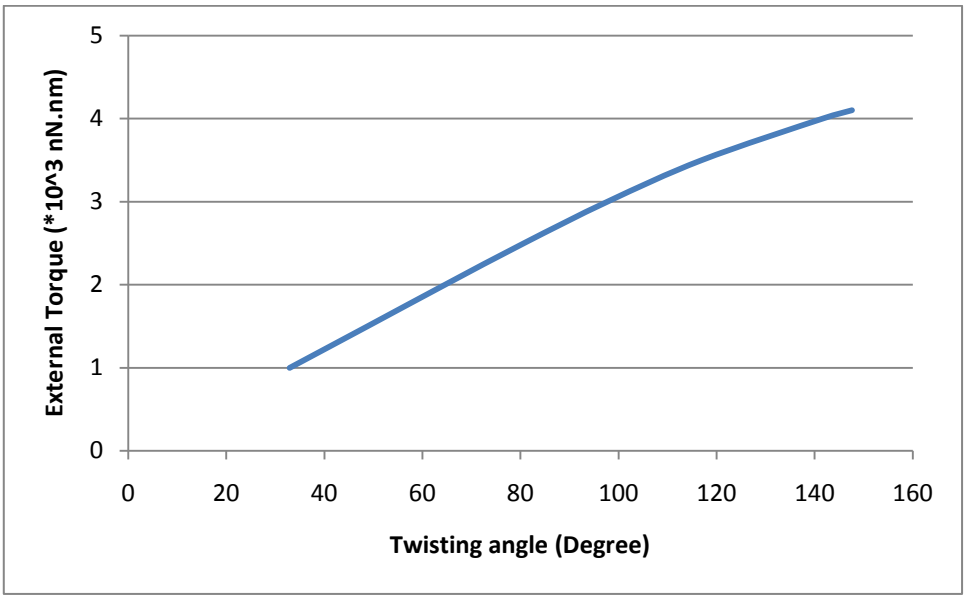

Figure 4-47: Relationship of external torque and twisting angle

As is shown in Figure 4.47, a linear relationship is obtained between the external torque moment and the twisting angle when the twisting angle is small, it becomes a non-linear curve after about 100 °.

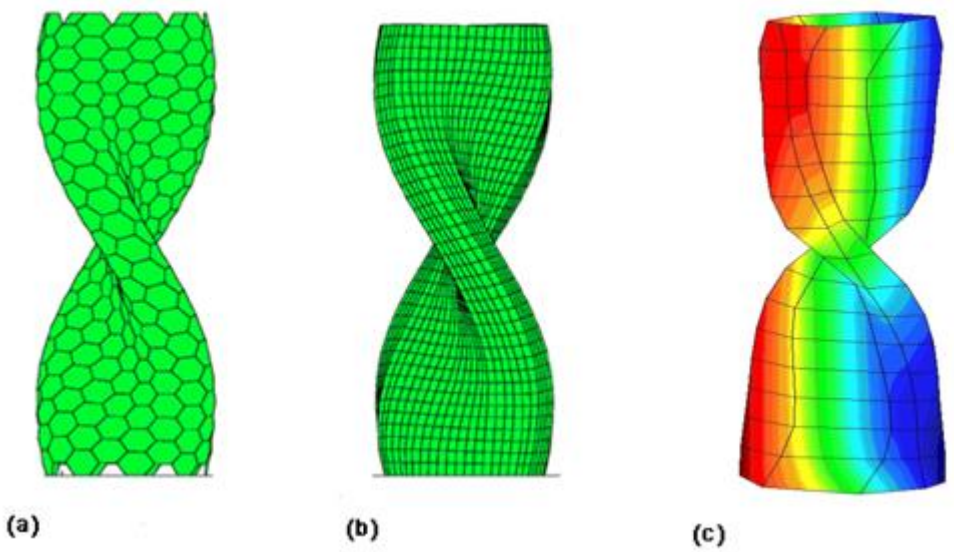

Figure 4-48: (a) atomistic simulation and (b) local Chauchy-Born rule result of SWCNT under twisting (*Yang and E, 2006*) (c) present result

Yang and E (*2006*) applied local Cauchy-Born rule to simulate SWCNT under twisting and compared the result with one from atomistic simulation as shown in Figure 4.48 (a) and (b). With the same dimension and twisting angle studied, which is a (9,9) armchair SWCNT with tube length L=5nm, and twisting angle θ=50°, our result from the Cosserat surface shell theory is shown in Figure 4.48 (c), where it is shown that even with coarse mesh of finite elements, Cosserat surface-based shell theory can produce reasonable results.

However, since van der Waals forces have not been included in the potential form, deformations of modelled SWCNT under torsion beyond 148° could not be captured, because the up and bottom surfaces are twisting towards each other, in which case, the atoms are close enough and their interactions contribute to the total energy that cannot be neglected, but they are not neighbours at the reference configuration whose interactions are not described by bonded energies. Thus, for large twisting angle deformations, as well as for severe buckling deformations and severe bending deformations, when two surfaces deform close to each other, van der Waals forces have to be considered in the potential.

Chapter 5

Conclusions and Discussions

5.1 Summary and conclusions

This research has presented a continuum and atomistic mixing approach to study the mechanical properties of SWCNTs. Because of the hollow cylindrical shell structure of SWCNT, it can be modelled as a thin shell, thus Cosserat surface as a shell model is applied in this research to compute and simulate the mechanical properties of SWCNTs, for the independent rotation tensor can describe the rotation field at a micro-level, which as well accounts for a hypothetical curvature of the deformed surface going beyond the standard Cauchy-Born rule.

Two sets of models are built in this research. As a tool, an atomic chain, which consists of a series of atoms in a chain, is modelled as a Cosserat curve and studied through a one-dimensional reduced Cosserat curve theory. For SWCNT,

modelled as a Cosserat surface, the mechanical properties have been studied. Cauchy-Born rule is applied to link the deformation of the lattice vector at an atomistic level to the tangent space of the deformation of the system at a continuum level.

By incorporating the potential form, the stress field and modulus field can be derived as the first and second derivatives of the potential over the displacement and rotation fields. For the atomic chain model, interatomic potentials are defined by a force field, which takes into account bond stretching, bond angle bending and bond torsion energies. For SWCNT, sophisticated second generation of Brenner potential is chosen, which contains bond stretching and bond angles as well.

Implementation of the discretization in a finite element approach is accomplished. The stress fields and the modulus fields are calculated via an iteration procedure where the displacement and rotation fields are updated. The rotation field is path-independent updated.

The deformation of an atomic chain under dynamic forces is simulated. Simulations of the atomic chain model in torsion is also presented, which shows a vibration mode after vertical instant disturbance, and coiling up mode after horizontal push. The result matches atomistic simulation of CNTs under torsion by *Yakobson et al.* (*1996*). Simulation of cross section of SWCNTs under bending is carried on by an atomic ring model. The simulation matches the results for the deformations of a cross section of SWCNTs under bending from *Vodenitcharova and Zhang* (*2004*) and *Kutana and Giapis* (*2006*).

It is shown that the atomic chain model can be used to simulate some behaviour of SWCNTs, but only provides qualitative results so far. In order to apply atomic chain model in the use of studying mechanical properties of SWCNTs, the relation between the structure of the atomic chain and the structure of SWCNT need to be studied and built numerically, also the potential forms and parameters need to be modified to provide quantitatively accurate results. Despite of the fact that a lot of improvements need to be made for atomic chain models to have physical meanings, 1-D atomic chain as a Cosserat curve model presents a fine preparation for further use of Cosserat surface to model and simulate SWCNTs.

For the study of SWCNTs, configuration formulas are established in addition to introducing an inner displacement because of the non-centrosymmetric hexagonal structure of a carbon cell. The mechanical properties of SWCNTs are then predicted via the finite element method.

Young's modulus and Poisson ratio are predicted for a zigzag SWCNT. With tension method, an average tension rigidity of 320.5 N/m and an average Poisson ratio of 0.395 are obtained, which are in good agreement with the literature. By the bending method, the effective wall thickness of SWCNT is computed as 0.058nm, which leads to an average of Young's modulus being 5.526TPa.

For SWCNT under stretching, results are gained that Young's modulus is decreasing with the increase of tube diameter. By applying wall thickness as 0.34nm, Young's modulus is converging at 0.72TPa, by which the result of dependence of Young's modulus on tube diameter for zigzag SWCNTs is in good agreement with results from *Natsuki et al.* (*2003*), *Shen and Li* (*2004*) and

Parvaneh and Shariati (*2011*). And it is shown that Young's modulus of SWCNT with zigzag structure is slightly larger than that of the armchair one, which is agreed with the results from *Lei et al.* (*2011*).

SWCNTs under bending are simulated in three situations: one end fixed bending, two end fixed bending and two end simply supported bending. The results have shown that, as for the prediction of Young's modulus of SWCNT, bending methods have to be considered carefully, although one end fixed model can predict similar results with cylindrical shell under tension when the tube diameter is large enough, all three sets of bending models provide extremely large values of Young's modulus when the tube diameter is small, while the two end fixed model and the two end simply supported model provide values of Young's modulus towards zero when the tube diameter is large. Demonstration of non-local bending and local bending of SWCNTs are also presented.

SWCNTs under compression are simulated. Critical buckling strains have been captured by reading the force and strain relationship. The results show that, for a fixed tube length, critical buckling strain decreases with the tube diameter increasing. And for a fixed tube diameter, critical buckling strain decreases when the tube length increases. Results are in good agreement with the literature. Twisting deformations of SWCNTs are also simulated, and a non-linear behaviour after twisting angle of 100° is captured.

5.2 **Discussions and recommendations**

Shell models have been applied widely to model SWCNTs (*Tu and Ou-yang, 2002, Pantano et al. 2004, Arroyo and Belytschko, 2002, 2003, 2004*). But it is hard to define Young's modulus and shell thickness in a classical linear elastic shell theory, where the wall thickness has been calculated from 0.066nm to 0.34nm as demonstrated in Table 4.1. In this case, Cosserat surface presented a great advantage by avoiding the shell thickness as well as Young's modulus itself, but linking the tension and bending rigidities directly to interatomic potentials.

The link between atomistic deformations and continuum deformations is provided by the Cauchy-Born rule. However, the drawback of the Cauchy-Born rule for SWCNTs is that the deformation map maps the deformed lattice vector onto the tangent plane of the deformed surface, which does not matter for bulk material but has significant effects on a thin surface material such as SWCNTs, especially when a large curvature is involved. Therefore, modifications need to be made to the Cauchy-Born rule for its application to study SWCNTs, in which aspect, Cosserat surface as a shell model makes perfect compatibility with the standard Cauchy-Born rule, since in a Cosserat surface-based shell theory, a displacement field-independent rotation tensor is introduced that describes the curvature at each point of the surface, which relates the rotation field to the inner structure of the surface, i.e. at a micro-level. Therefore, the Cauchy-Born rule describes the tangent map, while the change of curvature of the deformed surface is captured by rotation tensor which describes the micro-level rotation map.

An ideal potential model should be able to accurately describe the interactions among atoms in a SWCNT. How accurate the empirical potentials are defined plays a very important role on how well the results come out, because different potential models, or even different sets of parameters in the potential form can lead to big differences in the results, which was also pointed out by *Wang et al.* (2006) and *Wu et al.* (2008).

In this research, we adopt interatomic potential forms based on a force field to describe potentials for the atomic chain, which is of advantage since the atomic chain model consists of a series of atoms, and so a force field defines all the interactions between atoms, except that the C-C bond atomic chain model has not been given a physical explanation, since C-C bonds have hexagonal structure in the SWCNT structure rather than a straight line. However, an atomic chain model presents various behaviours that are similar to SWCNT's behaviours, so if the relation between an atomic chain and SWCNT, or any other similar atomic structures, can be studied and constructed and if the potential forms can be reformulated, atomic chain models could be very handy for simulation of string-like nanostructures.

Cosserat surface as a shell model has been built to simulate SWCNTs. Second generation Brenner potential formulation is adopted. The first generation of Tersoff-Brenner potential has been applied widely by previous researchers, in most cases produced an opposite trend of the results, as shown in Figure 1.2 and Figure 1.4, and also as shown in results from *Arroyo and Belytschko* (*2004*), where Young's modulus of SWCNT increases with the tube diameter increasing and converging at around 0.69TPa. Second generation Brenner potential has not

been used as much, since the formulation is new and the adjustments make the potential forms much more complicated, and atoms from second layer in the neighbourhood are involved in the calculation. Extra potential terms which describe shear effects and atom spin effects are added to assure the non-singularity of the tangent modulus.

Most researches in recent years have applied atomistic potential forms from force field, and built C-C bonds as a beam, rod or spring, and built-in the constitutive law into commercial software, such as ANSYS or ABAQUS (*Avila and Lacerda, 2008*; *Dun et al. 2010*; *Shokrieh and Rafiee, 2010*; *Parvaneh and Shariati, 2011*). The results received in this research are in good agreement with the results from these atomistic simulations based on force field potentials. And the results of buckling patterns and twisting patterns are still in agreement with previous researchers who applied first generation Tersoff-Brenner potential forms, because the change of potential forms did affect the results of Young's modulus, but it didn't affect the bending, buckling and twisting patterns.

Young's modulus and Poisson ratio has been obtained from tension and bending methods for graphite sheet. Because the force displacement relationship Cosserat surface-based shell theory provides is non-linear, it is rather flexible and subjective to decide what value to go for to calculate Young's modulus of graphite sheet. Assume wall thickness is 0.34nm, if initial value is selected from the results of graphite sheet tension that leads to a Young's modulus of 0.706TPa. In this research, we go for the other method of selecting a changing point and an area around it to calculate an average value, in which case, it arrives an average Young's modulus of 0.943TPa for wall thickness 0.34nm, which is in good

agreement with the experimental results. But still, the definition of selected area is subjective and then the result may vary from time to time.

Therefore, we decide to use another method which is straight forward to calculate Young's modulus for SWCNTs modelled by cylindrical shells, where we adopt the equations from classical elastic beam theory which build a relation between external forces and the final deflection. In which way, results of Young's modulus for SWCNTs obtained from the tension model are still within the range, but results from the bending models become unreasonable. One end fixed bending model can still provide similar results with the tension model when tube diameter is large, while the two end fixed and the two end simply supported models result in a Young's modulus value towards zero when tube diameter becomes large. And all three sets of bending models produce extremely high values of Young's modulus when the tube diameter is small. All these errors might be caused by two reasons, either when the tube diameter is small enough that the size of tube diameter and the size of tube wall thickness is similar, in which case, shell theory cannot be applied anymore, or when the tube diameter is large enough that there is only deformations on the surface rather than the whole system, in which case, the equations from classical beam theory are not valid anymore. To sum up, by applying continuum theory in calculating properties of SWCNTs, the size effects have to be considered, and the assumptions have to be used carefully because they may not be valid anymore in some situations, even in elastic cases.

The whole calculation, except few cases, has been carried on by 8×8 element models, which includes 486 degrees of freedom for graphite sheet and only 432 degrees of freedom for cylindrical shell model, which already provide reasonable

results with good agreements with the literature. If the calculation is carried on by more elements, i.e. finer meshes, it should be able to catch more detailed information about the behaviour of SWCNTs.

Van der Waals force interactions have not been considered in either atomic chain model or cylindrical shell model, which contributes to the non-bonded energies in the total potential forms. It describes the interatomic reactions between two atoms that are not bonded within certain range in SWCNT case, which can normally be neglected when the bonded energies dominate the total energy, as is considered in this research. However, non-bonded energy cannot be ignored in the study of MWCNTs, as van der Waals forces contributes to the interactions between the layers of CNTs, in which case we need to add van der Waals force energy, which is normally described by Lennard-Jones potential, if we want to do further research about MWCNTs. Van der Waals force should also not be neglected when SWCNT is studied under severe deformation, like when the tube is under severe bending that two ends move towards each other, the atoms from two surfaces become close enough but bonded energy cannot define the interactions of the close non-bonded atoms which can only be described by van der Waals force, or when tube is under large torsion deformation, van der Waals force also needs to be included for the atoms on two close surfaces under twisting.

Future work will focus on:

1. Check the validation of the potential forms, possible modifications will be made to fit the potential in an atomistic level. Neglected terms need to be checked if they would make much differences for the results. Applications

of other empirical potentials will be used and compared to find an optimized solution.

2. Van der Waals force interactions should be considered based on Lennard-Jones 6-12 expressions, in order to study more complicated deformations of SWCNTs, or possibly MWCNTs. In this case, third and forth buckling patterns, severe local bending, and large angle twisting deformations for SWCNTs will then be simulated.
3. More elements with finer meshes need to be applied to provide more detailed information. Nine-node elements will be used to study tensile strength, buckling failure, fracture of CNTs, or other aspects involving stress concentrating.
4. Quantitative properties obtained from cylindrical shell models for CNTs will be used to calculate parameters in the potential forms for atomic chain model, in order to check if an easy 1-D Cosserat curve model can produce reasonable results in simulating CNTs' behaviours.

References

Ajayan, P. M., Zhou, O.Z. (2001) Applications of carbon nanotubes, *Carbon Nanotubes*, 80, 391-425.

Arroyo, M., Belytschko, T. (2002) An atomistic-based finite deformation membrane for single layer crystalline films. *Journal of the Mechanics and Physics of Solids*, 50, 1941-1977.

Arroyo, M., Belytschko, T. (2003) A finite deformation membrane based on inter-atomic potentials for the transverse mechanics of nanotubes. *Mechanics of Materials*, 35 (3-6), 193-215.

Arroyo, M., Belytschko, T. (2004) Finite crystal elasticity of carbon nanotubes based on the exponential Cauchy-Born rule. *Physical Review* B, 69:115415.

Arroyo, M., Belytschko, T. (2004) Finite element methods for the non-linear mechanics of crystalline sheets and nanotubes, *International Journal for Numerical Methods in Engineering*, 59, 419-456.

Avila, A.F., Lacerda, G.S. (2008) Molecular mechanics applied to single-walled carbon nanotubes. *Materials Research*, Vol. 11, No. 3, 325-333.

Avouris, P. (2002) Carbon Nanotube Electronics. *Chemical Physics*, 281, 429-445.

Bao, W.X., Zhu, C.C., Cui, W.Z. (2004) Simulation of Young's modulus of single-walled carbon nanotubes by molecular dynamics. *Physica B: Condensed Matter*, 352 (1-4), 156-163.

Batra, R.C., Sears, A. (2007) Continuum models of multi-walled carbon nanotubes. *Int. J. Solids Struct.*, 44, 7577-7596.

Baughman, R. H., Zakhidov, A. A., Heer, W. A. (2002) Carbon nanotubes-the route toward applications. *Science*, 297, 787-792.

Belytschko, T., Xiao, S.P., Schatz, G.C., Ruoff, R.S. (2002) Atomistic simulations of nanotube fracture, *Phys Rev* B, 65, 235430.

Bertoni, G., Calmels, L. (2006) First-principles calculation of the electronic structure and energy loss near edge spectra of chiral carbon nanotubes. *Micron*, 37 (5), 486-491.

Brenner, D.W. (1989) Tersoff-type Potentials for Carbon, Hydrogen and Oxygen", *Mat. Res. Soc. Symp.* Proc. 141, 59-64.

Brenner, D.W., Shenderova, O.A., Harrison, J.A., Stuart, S.J., Ni, B., Sinnott, S.B. (2002) A second-generation reactive empirical bond order (REBO) potential energy expression for hydrocarbons. *J. Phys.: Condens. Matter* 14, 783–802.

Buongiorno-Nardelli, M., Yakobson, B.I., Bernhold, J. (1998) Mechanism of strain release in carbon nanotubes. *Phys. Rev*. Lett. 81, 4656; *Phys. Rev*. B. 57, 4277.

Cai, J., Bie, R. F., Tan, X. M., Lu, C. (2004) Application of the tight-binding method to the elastic modulus of C60 and carbon nanotube. *Physica B: Condensed Matter*, 344 (1-4), 99-102.

Chandraseker, K., Mukherjee, S., Mukherjee, Y. X. (2006) Modifications to the Cauchy–Born rule: Applications in the deformation of single-walled carbon nanotubes. *International Journal of Solids and Structures*, 43 (22-23), 7128-7144.

Chang, T., Gao, H. (2003) Size-dependent elastic properties of a single-walled carbon nanotube via a molecular mechanics model. *Journal of the Mechanics and Physics of Solids*, 51, 1059-1074.

Cornwell, C.F., Wille, L.T. (1997) Proposed growth mechanism of single-walled carbon nanotubes. *Chemical Physics Letters* 278, 262-266.

Dai, H., Hafner, J. H., Rinzler, A. G., Colbert, D. T., Smalley, R. E.(1996) Nanotubes as nanoprobes in scanning probe microscopy. *Nature*, 384, 147-150.

Damnjanovic, M., Milosevic, I., Vukovic, T., Sredanovic, R. (1999) Full Symmetry, Optical Activity and Potentials of Single- and Multi-wall Nanotubes, *Phys. Rev*. B. 60, 2728-2739.

Dresselhaus, M.S., Dresselhaus, G., Eklund, P. C. (1996) Science of Fullerenes and Carbon Nanotubes. *Academic Press Inc.*

Duan, W. H., Wang, Q., Wang, Q., Liew, K. (2010) Modelling the Instability of Carbon Nanotubes: From Continuum Mechanics to Molecular Dynamics. *Journal of Nanotechnology in Engineering and Medicine*. Vol. 1, 011001-10.

Endo, M., Hayashi, T., Kim, Y.A., Muramatsu, H. (2006) Development and application of carbon nanotubes. *Japanese Journal of Applied Physics*, 45 (6A), 4883–4892.

Gao, X. L., Li, K. (2003) Finite deformation continuum model for single-walled carbon nanotubes. *International Journal of Solids and Structures*, 40(26), 7329-7337.

Govindjee, S., Sackman, J. L. (1999) On the use of continuum mechanics to estimate the properties of nanotubes. *Solid State Communications*, 110 (4), 227-230.

Guo, X., Wang, J. B., Zhang, H.W. (2006) Mechanical properties of single-walled carbon nanotubes based on higher order Cauchy–Born rule. *International Journal of Solids and Structures*, 43 (5), 1276-1290.

Haefner, J., Sachse, F.B., Sansour, C., Seeman, G. (2002) Hyperelastic description of elastomechanic properties of the heart: A new material law and its application. *Biomedical Engineering -Supplement*, 47(6), 770-773.

Hall, B.C. (2003) Lie Groups, Lie Algebras, and Representations: An Elementary Introduction, *Springer*, ISBN 0-387-40122-9.

Harris, P. J. F. (2009) Carbon Nanotube Science: Synthesis, Properties and Applications. *Cambridge University Press*.

He, X. Q., Kitipornchai, S., Wang, C. M., Liew, K. M. (2005) Modelling of van der Waals force for infinitesimal deformation of multi-walled carbon nanotubes treated as cylindrical shells. *International Journal of Solids and Structures*, 42 (23), 6032-6047.

He, X. Q., Kitipornchai, S., Liew, S. (2005) Buckling analysis of multi-walled carbon nanotubes: a continuum model accounting for van der Waals interaction. *Journal of the Mechanics and Physics of Solids*, 53 (2), 303-326.

Hernandez, E., Goze, C., Bernier, P. Rubio, A. (1998) Elastic properties of C and BxCyNz Composite Nanotubes. *Phys. Rev. Lett*. 80, 4502–4505.

Hertel, T., Martel, R., Avouris, P. (1998) Manipulation of carbon nanotubes and their Interaction with Surfaces. *J. Phys. Chem. B* 102, 910-915.

Hone, J., Llaguno, M. C., Biercuk, M. J., Johnson, A. T., Batlogg, B., Benes, Z., Fischer, J. E. (2002) Thermal properties of carbon nanotubes and nanotube-based materials. *Appl. Phys*. A, 74, 339–343.

Huang, Y., Wu, J., Hwang, K. C. (2006) Thickness of graphene and single-wall carbon nanotubes. *Physical Review* B, 74, 245413.

Huhtala, M., Kuronen, A., Kaski, K. (2002) Carbon nanotubes under bending strain. *Mat. Res. Soc. Symp. Proc*. Vol. 706.

Iijima, S. (1991) Helical microtubules of graphitic carbon. Nature 354, 56–58.

Ito, T., Nishidate, K., Baba, M., Hasegawa, M. (2002) First principles calculations for electronic band structure of single-walled carbon nanotube under uniaxial strain. *Surface Science*, 514 (1-3), 222-226.

Jin, Y., Yuan, F. G. (2003) Simulation of elastic properties of single-walled carbon nanotubes. *Compos. Sci. Technol*. 63, 1507.

Justo, J. F., Bazant, M. Z., Kaxiras, E., Bulatov, V. V., Yip, S. (1998) Interatomic potential for Silicon defects and disordered phases. *Physical review* B, 58 (5), 2539-2550.

Kollman, F. G., Sansour, C. (1999) Theory and numerics of viscoplastic shells - a review. *Constitutive laws for engineering materials*, 4, 20-23.

Krishnan, A., Dujardin, E., Ebbesen, T.W., Yianilos, P.N., Treacy, M.M. (1998) Young's modulus of single-walled nanotubes. *Phys. Rev.* B 58, 14013–14019.

Kutana, A., Giapis, K.P. (2006) A transient deformation regime in bending of single-walled carbon nanotubes, *Phys. Rev. Lett*. 97, 245501.

Leamy, M. J., Chung, P. W., Namburu, R. (2003) On an exact mapping and a higher-order Born rule for use in analyzing graphene carbon nanotubes. *Proceedings of the 11th Annual ARL-USMA Technical Symposium*.

Lei, X., Natsuki, T., Shi, J. Ni, Q. Q. (2011) Analysis of carbon nanotubes on the mechanical properties at atomic scale. *Journal of Nanomaterials*. 805313,10.

Li, C., Chou, T. (2003) A structural mechanics approach for the analysis of carbon nanotubes. *International Journal of Solids and Structures*, 40, 2487–2499.

Liew, K.M., He, X.Q., Wong, C.H. (2004) On the study of elastic and plastic properties of multi-walled carbon nanotubes under axial tension using molecular dynamics simulation. *Acta Materialia*, 52 (9), 2521-2527.

Liew, K.M., Wong, C.H., Tan, M.J. (2006) Twisting effects of carbon nanotube bundles subjected to axial compression and tension. *Jounal of Applied Physics*, 99,114312.

Lindsay, L., Broido, D.A. (2010) Optimized Tersoff and Brenner empirical potential parameters for lattice dynamics and phonon thermal transport in carbon nanotubes and graphene *Phys. Rev*. B 81, 205441.

Liu, J. Z., Zheng, Q. S., Wang, L. F., Jiang, Q. (2005) Mechanical properties of single-walled carbon nanotube bundles as bulk materials. *Journal of the Mechanics and Physics of Solids*, 53 (1), 123-142.

Lourie, O., Cox, D. M., Wagner, H. D. (1998) Buckling and collapse of embedded carbon nanotubes. *Phys. Rev. Lett*. 81, 1638–1641.

Lu, J.P. (1997) Elastic properties of carbon nanotubes and nanoropes. *Physical Review Letters*, 79(7), 1297-300.

Lu, Q., Bhattacharya, B. (2005) The role of atomistic simulations in probing the small-scale aspects of fracture - a case study on a single-walled carbon nanotube. *Engineering Fracture Mechanics*, 72, (13), 2037-2071.

Meo, M., Rossi, M. (2006) Tensile failure prediction of single wall carbon nanotube. *Engineering Fracture Mechanics*, 73 (17), 2589-2599.

Meo, M., Rossi, M. (2006) Prediction of Young's modulus of single wall carbon nanotubes by molecular-mechanics based finite element modelling. *Composites Science and Technology*, 66, 1597–1605.

Natsuki, T., Endo, M. (2004) Stress simulation of carbon nanotubes in tension and compression. *Carbon*, 42 (11), 2147-2151.

Natsuki, T., Tantrakarn, K., Endo, M. (2004) Prediction of elastic properties for single-walled carbon nanotubes. *Carbon*, 42 (1), 39-45.

Niyogi, S., Hamon, M. A., Hu, H., Zhao, B., Bhowmik, P., Sen, R., Itkis, M. E., Haddon, R. C. (2002) Chemistry of single-walled carbon nanotubes. *Accounts of Chemical Research*. 35 (12), 1105-1113.

Odegard, G.M., Gates, T.S., Nicholson, L.M., Wise, K.E. (2002) Equivalent continuum modelling with application to carbon nanotubes. *NASA/TM*, 211454.

Omata, Y., Yamagami, Y., Tadano, K., Miyake, T., Saito, S. (2005) Nanotube nanoscience: A molecular-dynamics study. *Physica E: Low-dimensional Systems and Nanostructures*, 29 (3-4), 454-468.

Pantano, A., Parks, D. M., Boyce, M. C. (2004) Mechanics of deformation of single- and multi-wall carbon nanotubes. *Journal of the Mechanics and Physics of Solids*, 52 (4), 789-821.

Parvaneh, V., Shariati, M. (2011) Effect of defects and loading on prediction of Young's modulus of SWCNTs. *Acta Mech*, 216, 281–289.

Poncharal, P., Wang, Z. L., Ugarte, D., deHeer, W. A. (1999) Electrostatic deflections and electromechanical resonances of carbon nanotubes, *Science*, 283, 1513–1516.

Rappi, A.K., Casewit, C.J., Colwell, K.S. Goddard, W.A., Skid, W.M. (1992) UFF, a full periodic table force field for molecular mechanics and molecular dynamics simulations. *J. Am. Chem. Soc.*, 114, 10024-10035.

Salvetat, J., Bonard, J., Thomson, N.H., Kulik, A.J., Forro, L., Benoit, W., Zuppiroli, L. (1999) Mechanical properties of carbon nanotubes. *Appl. Phys.* A 69, 255–260.

Sansour, C., Bednarczyk, H. (1995) The Cosserat surface as a shell model, theory and finite-element formulation. *Computer Methods in Applied Mechanics and Engineering*, 120 (1-2), 1-32.

Sansour, C., Kollmann, F.G. (1998) Large viscoplastic deformations of shells-Theory and finite element formulation. *Computational Mechanics*, 21, 512-525.

Sansour, C., Wagner, W., (2003) Multiplicative updating of the rotation tensor in the finite element analysis of rods and shells - a path independent approach. *Computational Mechanics,* 31(1-2), 153-162.

Sansour, C. (2006) On anisotropic formulations for finite strain plasticity and the plastic spin. *Oberwolfach reports*, 3(1), 242.

Sansour, C., Skatulla, S. (2008) Essential boundary conditions in meshfree methods via a modified variational principle. Applications to shell

computations, *Computer Assisted Mechanics and Engineering Sciences*, 15: 123-142.

Shokrieh, M.M., Rafiee, R. (2010) Prediction of Young's modulus of graphene sheets and carbon nanotubes using nano-scale continuum mechanics approach. *Materials and Design*, 31,790–795.

Sinnott, S. B., Shenderova, O. A., White, C. T., Brenner, D. W. (1998) Mechanical properties of nanotubule fibers and composites determined from theoretical calculations and simulations. *Carbon*, 36 (1-2), 1-9.

Sun, X.K., Zhao, W.M. (2005) Prediction of stiffness and strength of single-walled carbon nanotubes by molecular-mechanics based finite element approach. *Materials Science and Engineering A*, 390 (1-2), 366-371.

Tersoff, J. (1988) Empirical Interatomic Potential for Carbon, with Application to Amorphous Carbon, *Phys. Rev*. Lett. 61, 2879-2882.

Treacy, M. M. J., Ebbesen, T. W., Gibson, J. M. (1996) Exceptionally high Young's modulus observed for individual carbon nanotubes, *Nature*, 381, 678.

Tserpes, K. I., Papanikos, P. (2005) Finite element modelling of single-walled carbon nanotubes. *Composites*: Part B 36, 468–477.

Tu, Z., Ou-Yang, Z. (2002) Single-walled and multiwalled carbon nanotubes viewed as elastic tubes with the effective Young's moduli dependent on layer number, *Phys. Rev.* B 65 , p. 233407.

Umeno, Y., Kitamura, T., Kushima, A. (2004) Theoretical analysis on electronic properties of zigzag-type single-walled carbon nanotubes under radial deformation. *Computational Materials Science*, 30 (3-4), 283-287.

Vodenitcharova, T., Zhang, L. C. (2004) Mechanism of bending with kinking of a single-walled carbon nanotube. *Physical Review*, B 69, 115410.

Wang, J.B., Guo, X., Zhang, H.W., Wang, L., Liao, J.B. 1 (2006) Energy and mechanical properties of single-walled carbon nanotubes predicted using the higher order Cauchy-Born rule. *Physical Review* B, 73, 115428.

Wang, Q., Varadan, V. K., Quek, S. T. 2 (2006) Small scale effect on elastic buckling of carbon nanotubes with nonlocal continuum models. *Physics Letters A*, 357 (2), 130-135.

Wang, Y., Wang, X. X., Ni, X. G., Wu, H. A. (2005) Simulation of the Elastic Response and the Buckling Modes of Single-Walled Carbon Nanotubes. *Comput. Mater. Sci*., 32, 141–146.

Wong, E.W., Sheehan, P.E., Lieber, C.M. (1997) Nanobeam mechanics: elasticity, strength, and toughness of nanorods and nanotubes. *Science* 277, 1971–1975.

Wu, J., Hwang, K.C., Song, J., Huang, Y. (2008) A finite deformation shell theory for carbon nanotubes based on the interatomic potential—part II: instability analysis. *Jounal of Applied Mechanics*. Vol. 75, 061007.

Wu, Y. D., Zhang, X. C., Leung, A. Y. T., Zhong, W. F. (2006) An energy-equivalent model on studying the mechanical properties of single-walled carbon nanotubes. *Thin-Walled Structures*, 44 (6), 667-676.

Yakobson, B. I., Brabec, C. J., Bernholc, J. (1996) Nanomechanics of carbon tubes: Instabilities beyond the linear response. *Phys. Rev. Lett.,* 76, 2511.

Yakobson, B. I., Brabec, C. J., Bernholc, J. (1996) Structural mechanics of carbon nanotubes: from continuum elasticity to atomistic fracture. *J. Computer-Aided Materials Design*, 3, 173.

Yakobson B.I., Campbell M.P., Brabec C.J., Bernholc, J. (1997) High strain rate fracture and C-chain unraveling in carbon nanotubes. *Computational material Science*, 8, 341-348.

Yang, J.Z., E, W. (2006) Generalized Cauchy-Born rules for elastic deformation of sheets, plates, and rods: Derivation of continuum models from atomistic models. *Physical Review*, B, 74, 184110.

Yang, H. K., Wang, X. (2007) Torsional buckling of multi-wall carbon nanotubes embedded in an elastic medium. *Composite Structures*, 77 (2), 182-192.

Zhang, P., Huang, Y., Geubelle, P. H., Klein, P. A., Hwang, K. C. (2002) The elastic modulus of single-wall carbon nanotubes: a continuum analysis incorporating interatomic potentials. *International Journal of Solids and Structures*, 39 (13-14), 3893-3906.

Zhang, P., Jiang, H., Huang, Y., Geubelle, P. H., Hwang, K. C. (2004) An atomistic-based continuum theory for carbon nanotubes: analysis of fracture nucleation. *Journal of the Mechanics and Physics of Solids*, 52 (5), 977-998.

Zhang, S. L., Mielke, S. L., Khare, R., Troya, D., Ruoff, R. S., Schatz, G. C., Belytschko, T. (2005) Mechanics of defects in carbon nanotubes: Atomistic and multiscale simulations. *Physical Review* B, 71, 115403(12).

Zhang, H.W., Wang, J.B., Guo, X. (2005) Predicting the elastic properties of single-walled carbon nanotubes. *Journal of the Mechanics and Physics of Solids.* 53, 1929-1950.

Zhang, Y.Y., Wang, C. M., Tan, V. B. C. (2006) Effect of omitting terms involving tube radii difference in shell models on buckling solutions of DWNTs. *Computational Materials Science*, 37 (4), 578-581.

Zhang, Y.Y., Wang, C.M., Duan, W.H., Xiang, Y. Zong, Z. (2009) Assessment of continuum mechanics models in predicting buckling strains of single-walled carbon nanotubes. *Nanotechnology*, 20, 395707-8.

Zhou, L., Zhu, B.E., Pan, Z.Y., Wang, Y.X., Zhu, J. (2007) Reduction of the buckling strength of carbon nanotubes resulting from encapsulation of C60 fullerenes. *Nanotechnology*, Vol. 18, 27, 275709.

Zhou, X., Chen, H., Zhou, J. J., Ou-Yang, Z. C. (2001) The structure relaxation of carbon nanotube. *Physica B: Condensed Matter*, 304 (1-4), 86-90.

Zhou, X., Zhou, J. J., Ou-Yang, Z. C. (2000) Strain energy and Young's modulus of single-wall carbon nanotubes calculated from electronic energy-band theory, *Phys. Rev.* B 62, p. 13692.

Appendix

A. Algorithm Expansion

Rotation tensor is expressed as

$$\boldsymbol{R} = \mathbf{1} + \frac{\sin|\boldsymbol{\omega}|}{|\boldsymbol{\omega}|}\boldsymbol{\Omega} + \frac{1-\cos|\boldsymbol{\omega}|}{|\boldsymbol{\omega}|^2}\boldsymbol{\Omega}^2 \qquad (A.1)$$

and the deformation gradient is in the form of

$$\boldsymbol{F} = (\boldsymbol{G}_\alpha + \boldsymbol{u}_{,\alpha}) \otimes \boldsymbol{G}^\alpha \qquad (A.2)$$

And then the strain tensor can be obtained from

$$\boldsymbol{U} = \boldsymbol{R}^{\boldsymbol{T}}\boldsymbol{F} = \boldsymbol{G}_\alpha \otimes \boldsymbol{G}^\alpha + \frac{\sin|\boldsymbol{\omega}|}{|\boldsymbol{\omega}|}\boldsymbol{\Omega}\boldsymbol{G}_\alpha \otimes \boldsymbol{G}^\alpha + \frac{1-\cos|\boldsymbol{\omega}|}{|\boldsymbol{\omega}|^2}\boldsymbol{\Omega}^2\boldsymbol{G}_\alpha \otimes \boldsymbol{G}^\alpha + \boldsymbol{u}_{,\alpha}$$

$$\otimes \boldsymbol{G}^\alpha + \frac{\sin|\boldsymbol{\omega}|}{|\boldsymbol{\omega}|}\boldsymbol{\Omega}\boldsymbol{u}_{,\alpha} \otimes \boldsymbol{G}^\alpha + \frac{1-\cos|\boldsymbol{\omega}|}{|\boldsymbol{\omega}|^2}\boldsymbol{\Omega}^2\boldsymbol{u}_{,\alpha} \otimes \boldsymbol{G}^\alpha \qquad (A.3)$$

when displacement field and rotation field is defined in Cartesian co-ordinates

$$\boldsymbol{u} = u_i\boldsymbol{e}_i,\ \boldsymbol{\omega} = \omega_i\boldsymbol{e}_i \qquad (A.4)$$

And bring in mind the relation of

$$\boldsymbol{\Omega} = \boldsymbol{\omega} \times \mathbf{1} = \omega_j e_{ijk}\boldsymbol{e}_k$$

$$\boldsymbol{\Omega}^2 = \boldsymbol{\omega} \times (\boldsymbol{\omega} \times \mathbf{1}) = (\omega_i\omega_k - \omega_j\omega_j\delta_{ik}) \qquad (A.5)$$

The relation between base system and Cartesian system is

$$c_{\alpha i} = \boldsymbol{G}_\alpha \cdot \boldsymbol{e}_i \ , \qquad c_{3i} = \boldsymbol{N} \cdot \boldsymbol{e}_i$$

$$\boldsymbol{G}_\alpha = c_{i\alpha}\boldsymbol{e}_i \ , \qquad \boldsymbol{G}^\alpha = c_i^\alpha \boldsymbol{e}_i \tag{A.6}$$

Now, strain tensor is expressed as

$$\begin{aligned}\boldsymbol{U} = {} & c_{i\alpha}\boldsymbol{e}_i \otimes c_j^\alpha \boldsymbol{e}_j + \frac{\sin|\boldsymbol{\omega}|}{|\boldsymbol{\omega}|}(\boldsymbol{\omega}\times\boldsymbol{1})c_{i\alpha}\boldsymbol{e}_i \otimes c_j^\alpha \boldsymbol{e}_j + \frac{1-\cos|\boldsymbol{\omega}|}{|\boldsymbol{\omega}|^2}\boldsymbol{\omega} \\ & \times(\boldsymbol{\omega}\times\boldsymbol{1})c_{i\alpha}\boldsymbol{e}_i \otimes c_j^\alpha \boldsymbol{e}_j + \boldsymbol{u}_{,\alpha} \otimes c_j^\alpha \boldsymbol{e}_j + \frac{\sin|\boldsymbol{\omega}|}{|\boldsymbol{\omega}|}(\boldsymbol{\omega}\times\boldsymbol{1})\boldsymbol{u}_{,\alpha} \\ & \otimes c_j^\alpha \boldsymbol{e}_j + \frac{1-\cos|\boldsymbol{\omega}|}{|\boldsymbol{\omega}|^2}\boldsymbol{\omega}\times(\boldsymbol{\omega}\times\boldsymbol{1})\boldsymbol{u}_{,\alpha} \otimes c_j^\alpha \boldsymbol{e}_j \\ = {} & \Bigg((c_{i\alpha}c_j^\alpha + c_j^\alpha u_{i,\alpha}) + \frac{\sin|\boldsymbol{\omega}|}{|\boldsymbol{\omega}|}(c_{i\alpha}c_j^\alpha e_{ijk}\omega_k + c_j^\alpha e_{ijk}\omega_k u_{i,\alpha}) \\ & + \frac{1-\cos|\boldsymbol{\omega}|}{|\boldsymbol{\omega}|^2}\Big\{\big[c_{i\alpha}c_j^\alpha(\omega_k\omega_k - \omega_k\omega_j)\big] + c_j^\alpha\big[(\omega_k u_{k,\alpha})\omega_i \\ & - \omega_k\omega_k u_{i,\alpha}\big]\Big\}\Bigg)\boldsymbol{e}_i \otimes \boldsymbol{e}_j \end{aligned} \tag{A.7}$$

Axial vector of $\boldsymbol{R^T R_{,\alpha}}$ is

$$\boldsymbol{k} = \frac{\sin|\boldsymbol{\omega}|}{|\boldsymbol{\omega}|}\boldsymbol{\omega}_{,\alpha} - \frac{1-\cos|\boldsymbol{\omega}|}{|\boldsymbol{\omega}|^2}\boldsymbol{\omega}_{,\alpha}\times\boldsymbol{\omega} + \left(\frac{1}{|\boldsymbol{\omega}|} - \frac{\sin|\boldsymbol{\omega}|}{|\boldsymbol{\omega}|^2}\right)\frac{(\boldsymbol{\omega}\cdot\boldsymbol{\omega}_{,\alpha})}{|\boldsymbol{\omega}|}\boldsymbol{\omega} \tag{A.8}$$

And the curvature tensor becomes

$$\boldsymbol{\mathcal{K}} = -\boldsymbol{k} \otimes \boldsymbol{G}^\alpha \tag{A.9}$$

Rotation tensor

$$\begin{aligned}\boldsymbol{R} &= \boldsymbol{1} + \frac{\sin|\boldsymbol{\omega}|}{|\boldsymbol{\omega}|}\boldsymbol{\Omega} + \frac{1-\cos|\boldsymbol{\omega}|}{|\boldsymbol{\omega}|^2}\boldsymbol{\Omega}^2 \\ &= \boldsymbol{1} + \frac{\sin|\boldsymbol{\omega}|}{|\boldsymbol{\omega}|}(\boldsymbol{\omega}\times\boldsymbol{1}) + \frac{1-\cos|\boldsymbol{\omega}|}{|\boldsymbol{\omega}|^2}\,\boldsymbol{\omega}\times\,(\boldsymbol{\omega}\times\boldsymbol{1}) \\ &= \left[\delta_{ij} + \frac{\sin|\boldsymbol{\omega}|}{|\boldsymbol{\omega}|}\omega_k e_{ijk} + \frac{1-\cos|\boldsymbol{\omega}|}{|\boldsymbol{\omega}|^2}(\omega_i\omega_j - \omega_k\omega_k\delta_{ij})\right]\boldsymbol{e}_i \otimes \boldsymbol{e}_j \end{aligned} \tag{A.10}$$

B. 1-D Bond Angle Formulation

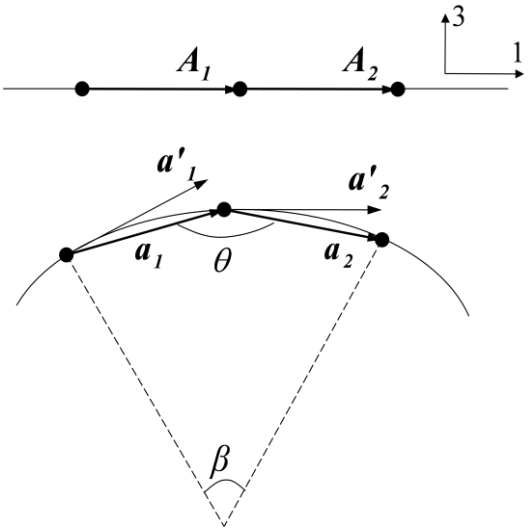

The potential is formulated as a function of bond length and bond angle, i.e.$V = V(r, \theta)$, where the bond length can be calculated through the standard Cauchy-Born rule. And the bond angle θ is related to the curvature tensor $\boldsymbol{\mathcal{K}}$, which in the one-dimensional case is expressed as $\kappa = \omega_{,s}$. The neighbouring atom bonds *AB* and *AC* are considered to be a smooth curve, which can be either an internally tangent circle or a circumscribed circle. For an internally tangent circle,

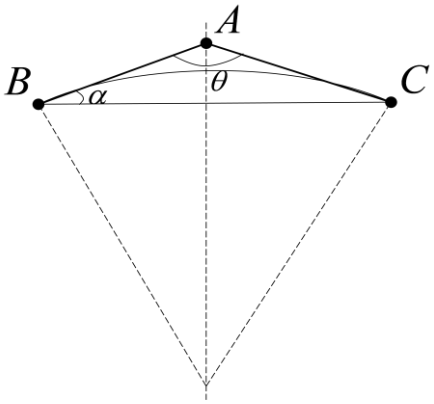

$$\beta = \kappa l = 2\kappa r$$

$$\theta = \pi - \beta = \pi - 2\kappa r. \qquad (B.1)$$

For a circumscribed circle,

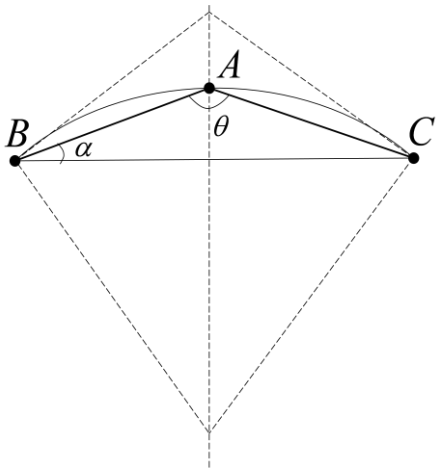

$$\beta = \kappa l = 2\kappa r$$

$$\frac{\theta}{2} = \frac{\pi - \frac{\beta}{2}}{2} \Rightarrow \theta = \pi - \frac{\beta}{2} = \pi - \kappa r. \qquad (B.2)$$

In this research, a circumscribed circle is used, because in which case the atoms are lying on the deformed curve, which should be more adequate to describe the system.

C. Total Potential Expansion

The total potential form for CNTs is

$$V_{REBO} = \sum_i \sum_{j=i+1} \left[V_R(r_{IJ}) - \bar{b}_{IJ} V_A(r_{IJ}) \right] \qquad (C.1)$$

with

$$V_R(r) = f_c(r) \left(1 + \frac{Q}{r}\right) A \exp(-\alpha r) \qquad (C.2)$$

$$V_A(r) = f_c(r) \sum_{n=1}^{3} B_n e^{-\beta_n r} \qquad (C.3)$$

and

$$f_c(r) = \begin{cases} 1 & r < R_1 \\ \left\{1 + \cos\left[\dfrac{\pi(r - R_1)}{R_2 - R_1}\right]\right\}/2 & R_1 < r < R_2 \\ 0 & r > R_2 \end{cases} \qquad (C.4)$$

while

$$\bar{b}_{IJ} = \frac{1}{2}\left(b_{IJ}^{\sigma-\pi} + b_{JI}^{\sigma-\pi}\right) \qquad (C.5)$$

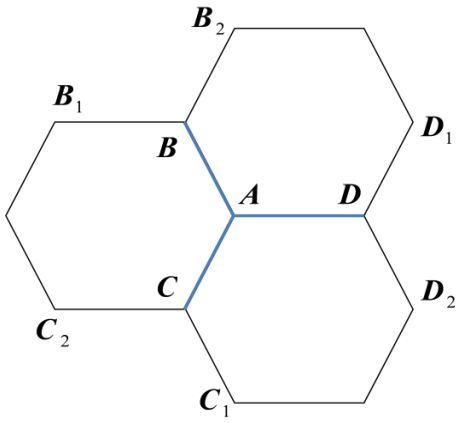

where

$$b_{IJ}^{\sigma-\pi} = \left[1 + \sum_{K(\neq I,J)} f_{cIK}\,(r_{IK}) G\left(\cos\theta_{IJK}\right)\right]^{-1/2} \qquad (C.6)$$

$$G\left(\cos\theta_{IJK}\right) = \sum_{n=0}^{5} a_n \left(\cos\theta_{IJK}\right)^n \qquad (C.7)$$

$$b_{JI}^{\sigma-\pi} = \left[1 + \sum_{K(\neq I,J)} f_{cJK}\,(r_{JK}) G\left(\cos\theta_{JIK}\right)\right]^{-1/2} \qquad (C.8)$$

In this case

$$JI = BA;\quad JK = BB_1, BB_2;\quad r_{JK} = r_{BB_1}, r_{BB_2};\quad \theta_{JIK} = \theta_{B_1BA}, \theta_{B_2BA}$$

$$JI = CA;\quad JK = CC_1, CC_2;\quad r_{JK} = r_{CC_1}, r_{CC_2};\quad \theta_{JIK} = \theta_{C_1CA}, \theta_{C_2CA}$$

$$JI = DA;\quad JK = DD_1, DD_2;\quad r_{JK} = r_{DD_1}, r_{DD_2};\quad \theta_{JIK} = \theta_{D_1DA}, \theta_{D_2DA}$$

Define

$$V_{AB} = V(r_{AB}, r_{AC}, r_{AD}, \theta_{BAC}, \theta_{BAD})$$

$$V_{AC} = V(r_{AC}, r_{AB}, r_{AD}, \theta_{BAC}, \theta_{CAD})$$

$$V_{AD} = V(r_{AD}, r_{AB}, r_{AC}, \theta_{BAD}, \theta_{CAD})$$

$$V_{BA} = V\left(r_{BB_1}, r_{BB_2}, \theta_{B_1BA}, \theta_{B_2BA}\right)$$

$$V_{CA} = V\left(r_{CC_1}, r_{CC_2}, \theta_{C_1CA}, \theta_{C_2CA}\right)$$

$$V_{DA} = V\left(r_{DD_1}, r_{DD_2}, \theta_{D_1DA}, \theta_{D_2DA}\right)$$

Then the total potential is

$$V_{total} = V_{AB} + V_{AC} + V_{AD} + V_{BA} + V_{CA} + V_{DA} \qquad (C.9)$$

The bond lengths are

$$r_s(\boldsymbol{U}, \boldsymbol{\eta}) = \sqrt{(\boldsymbol{r}_s^0 + \boldsymbol{\eta}) \cdot \boldsymbol{U}^T \boldsymbol{U} \cdot (\boldsymbol{r}_s^0 + \boldsymbol{\eta})} \qquad (C.10)$$

where $s = BB_1, BB_2, CC_1, CC_2, DD_1, DD_2$.

The deformed bond vectors are

$$\boldsymbol{r}_s = \boldsymbol{U}\boldsymbol{R}_1(\boldsymbol{V}_{\mathrm{I}} \cdot (\boldsymbol{r}_s^0 + \boldsymbol{\eta}))\boldsymbol{V}_{\mathrm{I}} + \boldsymbol{U}\boldsymbol{R}_2(\boldsymbol{V}_{\mathrm{II}} \cdot (\boldsymbol{r}_s^0 + \boldsymbol{\eta}))\boldsymbol{V}_{\mathrm{II}} \qquad (C.11)$$

And the bond angles are

$$\theta_{\bar{s}A} = \arccos \frac{\boldsymbol{r}_{AB} \cdot \boldsymbol{r}_s}{r_{AB} r_s} \qquad (C.12)$$

where $\bar{s} = B_1B,\ B_2B,\ C_1C,\ C_2C,\ D_1D,\ D_2D$

corresponding to $s = BB_1,\ BB_2,\ CC_1,\ CC_2,\ DD_1,\ DD_2$.

Define bond lengths r_{AB} , r_{AC} , r_{AD} , r_{BB_1} , r_{BB_2} , r_{CC_1} , r_{CC_2} , r_{DD_1} , r_{DD_2} as a_i (i=1,2,…,9) and bond angles θ_{BAC} , θ_{BAD} , θ_{CAD} , θ_{B_1BA} , θ_{B_2BA} , θ_{C_1CA} , θ_{C_2CA} , θ_{D_1DA}, θ_{D_2DA} as θ_i (i=1,2,…,9), inner displacement can be determined by

$$\frac{\partial W}{\partial \boldsymbol{\eta}} = \sum_{i=1}^{9} \left(\frac{\partial W}{\partial a_i} \frac{\partial a_i}{\partial \boldsymbol{\eta}} + \frac{\partial W}{\partial \theta_i} \frac{\partial \theta_i}{\partial \boldsymbol{\eta}} \right) = \boldsymbol{0} \qquad (C.13)$$

where strain energy density $W = V_{total}/S_0$.

Force tensor can be obtained from

$$S_{ab} = \frac{\partial W}{\partial U_{ab}} = \sum_{i=1}^{9} \left(\frac{\partial W}{\partial a_i} \frac{\partial a_i}{\partial U_{ab}} + \frac{\partial W}{\partial \theta_i} \frac{\partial \theta_i}{\partial U_{ab}} \right) \tag{C.14}$$

Couple tensor can be expressed as

$$T_{ab} = \frac{\partial W}{\partial \mathcal{K}_{ab}} = \sum_{i=1}^{9} \frac{\partial W}{\partial \theta_i} \frac{\partial \theta_i}{\partial \mathcal{K}_{ab}} \tag{C.15}$$

Stretch modulus-like tensor

$$\boldsymbol{n} = \frac{\partial^2 W}{\partial \boldsymbol{U} \partial \boldsymbol{U}} - \frac{\partial^2 W}{\partial \boldsymbol{U} \partial \boldsymbol{\eta}} \cdot \left(\frac{\partial^2 W}{\partial \boldsymbol{\eta} \partial \boldsymbol{\eta}} \right)^{-1} \cdot \frac{\partial^2 W}{\partial \boldsymbol{\eta} \partial \boldsymbol{U}} \tag{C.16}$$

where

$$\frac{\partial^2 W}{\partial U_{ab} \partial U_{kl}} = \sum_{i=1}^{9} \sum_{j=1}^{9} \left(\frac{\partial^2 W}{\partial a_i \partial a_j} \frac{\partial a_j}{\partial U_{kl}} \frac{\partial a_i}{\partial U_{ab}} + \frac{\partial^2 W}{\partial a_i \partial \theta_j} \frac{\partial \theta_j}{\partial U_{kl}} \frac{\partial a_i}{\partial U_{ab}} + \frac{\partial W}{\partial a_i} \frac{\partial^2 a_i}{\partial U_{ab} \partial U_{kl}} \right.$$
$$\left. + \frac{\partial^2 W}{\partial \theta_i \partial a_j} \frac{\partial a_j}{\partial U_{kl}} \frac{\partial \theta_i}{\partial U_{ab}} + \frac{\partial^2 W}{\partial \theta_i \partial \theta_j} \frac{\partial \theta_j}{\partial U_{kl}} \frac{\partial \theta_i}{\partial U_{ab}} + \frac{\partial W}{\partial \theta_i} \frac{\partial^2 \theta_i}{\partial U_{ab} \partial U_{kl}} \right)$$

$$\frac{\partial^2 W}{\partial U_{ab} \partial \eta_p} = \sum_{i=1}^{9} \sum_{j=1}^{9} \left(\frac{\partial^2 W}{\partial a_i \partial a_j} \frac{\partial a_j}{\partial \eta_p} \frac{\partial a_i}{\partial U_{ab}} + \frac{\partial^2 W}{\partial a_i \partial \theta_j} \frac{\partial \theta_j}{\partial \eta_p} \frac{\partial a_i}{\partial U_{ab}} + \frac{\partial W}{\partial a_i} \frac{\partial^2 a_i}{\partial U_{ab} \partial \eta_p} \right.$$
$$\left. + \frac{\partial^2 W}{\partial \theta_i \partial a_j} \frac{\partial a_j}{\partial \eta_p} \frac{\partial \theta_i}{\partial U_{ab}} + \frac{\partial^2 W}{\partial \theta_i \partial \theta_j} \frac{\partial \theta_j}{\partial \eta_p} \frac{\partial \theta_i}{\partial U_{ab}} + \frac{\partial W}{\partial \theta_i} \frac{\partial^2 \theta_i}{\partial U_{ab} \partial \eta_p} \right)$$

$$\frac{\partial^2 W}{\partial \eta_p \partial \eta_q} = \sum_{i=1}^{9} \sum_{j=1}^{9} \left(\frac{\partial^2 W}{\partial a_i \partial a_j} \frac{\partial a_j}{\partial \eta_q} \frac{\partial a_i}{\partial \eta_p} + \frac{\partial^2 W}{\partial a_i \partial \theta_j} \frac{\partial \theta_j}{\partial \eta_q} \frac{\partial a_i}{\partial \eta_p} + \frac{\partial W}{\partial a_i} \frac{\partial^2 a_i}{\partial \eta_p \partial \eta_q} \right.$$
$$\left. + \frac{\partial^2 W}{\partial \theta_i \partial a_j} \frac{\partial a_j}{\partial \eta_q} \frac{\partial \theta_i}{\partial \eta_p} + \frac{\partial^2 W}{\partial \theta_i \partial \theta_j} \frac{\partial \theta_j}{\partial \eta_q} \frac{\partial \theta_i}{\partial \eta_p} + \frac{\partial W}{\partial \theta_i} \frac{\partial^2 \theta_i}{\partial \eta_p \partial \eta_q} \right)$$

$$\frac{\partial^2 W}{\partial \eta_q \partial U_{kl}} = \sum_{i=1}^{9} \sum_{j=1}^{9} \left(\frac{\partial^2 W}{\partial a_i \partial a_j} \frac{\partial a_j}{\partial U_{kl}} \frac{\partial a_i}{\partial \eta_q} + \frac{\partial^2 W}{\partial a_i \partial \theta_j} \frac{\partial \theta_j}{\partial U_{kl}} \frac{\partial a_i}{\partial \eta_q} + \frac{\partial W}{\partial a_i} \frac{\partial^2 a_i}{\partial \eta_q \partial U_{kl}} \right.$$
$$\left. + \frac{\partial^2 W}{\partial \theta_i \partial a_j} \frac{\partial a_j}{\partial U_{kl}} \frac{\partial \theta_i}{\partial \eta_q} + \frac{\partial^2 W}{\partial \theta_i \partial \theta_j} \frac{\partial \theta_j}{\partial U_{kl}} \frac{\partial \theta_i}{\partial \eta_q} + \frac{\partial W}{\partial \theta_i} \frac{\partial^2 \theta_i}{\partial \eta_q \partial U_{kl}} \right)$$

And bending modulus-like tensor

$$\boldsymbol{m} = \frac{\partial^2 W}{\partial \boldsymbol{\mathcal{K}} \partial \boldsymbol{\mathcal{K}}} - \frac{\partial^2 W}{\partial \boldsymbol{\mathcal{K}} \partial \boldsymbol{\eta}} \cdot \left(\frac{\partial^2 W}{\partial \boldsymbol{\eta} \partial \boldsymbol{\eta}} \right)^{-1} \cdot \frac{\partial^2 W}{\partial \boldsymbol{\eta} \partial \boldsymbol{\mathcal{K}}} \qquad (C.17)$$

where

$$\frac{\partial^2 W}{\partial \mathcal{K}_{ab} \partial \mathcal{K}_{kl}} = \sum_{i=1}^{9} \sum_{j=1}^{9} \left(\frac{\partial^2 W}{\partial \theta_i \partial \theta_j} \frac{\partial \theta_j}{\partial \mathcal{K}_{kl}} \frac{\partial \theta_i}{\partial \mathcal{K}_{ab}} + \frac{\partial W}{\partial \theta_i} \frac{\partial^2 \theta_i}{\partial \mathcal{K}_{ab} \partial \mathcal{K}_{kl}} \right)$$

$$\frac{\partial^2 W}{\partial \mathcal{K}_{ab} \partial \eta_p} = \sum_{i=1}^{9} \sum_{j=1}^{9} \left(\frac{\partial^2 W}{\partial \theta_i \partial a_j} \frac{\partial a_j}{\partial \eta_p} \frac{\partial \theta_i}{\partial \mathcal{K}_{ab}} + \frac{\partial^2 W}{\partial \theta_i \partial \theta_j} \frac{\partial \theta_j}{\partial \eta_p} \frac{\partial \theta_i}{\partial \mathcal{K}_{ab}} + \frac{\partial W}{\partial \theta_i} \frac{\partial^2 \theta_i}{\partial \mathcal{K}_{ab} \partial \eta_p} \right)$$

$$\frac{\partial^2 W}{\partial \eta_p \partial \eta_q} = \sum_{i=1}^{9} \sum_{j=1}^{9} \left(\frac{\partial^2 W}{\partial a_i \partial a_j} \frac{\partial a_j}{\partial \eta_q} \frac{\partial a_i}{\partial \eta_p} + \frac{\partial^2 W}{\partial a_i \partial \theta_j} \frac{\partial \theta_j}{\partial \eta_q} \frac{\partial a_i}{\partial \eta_p} + \frac{\partial W}{\partial a_i} \frac{\partial^2 a_i}{\partial \eta_p \partial \eta_q} \right.$$

$$\left. + \frac{\partial^2 W}{\partial \theta_i \partial a_j} \frac{\partial a_j}{\partial \eta_q} \frac{\partial \theta_i}{\partial \eta_p} + \frac{\partial^2 W}{\partial \theta_i \partial \theta_j} \frac{\partial \theta_j}{\partial \eta_q} \frac{\partial \theta_i}{\partial \eta_p} + \frac{\partial W}{\partial \theta_i} \frac{\partial^2 \theta_i}{\partial \eta_p \partial \eta_q} \right)$$

$$\frac{\partial^2 W}{\partial \eta_q \partial \mathcal{K}_{kl}} = \sum_{i=1}^{9} \sum_{j=1}^{9} \left(\frac{\partial^2 W}{\partial a_i \partial \theta_j} \frac{\partial \theta_j}{\partial \mathcal{K}_{kl}} \frac{\partial a_i}{\partial \eta_q} + \frac{\partial^2 W}{\partial \theta_i \partial \theta_j} \frac{\partial \theta_j}{\partial \mathcal{K}_{kl}} \frac{\partial \theta_i}{\partial \eta_q} + \frac{\partial W}{\partial \theta_i} \frac{\partial^2 \theta_i}{\partial \eta_q \partial \mathcal{K}_{kl}} \right)$$